MIXED-PHASE CLOUDS, THIN CIRRUS CLOUDS, AND OLR OVER THE TROPICS: OBSERVATIONS, RETRIEVALS, AND RADIATIVE IMPACTS

A Dissertation

by

JOONSUK LEE

Submitted to the Office of Graduate Studies of
Texas A&M University
in partial fulfillment of the requirements for the degree of

DOCTOR OF PHILOSOPHY

August 2007

Major Subject: Atmospheric Sciences

MIXED-PHASE CLOUDS, THIN CIRRUS CLOUDS, AND OLR OVER THE TROPICS: OBSERVATIONS, RETRIEVALS, AND RADIATIVE IMPACTS

A Dissertation

by

JOONSUK LEE

Submitted to the Office of Graduate Studies of
Texas A&M University
in partial fulfillment of the requirements for the degree of

DOCTOR OF PHILOSOPHY

Approved by:

Co-Chairs of Committee,	Ping Yang
	Andrew E. Dessler
Committee Members,	Gerald R. North
	George W. Kattawar
	Steven Platnick
Head of Department,	Richard Orville

August 2007

Major Subject: Atmospheric Sciences

ABSTRACT

Mixed-phase Clouds, Thin Cirrus Clouds, and OLR over the Tropics:

Observations, Retrievals, and Radiative Impacts. (August 2007)

Joonsuk Lee, B. S., Yonsei University;

M.S., Yonsei University

Co-Chairs of Advisory Committee: Dr. Ping Yang
Dr. Andrew E. Dessler

The tropics is a very important region in terms of earth's radiation budget because the net radiative heating is largest in the tropics and that surplus energy is redistributed by the circulations of oceans and atmospheres. Moreover, a large number of clouds are formed by deep convection and convergence of water vapor. Thus, it is very important to understand the radiative energy balance of the tropics and the effect of clouds on the radiation field.

For mixed-phase clouds, error analyses pertaining to the inference of effective particle sizes and optical thicknesses are performed. Errors are calculated with respect to the assumption of a cloud containing solely liquid or ice phase particles. The analyses suggest that the effective particle size inferred for a mixed-phase cloud can be underestimated (or overestimated) if a pure liquid phase (or pure ice phase) is assumed for the cloud, whereas the corresponding cloud optical thickness can be overestimated (or underestimated).

The analyses of optical depth and fraction of occurrence for thin cirrus clouds showed that about 40% of pixels flagged as clear-sky contain detectible thin cirrus clouds. The regions of high occurrence and large optical depth located around deep convection showed seasonal variations. The thin cirrus clouds occur more frequently with larger optical depth in the northern (southern) hemisphere during spring and summer (autumn and winter). The net cloud radiative forcing by thin cirrus clouds is positive at the top of atmosphere and is negative at the bottom of atmosphere.

The difference in OLR between measurement and model is 4.2 Wm^{-2} for September 2005. The difference is smaller in moist regions and larger in drier regions. OLR increases with increasing surface temperatures up to 300 K but decreases at surface temperatures larger than 300 K due to the strong absorption of increased water vapor. In summary, if the surface temperature is lower than the threshold of convection (300 K), temperature is a dominant factor in OLR and if the surface temperature is larger than 300 K, OLR is strongly influenced by water vapor.

DEDICATION

This dissertation is dedicated to my friends and family who have always helped and supported me throughout my life.

ACKNOWLEDGEMENTS

I would like to thank my co-advisors, Dr. Ping Yang and Dr. Andrew Dessler, for their guidance and support. I would like to thank them for giving me the opportunity to continue my education, and for the encouragement to continue further. I would also like to thank the members of my committee, Dr. Gerald North, Dr. George Kattawar, and Dr. Steven Platnick, for supporting my research and for giving their time to edit this dissertation. I would like to thank my colleagues who offered a lot of help throughout this research. Without them, this study would never have been completed.

This study was supported by the National Science Foundation Physical Meteorological Program managed by Dr. Andrew Detwiler (ATM-0239605), and by a NASA research grant (NNG04GL24G) from the Radiation Sciences Program managed by Dr. Hal Maring (previously by Dr. Donald Anderson) and NASA MODIS program managed by Dr. Paula Bontempi.

Finally, I would like to thank my family and friends for all their support throughout the years.

TABLE OF CONTENTS

Page

CHAPTER Page

LIST OF FIGURES

FIGURE Page

FIGURE Page

FIGURE Page

LIST OF TABLES

CHAPTER I

INTRODUCTION

The tropical warm pool region is where deep convection occurs frequently and has low outgoing longwave radiation (OLR). Moreover, it is shown that the warm pool is a region of local maximum in net radiation at the top of atmosphere. By combining these facts with frequent precipitation, moisture transport, and tropical oceans, the tropics becomes very important regions in terms of earth's radiation budget.

It is important to understand the effect of cirrus clouds on the energy balance of the tropical atmosphere because clouds can change the energy balance by reflecting incoming solar radiation and absorbing longwave radiation emitted from the surface and lower atmosphere. Their frequent occurrence and persistence, their large areal coverage, and high altitude make them important components in radiative processes. The spatial and temporal variations of cirrus clouds may be another major factor that alters radiation budgets.

Clouds generally have a cooling effect on the climate system because the longwave warming effect by clouds due to blackbody emissions at low temperature in the atmosphere is smaller than the shortwave cooling effect due to reflection by clouds. Because water and ice clouds reflect solar radiation while absorb strongly longwave raditation, heating occurs in the lower atmosphere, strong cooling occurs at the top of

---

This dissertation follows the style of *Journal of the Atmospheric Sciences*.

thick clouds, and net heating in thin layers [Stephens, 2005; Rossow and Zhang, 1995]. The interaction between vertically distributed radiative and latent heating with large-scale dynamics of the atmosphere drives the global hydrological cycle [Webster, 1994]. Also, clouds affect the distributions of diabatic heating within the atmosphere leading to a change in atmospheric circulation [Stephens, 2005]. Cloud heating has a direct influence on the general circulation of the atmosphere. Thus, the interaction between radiative effect of clouds and circulation will contribute to the response of regional climates to changes created by global warming. The feedbacks caused by the radiative effect of clouds make it difficult to predict earth's climate change more accurately.

With the help of satellite radiation budget data sets, the radiative transfer models and other observations, we can understand clouds' radiative effect within the atmosphere and at the surface [Bergman and Hendon, 1998]. Thus, in this study, the mixed-phase clouds, the characteristics of tropical thin cirrus clouds, their radiative impact, and the clear-sky OLR over the tropics will be examined for the better understand of energy balance in the tropical regions.

CHAPTER II

THE INFLUENCE OF THERMODYNAMIC PHASE ON THE RETRIEVAL OF MIXED-PHASE CLOUD MICROPHYSICAL AND OPTICAL PROPERTIES IN THE VISIBLE AND NEAR INFRARED REGION*

2.1 Background

Both ice and water phase particles may coexist in clouds when the temperature is between -40^{o}C and 0^{o}C (Fleishauer et al. [2002]; Korolev et al. [2003]). Such mixed-phase clouds are important for several reasons. First, the difference in saturation vapor pressure between ice and water means that these clouds evolve differently from single-phase clouds. Additionally, mixed-phase clouds alter the radiative flux differently from single-phase clouds, thereby necessitating different treatment of these clouds in both numerical weather forecasting and general circulation models (e.g., Sun and Shine, 1994). Furthermore, mixed-phase clouds can create hazardous conditions for aviation due to decreased visibility and aircraft icing (Riley [1998]).

Mixed-phase clouds are frequently observed in the atmosphere (Fleishauer et al. [2002]; Zuidema et al. [2005]). Recent research on mixed-phase clouds has focused on the analysis of ground-based or aircraft measurements (Fleishauer et al. [2002]; Zuidema et al. [2005]), the microphysical characteristics in cloud processes (Jacobson [2003];

*Reprinted with permission from "The Influence of Thermodynamic Phase on the Retrieval of Mixed-Phase Cloud Microphysical and Optical Properties in the Visible and Near-Infrared Region", by Lee, J., P. Yang, A. E. Dessler, B. A. Baum, and S. Platnick, 2006, *IEEE Geoscience and Remote Sensing Letters*, 3, 287-291. Copyright 2006 by The Institute of Electrical and Electronics Engineers, Inc.

Korolev and Isaac [2003]), and modeling simulations (Sun and Shine [1994]; Lubin [2004]). However, current operational satellite-based retrievals of cloud microphysical and optical properties are based on the assumption of a cloud being composed entirely of either ice particles or water droplets (Nakajima and King [1990]; Platnick et al. [2001]; King et al. [2004]). This study investigates the cloud optical and microphysical properties for clouds containing a mixture of both ice and water particles and compares them with retrievals that incorrectly assume that the phase is solely ice or liquid water.

2.2 Radiative transfer model

The radiative transfer model used in this study discretizes the atmosphere into 100 layers. The cloud-free atmospheric optical thickness for each layer is computed using the MODTRAN radiative transfer model (Berk et al. [1989]). The bidirectional reflectance at the top of the atmosphere is computed using the discrete-ordinate radiative transfer model (DISORT) (Stamnes et al. [1998]) with a precalculated clear-sky atmospheric gaseous optical thickness vertical profile from MODTRAN. For a cloud layer, the bulk single-scattering properties of ice particles and water droplets are available from a precalculated library. The single-scattering properties of ice particles, covering a range of sizes from 1 to 4000 μm, are computed with the approach reported in Yang et al. [2000]. The mean (or bulk) scattering properties are calculated using 30 *in situ* size distributions measured for a variety of midlatitude and tropical cirrus cloud systems obtained during several field campaigns (Fu [1996]; Mitchell et al. [1996]).

In this study, the particle habit (or shape) percentage as a function of particle size for a given size distribution of ice crystals is consistent with that used in the MODIS (Moderate Resolution Imaging Spectroradiometer) operational (Collection 4 and earlier) cloud products (Platnick et al. [2003]). Specifically, the habits of ice particles considered for a given size distribution include bullet rosettes, hollow columns, aggregates, and hexagonal plates. For small ice particles (D_{max} < 70 μm, where D_{max} is maximum dimension), the ice habit mixture is composed of 50% bullet rosettes, 25% hexagonal plates, and 25% hollow columns. For large ice particles (D_{max} > 70 μm), the mixture is composed of 30% aggregates, 20% bullet rosettes, 20% hexagonal plates, and 20% hollow columns, following Baum et al. [2000] and King et al. [2004]. The single-scattering properties of water clouds are calculated based on the Lorenz-Mie scattering, assuming 50 different Gamma size distributions.

The single-scattering properties of mixed-phase clouds are calculated following the definitions in Yang et al. [2003]. Here, the mixed-phase clouds are assumed to be a uniform mixture of ice and water particles. The total water content (*TWC*) is the sum of ice water content (*IWC*) and liquid water content (*LWC*), i.e., $TWC = IWC + LWC$. The ice mass fraction (γ), is defined as follows:

$$\gamma = \frac{IWC}{TWC}. \tag{2.1}$$

The effective particle size D_{em} for a mixed-phase cloud can be specified as follows [Yang et al., 2003]:

$$D_{em} = \left[\left(\frac{\gamma}{D_{ei}\rho_i} + \frac{1-\gamma}{D_{ew}\rho_w} \right) \rho_m \right]^{-1}, \tag{2.2}$$

where D_e and ρ indicate the effective size and mass density, respectively; and the subscripts i, w, and m in Eq. (2.2) denote ice, water, and mixed-phase clouds, respectively.

The optical thickness of a mixed-phase cloud (τ_m) is given by

$$\tau_m = \tau_i + \tau_w = \Delta z \int Q_{ei} A_i n_i dD + \Delta z \int Q_{ew} A_w n_w dD \tag{2.3}$$

where Δz is the geometric thickness of the cloud, Q_e is the extinction efficiency, A is the projected area of the particle, n is the size distribution of particle number density, D is the characteristic length of the particle. It can be shown that the optical thicknesses pertaining to the ice and water components of a mixed-phase cloud are given, respectively, by the following expressions:

$$\tau_i = \frac{\langle Q_{ei} \rangle D_{em} \rho_m \gamma}{\langle Q_{em} \rangle D_{ei} \rho_i} \tau_m, \tag{2.4}$$

$$\tau_w = \frac{\langle Q_{ew} \rangle D_{em} \rho_m (1-\gamma)}{\langle Q_{em} \rangle D_{ew} \rho_w} \tau_m, \tag{2.5}$$

The detailed mathematical expressions for the quantities involved in Eqs. (2.4) and (2.5) can be found in Yang et al. [2003].

2.3 Methodology

We calculate the bidirectional reflectance at the top of the atmosphere using the radiative transfer model discussed in the previous section. The bidirectional reflectance is defined as

$$R(\mu,\phi;\mu_0,\phi_0) = \frac{\pi I(0;\mu,\phi)}{\mu_0 F_0} \quad , \tag{2.6}$$

where $I(0;\mu,\phi)$ is the reflected radiance at the top of atmosphere, F_0 is the incident solar flux at the top of the atmosphere, μ_0 is cosine of the solar zenith angle, ϕ_0 is the solar azimuthal angle, μ is cosine of the sensor zenith angle, and ϕ is the sensor azimuthal angle. In this study, we simulate the bidirectional reflectance at high latitudes where mixed-phase clouds are frequently observed and use 55.8^o, 7.0^o, and 20.0^o for the solar zenith angle, the sensor zenith angle, and the difference between solar and sensor azimuthal angles (*i.e.,* the relative azimuth angle), respectively. The corresponding scattering angle is approximately 130°.

A popular method pioneered by Twomey and Cocks [1989], Nakajima and King [1990], and Rawlins and Foot [1990] infers cloud microphysical and optical properties by using the bidirectional reflectance observations in two or more spectral bands that have varying amounts of cloud particle absorption, *e.g*., a nonabsorbing visible band and an absorbing near infrared band, or even two shortwave infrared bands (Platnick et al. [2001]). The reflectance in a nonabsorbing band (e.g., 0.67, 0.87 μm) is largely dependent on cloud optical thickness, whereas the reflectance in an absorbing band (e.g., 1.6, 2.1, and 3.75 μm) is sensitive to the cloud particle size (King [1987]). In this study,

we use a nonabsorbing and absorbing band defined by the MODIS spectral bandpasses at 0.87 and 2.13 μm, respectively, which is a combination used for the primary MODIS operational cloud retrieval (Platnick et al. [2003]).

This method is most accurate over a dark ocean surface away from sunglint, where the reflection comes from the cloud layer with little influence from the underlying surface (King et al. [2004]. On a bright surface such as ice or snow where the surface reflectance is large, the signal from the cloud is mixed with the signal from surface. In this study, a surface albedo of 0.03 is used both at 0.87 μm and 2.13 μm (Moore et al, [1998]; King et al. [2004]) which is representative of an ocean surface. Sunglint is not a concern for the solar-viewing geometry defined in this study.

2.4 Results

Figure 2.1 shows the variation of the effective particle diameter (Figure 2.1(a)) and optical thickness (Figure 2.1(b)) for clouds composed solely of ice, water, and a range of ice mass fractions. The water cloud has an effective particle diameter, D_{ew}, of 15 μm and an optical thickness of τ_w =10. The ice cloud has an effective particle diameter, D_{ei}, of 50 μm and an optical thickness of τ_i=10. In Figure 2.1(a) when the ice fraction γ=0, *i.e.,* a pure liquid water cloud case, the effective particle diameter becomes that of the water cloud. When γ=1, *i.e.,* a pure ice cloud case, the effective diameter becomes that of the ice cloud. For values of γ between 0 and 1, the effective particle size varies smoothly between the ice and water cloud value. When γ=0.5, for example, the ice water content equals the liquid water content, but the effective particle diameter (23.5

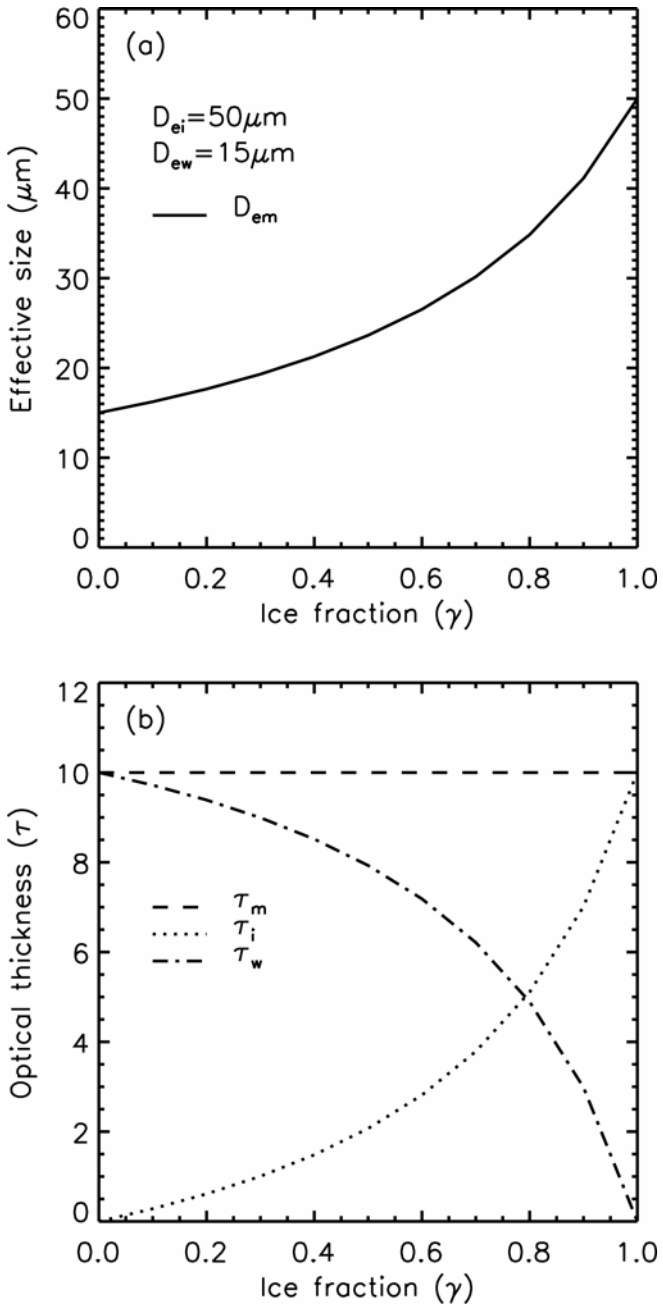

Figure 2.1 The variation of (a) effective particle diameter and (b) optical thickness as a function of ice fraction (γ) in a mixed-phase cloud. Subscripts *i*, *w*, and *m* refer to an ice, liquid water, and mixed-phase cloud, respectively.

μm, see Eq. 2.2) is less than the arithmetic mean of the ice and water cloud effective particle sizes (32.5 μm). This occurs because there are larger numbers of smaller particles in the water cloud.

Figure. 2.1(b) shows similar results as for Figure 2.1(a), but for a cloud with a total optical thickness, τ_m, equal to 10. Note that the magnitude of the derivative of the τ_w and τ_i components increases rapidly with γ. Figure 2.2 shows the response of the bidirectional reflectance at 0.87 and 2.13 μm to changes in γ. These results are superimposed on theoretical isolines of τ and D_e for pure ice (Figure 2.2(a)) and pure water (Figure 2.2(b)) clouds. Each symbol (+) corresponds to the ice fraction, which changes from 0 to 1 in increments of 0.1. The reflectances change gradually from those of a homogeneous water cloud to those for an ice cloud. The reflectance at 2.13μm for a water cloud (γ=0) is larger than that for the ice cloud (γ=1) because (a) ice is more absorbing than liquid water, and (b) ice cloud particles tend to be larger than for the water cloud and therefore have a smaller cloud reflectance. Note that the cloud reflectance tends to decrease with increasing particle size. Thus, as γ increases, the effective particle size inferred from the liquid water theoretical curves increases. The optical thickness in Figure 2.2b also increases with γ because the ice particles have a larger asymmetry parameter due to their larger size and nonspherical habits.

Figure 2.3 compares the differences between homogeneous (with respect to thermodynamic phase) ice and water clouds for effective particle diameters (Figure 2.3(a)) and optical thicknesses (Figure 2.3(b)) retrieved from the theoretical relationships of Figure 2.2. In this example (D_{ei}=50 μm, D_{ew}=15 μm), the effective particle diameter

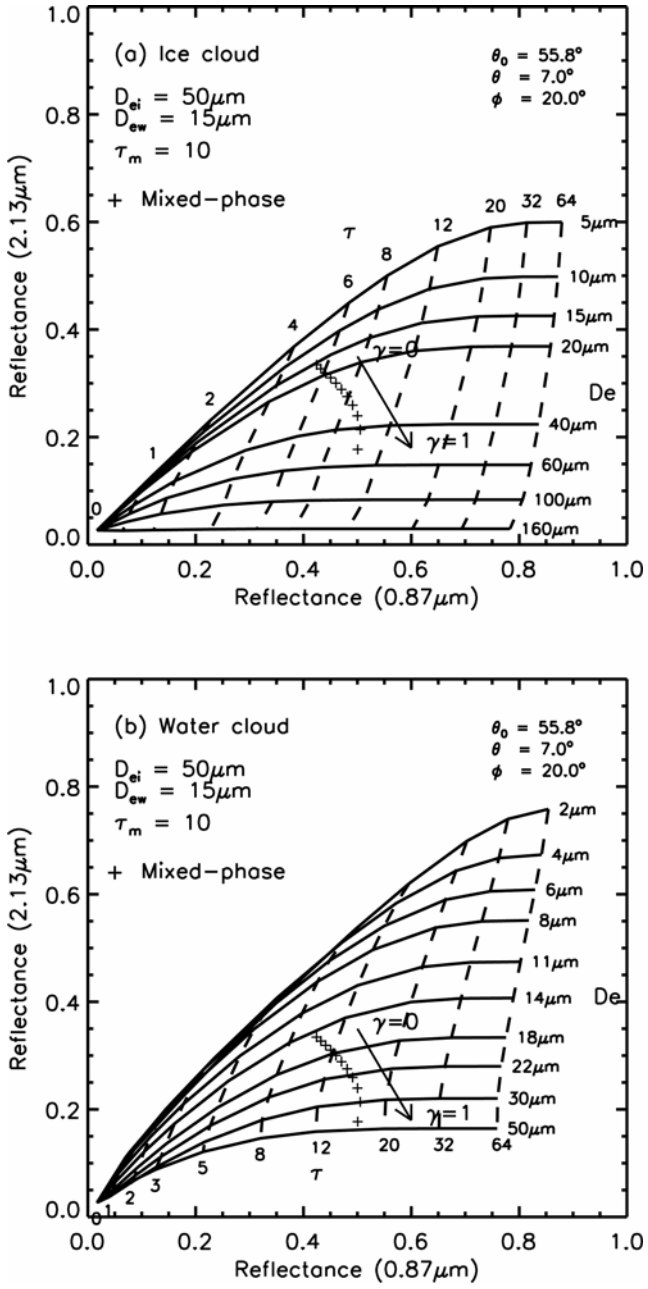

Figure 2.2 The variation of the bidirectional reflectance for a mixed-phase cloud at 0.87 and 2.13μm with the ice fraction (γ) superimposed on the theoretical τ-D_e curves for the (a) ice cloud and (b) water cloud. γ varies from 0 to 1 as denoted by the (+) symbols.

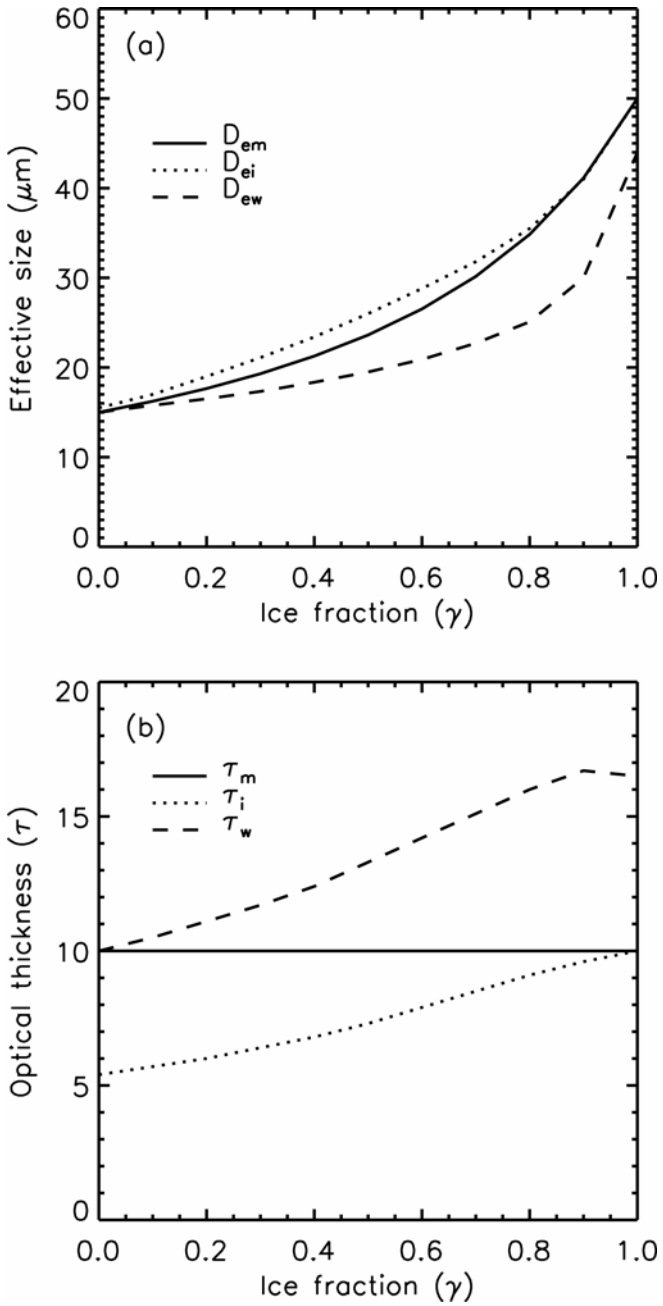

Figure 2.3 The comparison of the (a) effective diameter and (b) optical thickness retrieved assuming a homogeneous ice and water cloud as a function of ice mass fraction (γ). The true mixed-phase cloud parameters (τ_m, D_{em}) are also shown.

inferred with the assumption of a homogeneous water cloud is smaller than the actual particle size of the mixed-phase cloud. Conversely, the effective particle diameter obtained assuming an ice cloud is larger than that of the mixed-phase cloud. Figure 2.3(b) shows the differences in the inferred optical thickness. For this case (τ_m=10), the optical thickness obtained with the water (ice) cloud assumption is larger (smaller) thanthat of the mixed-phase cloud.

Figure 2.4 shows the variation of the bidirectional reflectance at 0.87 and 2.13 μm with both γ and optical thickness for mixed-phase clouds as well as for homogeneous ice and water clouds. The effective particle diameter of the ice and water clouds is fixed at 50 μm and 15 μm, respectively. The optical thickness varies from 1 to 15. In Figure 2.4(a) when γ=1, the reflectances correspond to purely ice cloud optical thicknesses of 1, 3, 5, 8, and 15, respectively. In Figure 2.4(b) when γ=0, the reflectances correspond to purely water cloud optical thicknesses of 1, 3, 5, 8, and 15, respectively. It is clear from this plot that substantial errors in inferred effective particle size and optical thickness parameters may be incurred if a mixed-phase cloud is treated as a single-phase ice or water cloud when using a bispectral retrieval algorithm.

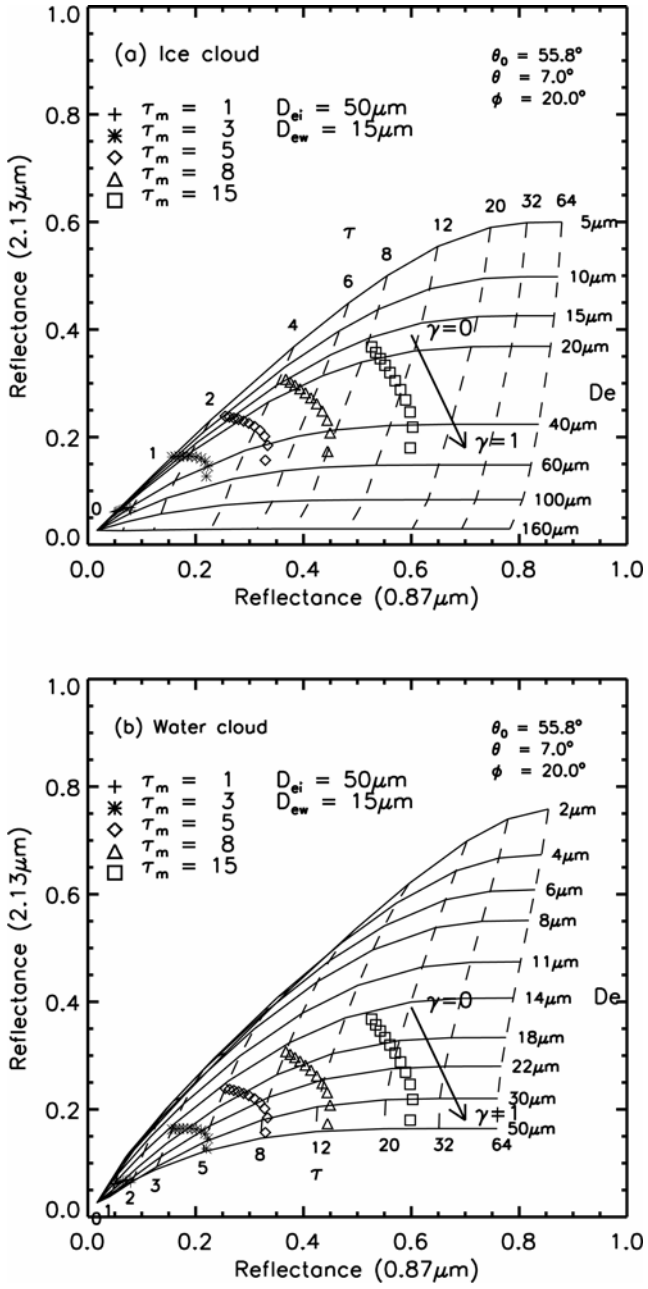

Figure 2.4 The variation of the bidirectional reflectance for a mixed-phase cloud at 0.87 and 2.13μm with the ice fraction (γ) and optical thickness of the mixed-phase cloud superimposed on the theoretical τ-D_e curves for the (a) ice cloud and (b) water cloud. γ varies from 0 to 1 as denoted by the (+) symbols.

CHAPTER III

THE DISTRIBUTION OF TROPICAL THIN CIRRUS CLOUDS AND THEIR RADIATIVE IMPACTS: ANALYSES BASED ON MODIS AND AIRS MEASUREMENTS

3.1 Background

Clouds play an important role in the earth's water and radiation budget. The horizontal and vertical distributions of the radiative heating rate are affected by clouds which reflect solar radiation and absorb longwave radiation. It is quite challenging to quantify the role of clouds in the atmosphere because of the need for the detailed and accurate information on their optical and physical properties including optical depth, particle size distribution, particle shape, location, physical thickness and occurrence frequency. However, it is difficult to obtain this information, particularly for thin cirrus clouds.

Thin cirrus clouds are frequently observed near the tropical tropopause, according to various measurements [Winker and Trepte, 1998; McFarquar et al., 2000; Massie et al, 2002; Pfiester, 2001]. Prabhakara et al. [1993], using Nimbus-4 Infrared Interferometer Spectrometer (IRIS) measurements, found that seasonal cloud cover by thin cirrus clouds is more than 50% near the central region of the warm pool in the western Pacific. Wang et al. [1996], using the Stratospheric Aerosol Gas Experiment (SAGE) II measurement, also found that maximum occurrence (~70%) is located at an altitude of 15.5km over the western Pacific. Thin cirrus clouds were observed to extend

from several hundred meters to one kilometer vertically and thousands of kilometers horizontally by the Lidar In-space Technology Experiment (LITE) [Winker and Trepte, 1998].

These thin cirrus clouds can be divided into two types, based on their formation mechanisms: high, thin, laminar cirrus clouds and lower, thicker, more structured cirrus clouds. Pfister et al. [2001] showed that on the basis of trajectory analyses and temperature histories, these two types were formed respectively by (1) in situ formation by uplift of humid air and (2) recent outflow from convection. Massie et al. [2002] used Halogen Occultation Experiment (HALOE) aerosol extinction data and found that half of the HALOE cirrus observations are from convective blow-off, while the other half are consistent with in situ formation processes.

Given the frequent occurrence of these types of clouds, the effect on the water and radiation budget can be significant. Thin cirrus clouds absorb longwave radiation and emit radiation at very low temperatures. This property can lead to local heating by a few K per day [Jensen et al., 1996; McFarquhar et al., 2000] and a net positive cloud forcing of 1 Wm^{-2} [Wang et al., 1996; McFarquhar et al., 2000]. This local heating near the tropopause can induce lifting of air and result in the formation of more cirrus or the growth of cirrus, causing a decrease in water vapor amount entering the stratosphere [Potter and Holton, 1995]. Thus, it is important to understand the radiative effect of thin cirrus clouds at the tropopause.

However, because of the difficulties associated with in situ measurements of the proportion of thin cirrus clouds and the limited number of observations, it is difficult to

accurately calculate the radiative impact of these clouds. Several studies using lidar measurements [Winker and Trepte, 1998; Pfister et al., 2001; Comstock et al, 2002] and ground-based measurements [Comstock and Sassen, 2001; Mather et al., 1998; Platt et al., 1998] show valuable results, but with time and space limitations. Wang et al. [1996] derived a 6-year climatology of cloud frequency from SAGE II observations, but their sampling rate and distribution was limited due to the shortcomings of the solar occultation technique.

It is important to investigate the frequency of occurrence of thin cirrus clouds, their mean optical depth and radiative impact for better understanding of the role of thin cirrus clouds in the climate system. Thus, the objectives of this study are (1) to derive the climatological characteristics of optical depth of tropical thin cirrus clouds to find the frequency and location of occurrence and (2) to calculate the effect of thin cirrus clouds' radiative forcing in terms of optical depth using retrieved optical depth and Atmospheric Infrared Sounder (AIRS) data.

3.2 Data

The simulation of the effect of clouds on atmospheric radiation needs the cloud and atmospheric properties required for computing radiative flux. Cloud properties from MODIS and atmospheric profiles from AIRS on the Aqua satellite were used to fulfill these calculations in this study.

Aqua is one of the National Aeronautics and Space Administration (NASA) Earth Observing System (EOS) satellite missions. Aqua has six instruments including

the Atmospheric Infrared Sounder (AIRS), the Advanced Microwave Sounding Unit (AMSU-A), the Humidity Sounder for Brazil (HSB), the Advanced Microwave Scanning Radiometer for EOS (AMSR-E), the Moderate Resolution Imaging Spectroradiometer (MODIS), and Clouds and the Earth's Radiant Energy System (CERES). Aqua with an orbital altitude of 705 km is in a near-polar sun-syncronous orbit, ascending the equator at 1:30 pm local time.

3.2.1 MODIS

MODIS is one of the major instruments on board the EOS Aqua satellite, measuring various important properties including clouds, aerosols, water vapor, land, and ocean. It measures 36 discrete spectral bands between 0.41 and 14.2μm, with three spatial resolutions of 250m (bands 1-2), 500m (bands 3-7), and 1000m (bands 8-36). MODIS data are provided at three processing levels from level-1 (radiances and brightness temperature) to level-2 (retrieved geophysical properties) to level-3 (daily, eight-day, and monthly global averages gridded $1^{o}\times1^{o}$) [Platnick et al., 2003; King et al., 2003]. There are 20 reflected solar bands and 16 thermal emissive bands. In this study, the cirrus reflectance at 1.38 μm from June 2005 to May 2006 was primarily used. The reason for selection of this band will be discussed in section 3.3.1.

3.2.2 AIRS

AIRS is a high-resolution spectrometer that measures the infrared spectral region from 3.75 to 15.4 μm (2378 spectral channels), with a horizontal spatial resolution of

13.5 km and four other channels which measure visible and near-infrared radiation from 0.4 to 0.94 μm, with a horizontal spatial resolution of 2.3 km. AIRS primarily gives humidity and temperature profiles in the atmosphere. Additionally, it provides cloud properties such as cloud fraction, cloud top height, and cloud liquid water content and also provides surface temperature and emissivity, and total ozone column.

3.3 Methodology

3.3.1 Retrieval of cirrus reflectance using 0.66 μm and 1.38 μm

Cirrus clouds are usually present in the upper troposphere or lower stratosphere. Over 90 % of total water vapor in the atmosphere is located under cirrus clouds [Gao et al., 1995]. Thus, 1.38 μm channel receives very little reflected radiance from the surface or lower atmosphere if there are no high level cirrus clouds because almost all radiances in the 1.38 μm band are absorbed by water vapor in the lower atmosphere. However, if cirrus clouds exist, this channel receives a significant amount of signals due to the reflection on the cirrus clouds and little absorption by water vapor above the cirrus clouds. To show the effect of absorption of 1.38 μm by water vapor, the two-way transmittance is calculated using MODTRAN for tropical atmosphere. Figure 3.1 shows the two-way clear-sky transmittance calculated by DISORT from 1.2 μm to 1.6 μm at 0, 5, 10, and 20 km. The standard tropical atmospheric profile was used and the clear-sky transmittance was calculated by a line-by-line method. The radiance of 1.38 μm was absorbed so strongly that the radiance reflected from the surface can not reach the top of atmosphere.

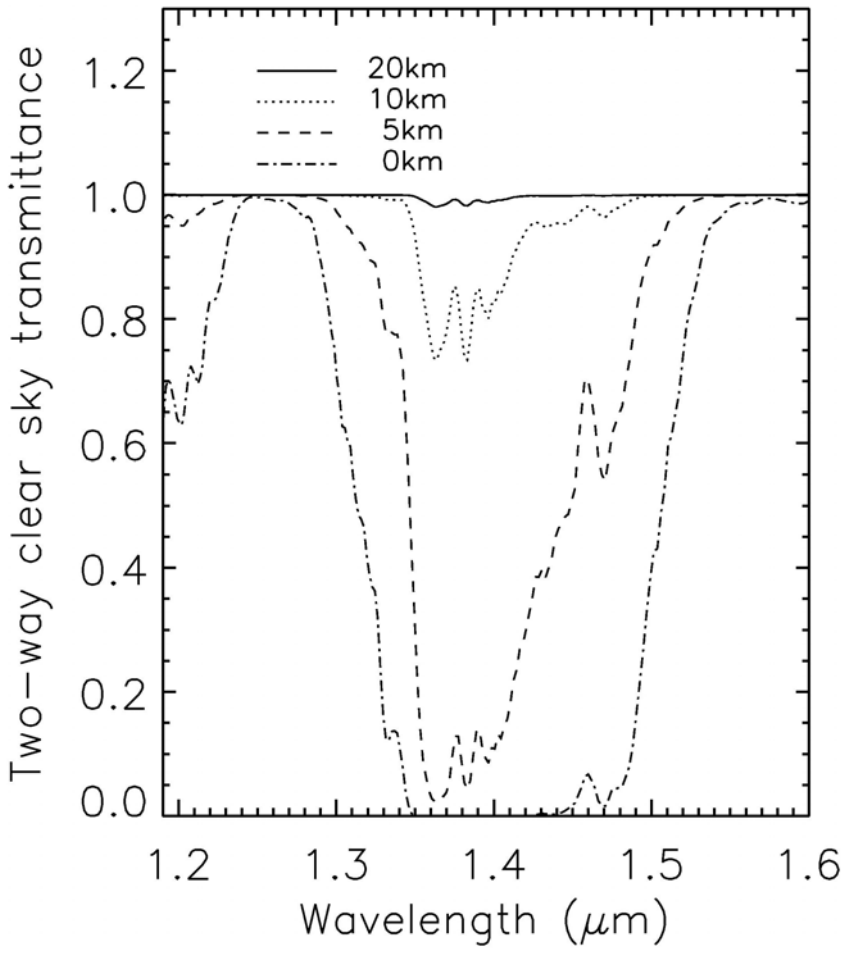

Figure 3.1 Two way transmittance of 1.38 μm.

Gao et al. [2002] developed a straightforward method to retrieve cirrus reflectance. The reflected radiance at 1.38 μm measured by satellite, $r_{1.38}$, can be expressed as follows

$$r_{1.38} = \tilde{t}(\mu_0) r_{c,1.38} \tilde{t}(\mu) = \Gamma_{1.38} r_{c,1.38} \tag{3.1}$$

where $\tilde{t}$ is the transmittance, $r_{c,1.38}$ is the reflectance at the cirrus clouds, $\Gamma_{1.38}$ is the two-way transmittance, and μ_0 and μ are the cosine of the solar zenith angle and satellite zenith angle, respectively. However, the 0.66 μm is a visible channel and is essentially not affected by water vapor absorption. Practically, the two-way transmittance of water vapor at 0.66 μm band, Γ0.66, is 1. But, the 0.66 μm band is strongly affected by the surface reflection. Based on the theory of radiative transfer, the reflectance measured by the satellite at the 0.66 μm band, $r_{0.66}$, including the effect of surface reflection and lower atmosphere, can be expressed as

$$\begin{aligned} r_{0.66} &= r_{c,0.66} + \tilde{t}_c(\mu_0) r_s \tilde{t}_c(\mu) + \tilde{t}_c(\mu_0) r_s^2 \bar{r}_c \tilde{t}_c(\mu) + \tilde{t}_c(\mu_0) r_s^3 \bar{r}_c^2 \tilde{t}_c(\mu) + \cdots \\ &= r_{c,0.66} + \tilde{t}_c(\mu_0) \frac{r_s}{1 - \bar{r}_c r_s} \tilde{t}_c(\mu) \\ &= r_{c,0.66} + b \end{aligned} \tag{3.2}$$

where $\tilde{t}_c$ is the cirrus transmittance, r_s is the surface reflectance, $\bar{r}_c$ is the cirrus reflectance for the upward radiance at the bottom of cloud layer. Moreover, it is known that there is a linear relationship between the reflectance of cirrus clouds at 0.66 μm and 1.38 μm [Gao et al., 1998] such that

$$r_{c,1.38} = a r_{c,0.66}. \tag{3.3}$$

The following relationship can be obtained by substituting (3.3) into (3.1)

$$r_{1.38} = \Gamma_{1.38} a r_{c,0.66} . \tag{3.4}$$

Then, the reflectance at 0.66 μm band and 1.38 μm band can be shown by substituting (3.2) into (3.4)

$$\begin{aligned} r_{1.38} &= \Gamma_{1.38} a (r_{0.66} - b) \\ &= c_1 r_{0.66} + c_2 \end{aligned} \tag{3.5}$$

where $c_1 = a\Gamma_{1.83}$ and $c_2 = -ab\Gamma_{1.38}$, respectively. c_1 and c_2 can be determined from the scatter plot of $r_{1.38}$ and $r_{0.66}$. Finally, cirrus reflectance, $r_{c,0.66}$, can be calculated from (3.4) using $r_{1.38}$ and slope, c_1. The points along slope, c1, represent a reflection from homogeneous surface. Here, c_2 depends on the surface reflectance and lower atmosphere characteristic. Thus, the points in the scatter plot disperse along the 0.66 μm reflectances if the surface property is not homogeneous.

3.3.2 Retrieval of optical depth of tropical thin cirrus clouds

The radiative transfer equation for the scattering atmosphere can be expressed as [Liou, 2002]

$$\mu \frac{dI(\tau;\mu,\phi)}{d\tau} = I(\tau;\mu,\phi) - J(\tau;\mu,\phi) \tag{3.6}$$

where I is radiance, τ is optical depth, μ is the cosine of zenith angle of scattered direction, ϕ is the azimuth angle of scattered direction, and the source function, J, is defined by

$$J(\tau;\mu,\phi)=\frac{\tilde{\omega}}{4\pi}\int_0^{2\pi}\int_{-1}^{1} I(\tau;\mu',\phi')P(\mu,\phi;\mu',\phi')d\mu'd\phi'$$

$$+\frac{\hat{\omega}}{4\pi}F_{\circ}P(\mu,\phi;-\mu_0,\phi_0)e^{-\tau/\mu_0}+(1-\tilde{\omega})B[T(\tau)]. \quad (3.7)$$

Here, $\tilde{\omega}$ is a single scattering albedo, P is a scattering phase function, F_o is the solar irradiance at the top of atmosphere, μ_0 is the cosine of solar zenith angle, ϕ_0 is the solar azimuth angle, and B is a radiant intensity. In source function, J, the first term on the right hand side represents a multiple scattering, second term shows a single scattering, and the third term is an emission from the layer.

For the optically thin layer, the single scattering of direct solar beam contributes most of the scattering event. Thus, the source function can be approximated as

$$J(\tau;\mu,\phi)\cong\frac{\hat{\omega}}{4\pi}F_{\circ}P(\mu,\phi;-\mu_0,\phi_0)e^{-\tau/\mu_0}. \quad (3.8)$$

If we assume no reflected radiances from the bottom of atmosphere, the upward radiance at the top of atmosphere is

$$I(0;\mu,\phi)=\int_0^{\tau_*} J(\tau';\mu,\phi)e^{-\tau'/\mu}\frac{d\tau'}{\mu}$$

$$=\frac{\mu_0 F_{\circ}}{\pi}\frac{\tilde{\omega}}{4(\mu+\mu_0)}P(\mu,\phi;-\mu_0\phi_0)\left\{1-\exp\left[-\tau_*\left(\frac{1}{\mu}+\frac{1}{\mu_0}\right)\right]\right\} \quad (3.9)$$

where τ_* is the total atmospheric optical depth. If τ_* is small, $I(0;\mu,\phi)$ becomes

$$I(0;\mu,\phi)\cong\frac{\mu_0 F_{\circ}}{\pi}\frac{\tilde{\omega}}{4\mu\mu_0}\tau_* P(\mu,\phi;-\mu_0\phi_0). \quad (3.10)$$

Then, the bidirectional reflectance, R, is obtained by

$$R(\mu,\phi;\mu_0,\phi_0)=\frac{\pi I(0;\mu,\phi)}{\mu_0 F_\circ}=\tau_*\frac{\tilde{\omega}}{4\mu\mu_0}P(\mu,\phi;-\mu_0\phi_0)\,. \tag{3.11}$$

The optical depth of thin cirrus clouds from MODIS 1.38 μm reflectance, $r_{c,1.38}$, can be calculated using equation (3.11)

$$\tau=r_{c,1.38}\frac{4\mu\mu_0}{\tilde{\omega}P(\mu,\phi;-\mu_0\phi_0)}\,. \tag{3.12}$$

The phase function in this study comes from Yang et al. [2001] with a mean maximum dimension of 20.6 μm and an effective size of 8.9 μm. The ice particle habit considered is a mixture of bullet rosettes, hollow columns, aggregates, and hexagonal plates which is consistent with MODIS Collection 4 cloud products (Platnick et al. [2003]).

Dessler and Yang [2003] pointed out the limitations of this method. Because the reflectance from upper level cirrus is so small that the reflection from bright and dry regions, such as deserts where the reflected radiances is not fully absorbed by water vapor, might mix signals with true cirrus reflection. Thus, this calculation is confined to the cloud free pixels over the ocean where the surface reflectance is relatively constant and small. Dessler and Yang [2003] also analyzed the error sources coming from measured $r_{1.38}$, conversion from $r_{1.38}$ to $r_{c,1.38}$, and conversion from $r_{c,1.38}$ to optical depth and determined that the detection limit of optical depth by this method is 0.02. If the retrieved optical depth is larger than 0.02, it shows a thin cirrus cloud.

3.3.3 Radiative model simulation

To investigate the radiative forcing of thin cirrus clouds, the shortwave and longwave fluxes at the top and bottom of atmosphere are calculated using Libradtran radiative transfer code [Mayer and Kylling, 2005] with the AIRS atmospheric profile data and corresponding thin cirrus optical depth. The background gaseous absorption properties are calculated according to the atmospheric profiles using a correlated k-distribution method by Fu and Liou [1992]. The solar spectrum from 2.0 μm to 4.0 μm is divided into 9 bands and the infrared spectrum from 4.0 μm to 10000 μm is divided into 12 bands. The transmittance in each band is calculated from the integration of spectral transmittance within the band. The LibRadtran code includes the effects of H_2O, O_2, O_3, CO_2, and NO_2. The profiles of temperature, H_2O, and O_3 are obtained from AIRS monthly retrieval products. Since AIRS does not produce atmospheric profiles higher than 100 hPa for water vapor and 1 hPa for other profiles, standard tropical atmospheric profiles are used above maximum AIRS levels. Also, profiles of other gases such as O_2, CO_2, and NO_2 are obtained from the standard tropical atmosphere. These profiles are interpolated into 100 layers in the model and a thin cirrus clouds layer is inserted as one layer. The single scattering properties of ice clouds are parameterized with respect to effective radius for each spectral band. Those simulated fluxes with corresponding atmospheric profiles and optical depth were analyzed to investigate the cirrus cloud's radiative impact.

3.4 Results

3.4.1 The temporal and spatial distribution of tropical thin cirrus clouds

The temporal and spatial distributions of mean optical depth of thin cirrus clouds and their frequency of occurrence are analyzed for the period of June 2005 to May 2006 to help determine the locations of maximum and minimum occurrences of thin cirrus clouds and to examine the characteristics of their seasonal variations.

To examine the frequency of occurrence of tropical thin cirrus clouds, the seasonal variations of clear-sky fraction of observations with optical depth larger than 0.02 are plotted in Figure 3.2. The fraction is calculated on 1° × 1° latitude and longitude boxes. High fraction occurs in the northern hemisphere during spring and summer and in the southern hemisphere during autumn and winter. In spring, the high fraction occurs over the western Pacific around Indonesia. The fraction is larger than 50 % over the most of the northern hemisphere oceans whereas the fraction is smaller than 30 % over the southern hemisphere oceans. Over the western Pacific, the high fraction exists around deep convection regions. Thus, these retrieved cirrus clouds can be the outflow from the convective anvil cirrus. The fraction of observations for summer show similar spatial distributions to those for spring. High fraction exists over the western Pacific, the Persian Gulf, and Central America and low fraction occurs over the southeastern Pacific and the southern Indian Ocean. The occurrences of high fraction are still around the western Pacific but move southward in autumn. The southern hemisphere oceans show high fraction while the northern hemisphere oceans show less than 30 % of occurrence. Other high fraction regions are off the west coast of South America and off the west

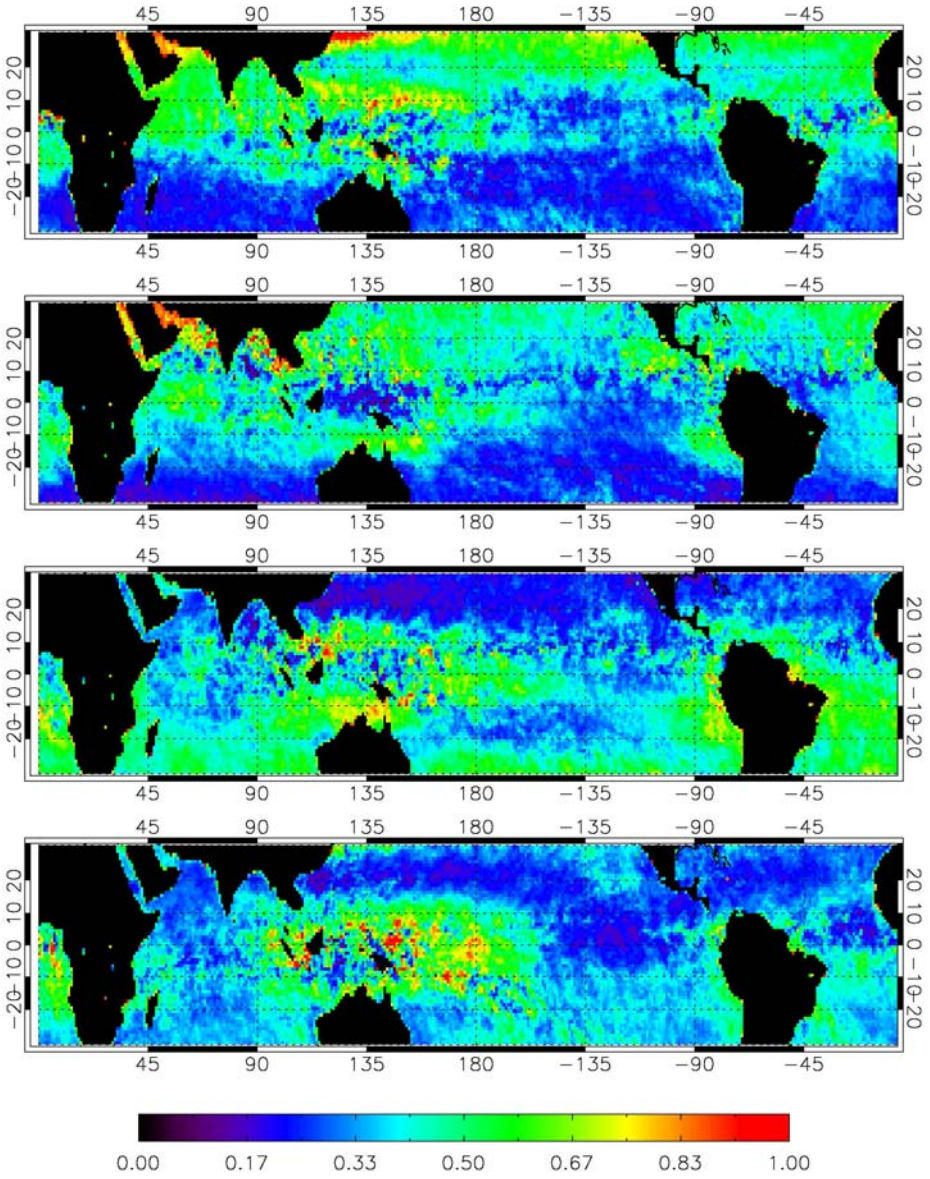

Figure 3.2 Fraction of "clear-sky" observations for 1°×1° boxes that have detectible thin cirrus (optical depth exceeds 0.02) for each season (spring, summer , autumn, and winter from top to bottom panel).

coast of Africa. The high fraction occurs over the western Pacific during winter the same as in autumn and low fraction widely exists over northern hemisphere oceans.

Figure 3.3 shows the histograms of optical depth for each season. Fraction is calculated at every 0.005 of optical depth for each season. Every distribution shows a similar pattern where the fraction increases sharply until optical depth is 0.01, decreases rapidly until 0.04, and decrease gradually at large optical depths. Using τ=0.02 as a detection limit as explained in section 3.3.2, 44%, 39%, 47%, and 44% of the observations flagged as cloud-free have detectible thin cirrus clouds during spring, summer, autumn, and winter, respectively.

Figure 3.4 shows the spatial distributions of optical depth of tropical thin cirrus clouds for the pixels flagged as clear-sky with an optical depth larger than 0.02 for each season. The optical depth is averaged over 1° × 1° boxes, the same as in fraction of observations. The pattern of optical depth is very similar to that of fraction of observations. Large optical depth occurs over the western and northern Pacific and small optical depth exists over the southern hemisphere oceans during spring. In summer, large optical depth appears widely over the western Pacific, the northern Indian Ocean, and Central America while southern hemisphere ocean areas have small optical depths. The locations of large optical depth still exist over the western Pacific but migrate southward during autumn. Large optical depth also appears off the west coast of South America. The pattern of spatial distributions of optical depth for winter is similar to those for autumn. Large optical depth exists over the western Pacific and off the west coast of Africa.

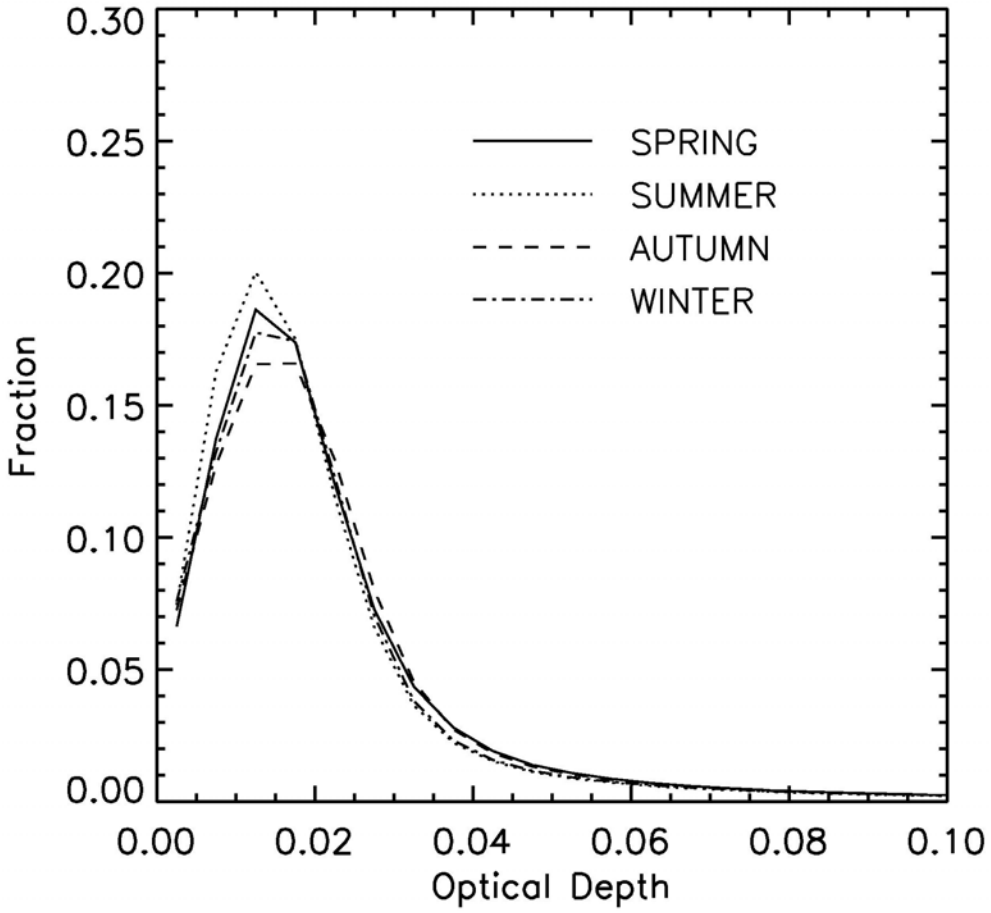

Figure 3.3 Histograms of optical depth for each season.

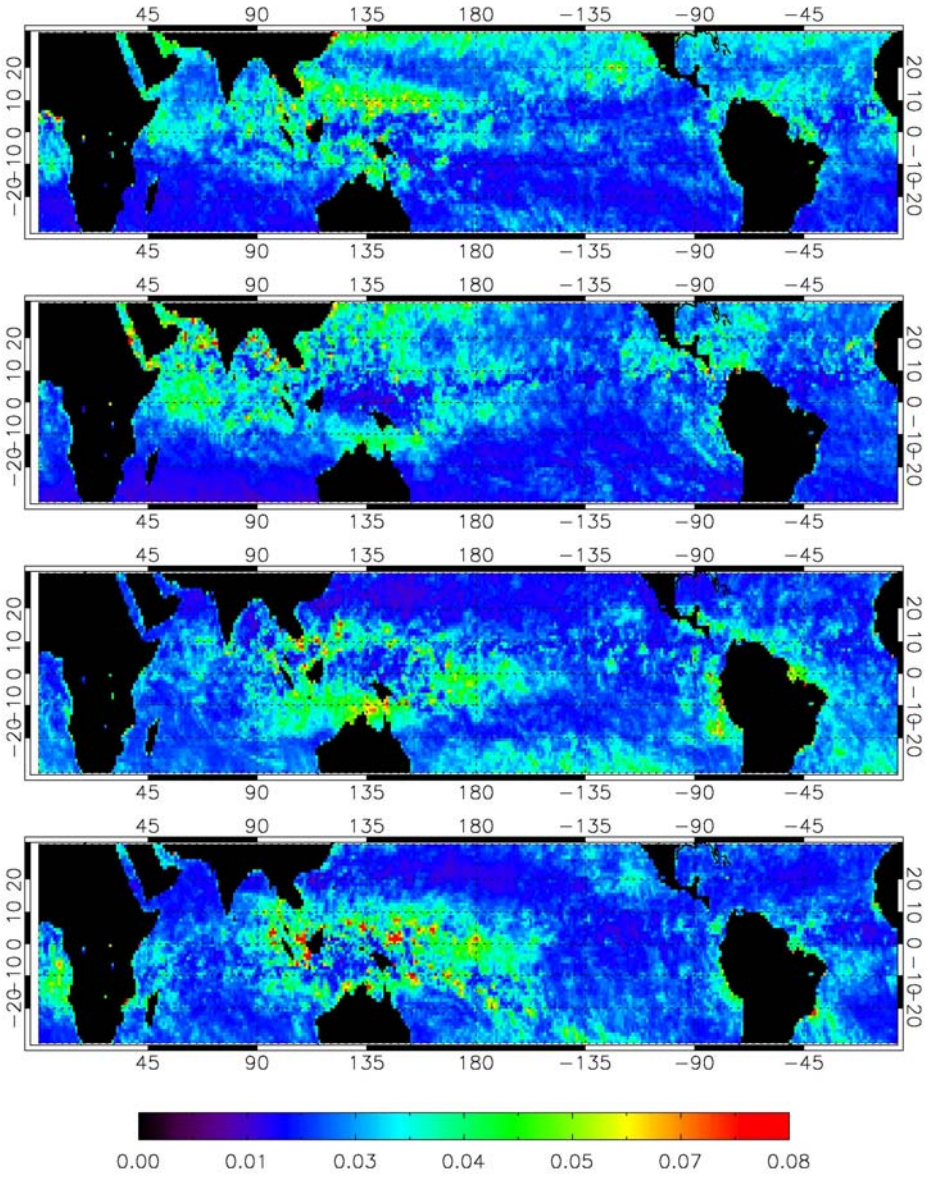

Figure 3.4 Optical depth of tropical thin cirrus for the pixels flagged as “clear-sky” by MODIS for each season (spring, summer, autumn, and winter from top to bottom panel).

Figure 3.5 shows the relationship between optical depth and fraction for each season. It is clearly seen that there is a positive relation between optical depth and fraction with a larger variance at higher optical depths and fractions. The optical depth becomes larger where thin cirrus clouds occur more frequently.

The zonal averaged fraction of observation and optical depth are plotted in Figure 3.6. The fraction of observation and optical depth is averaged over every 1° latitude from 30°S to 30°N. It is more clearly seen that the latitudinal variations of fraction of observations and optical depths with the season. The high fraction and large optical depth exist in northern hemisphere high latitudes and decrease toward the south during spring and summer. On the other hand, the high fraction and large optical depth appear in southern hemisphere high latitudes and decrease toward the north during autumn and winter.

3.4.2 Parameterization of ice cloud optical and microphysical properties

The radiative effect of ice clouds has a strong influence on weather and climate due to the frequent occurrence of ice clouds in the atmosphere. The rdiative properties of ice clouds are determined by their microphysical and optical properties. Thus, it is necessary to parameterize the optical and microphysical properties of ice clouds for the study of their effect on weather and climate. The microphysical properties of ice clouds include particle shape, particle size distribution, ice water content, and effective size. The optical properties of ice clouds include single scattering properties, asymmetry parameter, extinction efficiency, absorption efficiency, and phase function.

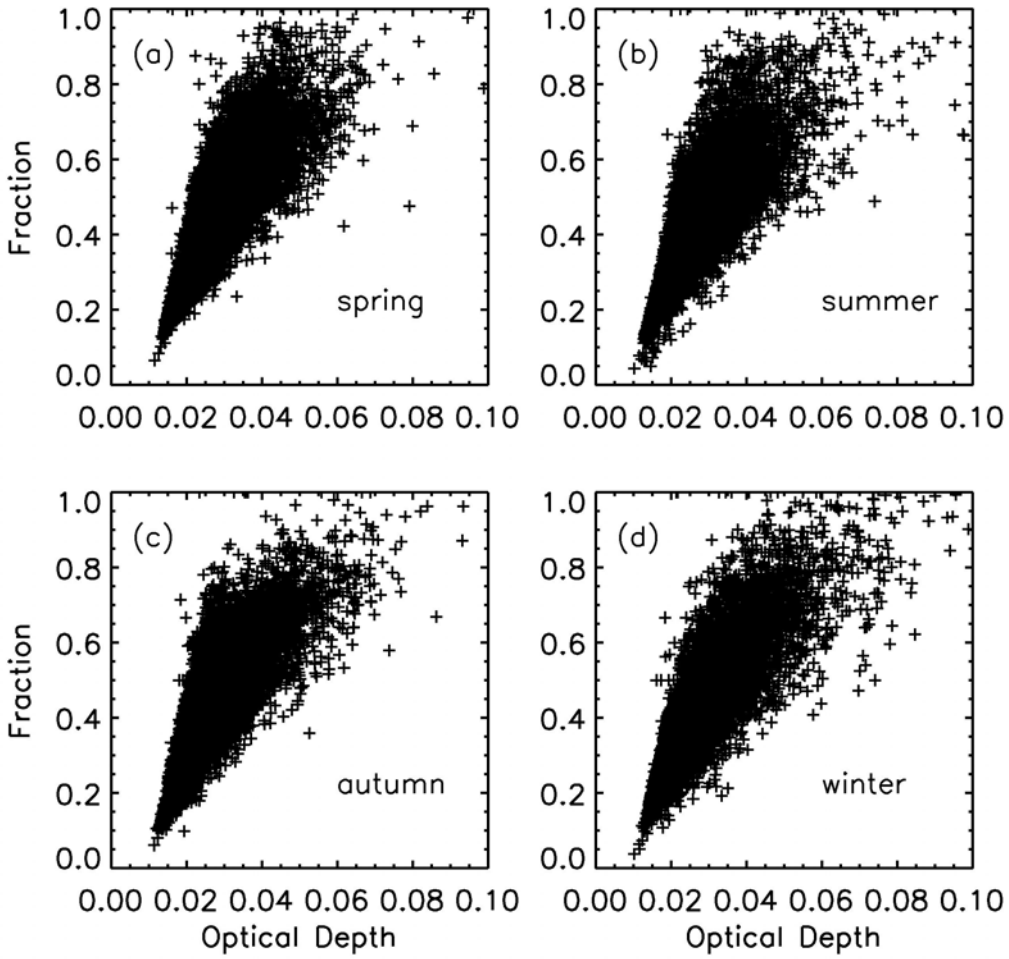

Figure 3.5 Relationship of optical depth and fraction of observations for (a) spring, (b) summer, (c) autumn, (d) winter.

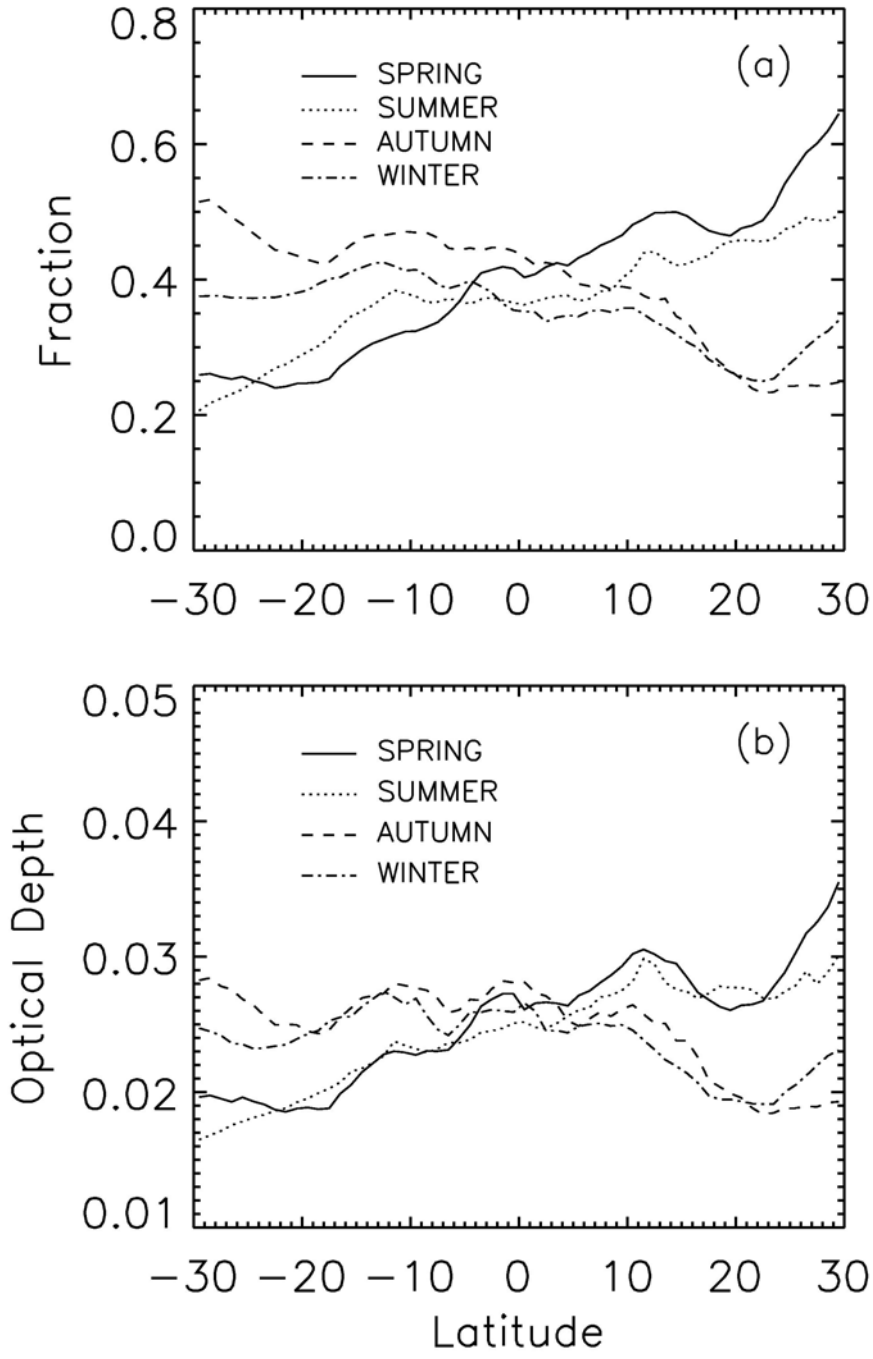

Figure 3.6 Zonally averaged (a) fraction of observations and (b) optical depth for each season.

Fu and Liou [1993] parameterized the optical properties of ice crystals as a function of the mean effective size in 6 solar bands and 12 infrared bands for 11 size distributions. The single scattering properties were calculated from a geometric ray-tracing technique for small hexagonal ice crystals and a Mie calculation for large spheroids. Fu [1996] also parameterized the single scattering properties of hexagonal ice crystals in terms of generalized effective size in 25 solar bands for 28 ice crystal distributions using improved light scattering calculations. Another effort to parameterize single scattering properties of ice crystal was done by Yang et al. [2000]. They parameterized the single scattering properties in 56 solar bands for six ice crystal shapes including hexagonal plates, solid and hollow columns, planar and spatial bullet rosettes, and aggregates. Key et al. [2002] parameterized the single scattering properties in the form of third-degree polynomials as a function of effective radius in 56 solar bands for seven particle habits by adding dendrites to the six particle shape of Yang et al. [2000]. The parameterization in this study is basically the expansion of the parameterization by Key et al. [2002] for 26 bands in solar spectrum region (0.2 μm ~ 0.5 μm) and 39 bands in infrared spectrum region (5.0 μm ~ 100 μm). Particle habits considered in the parameterization are droxtal, solid columns, hollow columns, hexagonal plates, bullet rosettes, aggregates and habit mixture. This study uses Fu's [1996] 30 size distributions, which were acquired from various field experiments such as the First International Satellite Cloud Climatology Project Regional Experiment (FIRE I and FIRE II) and the Central Equatorial Pacific Experiment (CEPEX). In these size distributions, each size

distribution is divided into 38 size bins according to maximum dimensions from 2 μm to 3100 μm.

3.4.2.1 Bulk single scattering properties

The single scattering properties of each particle shape are integrated over size distributions at each size bin and at each wavelength band. This process produces the bulk (mean) single scattering properties of ice particles for each size distribution. Each size distribution has corresponding values of effective size, ice water content, volume extinction coefficient, single scattering albedo, asymmetry parameter, and phase function at each wavelength band. Then, a nonlinear regression procedure is applied for the optical properties as a function of effective radius, R_e.

Following the method of Yang et al. [2001], effective size, D_e, is determined as

$$D_e = \frac{3}{2}\frac{\int_{L_{\min}}^{L_{\max}} V(L)n(L)dL}{\int_{L_{\min}}^{L_{\max}} A(L)n(L)dL} \tag{3.13}$$

where V is volume of the particle, A is projected area of the particle, L is maximum dimension, and $n(L)$ is the number of particles with a maximum dimension L. The parameterization is performed as a function of effective radius, R_e which is a half of effective size and defined as

$$R_e = \frac{3}{4}\frac{\int_{L_{\min}}^{L_{\max}} V(L)n(L)dL}{\int_{L_{\min}}^{L_{\max}} A(L)n(L)dL}. \tag{3.14}$$

The extinction coefficient, β_e and the ice water content of the size distribution, *IWC* is defined as

$$\beta_e = \int_{L_{\min}}^{L_{\max}} Q_e(L)A(L)n(L)dL \tag{3.15}$$

$$IWC = \rho_{ice}\int_{L_{\min}}^{L_{\max}} V(L)n(L)dL\,, \tag{3.16}$$

respectively where Q_e is the extinction efficiency and ρ_{ice} is the density of ice.

The single scattering albedo, ω and asymmetry parameter, g are weighted over extinction and scattering, respectively.

$$\omega = \frac{\int_{L_{\min}}^{L_{\max}} \omega(L)Q_e(L)A(L)n(L)dL}{\int_{L_{\min}}^{L_{\max}} Q_e(L)A(L)n(L)dL} \tag{3.17}$$

$$g = \frac{\int_{L_{\min}}^{L_{\max}} g(L)Q_s(L)A(L)n(L)dL}{\int_{L_{\min}}^{L_{\max}} Q_s(L)A(L)n(L)dL} \tag{3.18}$$

For the habit mixture, the composition of ice particle follows that of Baum et al. [2005a] such as D_e < 60 μm, 100 % droxtals; 60 < D_e < 1000 μm, 15 % bullet rosettes, 50 % solid columns, and 35 % plates; 1000 < D_e < 2000 μm, 45 % hollow columns, 45 % solid columns, and 10 % aggregates; D_e > 2000 μm, 97 % bullet rosettes and 3 % aggregates. The bulk scattering properties of habit mixture are then obtained by multiplying the habit fraction corresponding to the effective size ranges in the integration [Baum et al, 2005b]. For example, the effective size of habit mixture is expressed as

$$D_e = \frac{3}{2}\frac{\int_{L_{\min}}^{L_{\max}} f_i(L)V(L)n(L)dL}{\int_{L_{\min}}^{L_{\max}} f_i(L)A(L)n(L)dL} \tag{3.19}$$

where $f_i(L)$ is the fraction of ice particle habit in the particle size bin. This can be applied to the calculation of other bulk single scattering properties as well.

3.4.2.2 Parameterization of optical properties

The optical properties of ice clouds are parameterized nonlinearly with respect to effective radius, R_e at each wavelength and for each particle shape following Key et al. [2002].

$$\frac{\beta_{ext}}{IWC} = a_0 + a_1\frac{1}{R_e} + a_2\frac{1}{R_e^{\,2}} + a_3\frac{1}{R_e^{\,3}} \tag{3.20}$$

$$\omega = b_0 + b_1 R_e + b_2 R_e^{\,2} + b_3 R_e^{\,3} \tag{3.21}$$

$$g = c_0 + c_1 R_e + c_2 R_e^{\,2} + c_3 R_e^{\,3}\,. \tag{3.22}$$

Figure 3.7 shows the optical properties of habit mixture ice clouds with a function of effective radius at wavelengths of 1.40, 5.00, and 20.0 μm. The value of Extinction/IWC decreases with increasing effective radius and shows almost no dependence on wavelength (Figure 3.7(a)). Single scattering albedo decreases very rapidly with increasing effective radius in infrared region (5 and 20 μm) but is almost 1 at visible wavelength (1.4 μm) (Figure 3.7(b)) while asymmetry parameter increases with effective radius (Figure 3.7(c)). Figure 3.8 is an example of parameterization of

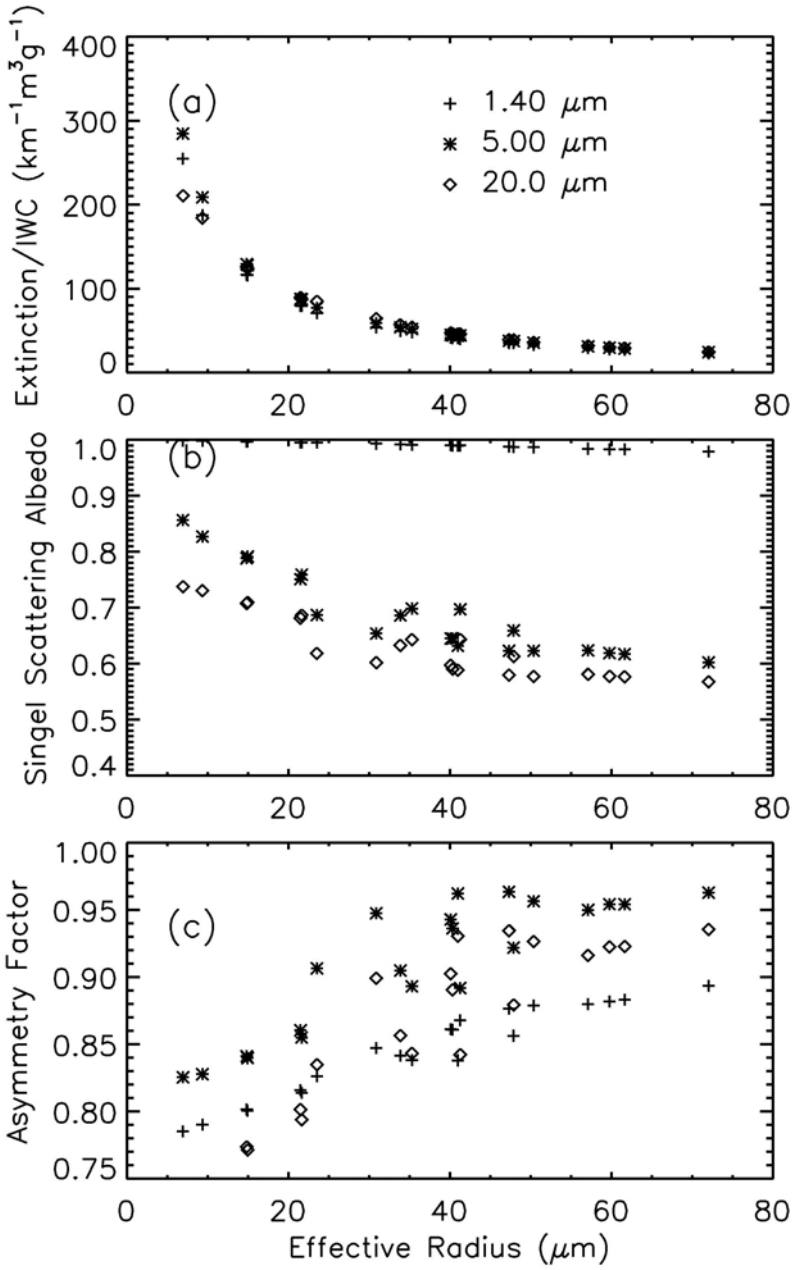

Figure 3.7 Variations of (a) the ratio of extinction coefficient to ice water content, (b) single scattering albedo, and (c) asymmetry factor as a function of effective radius.

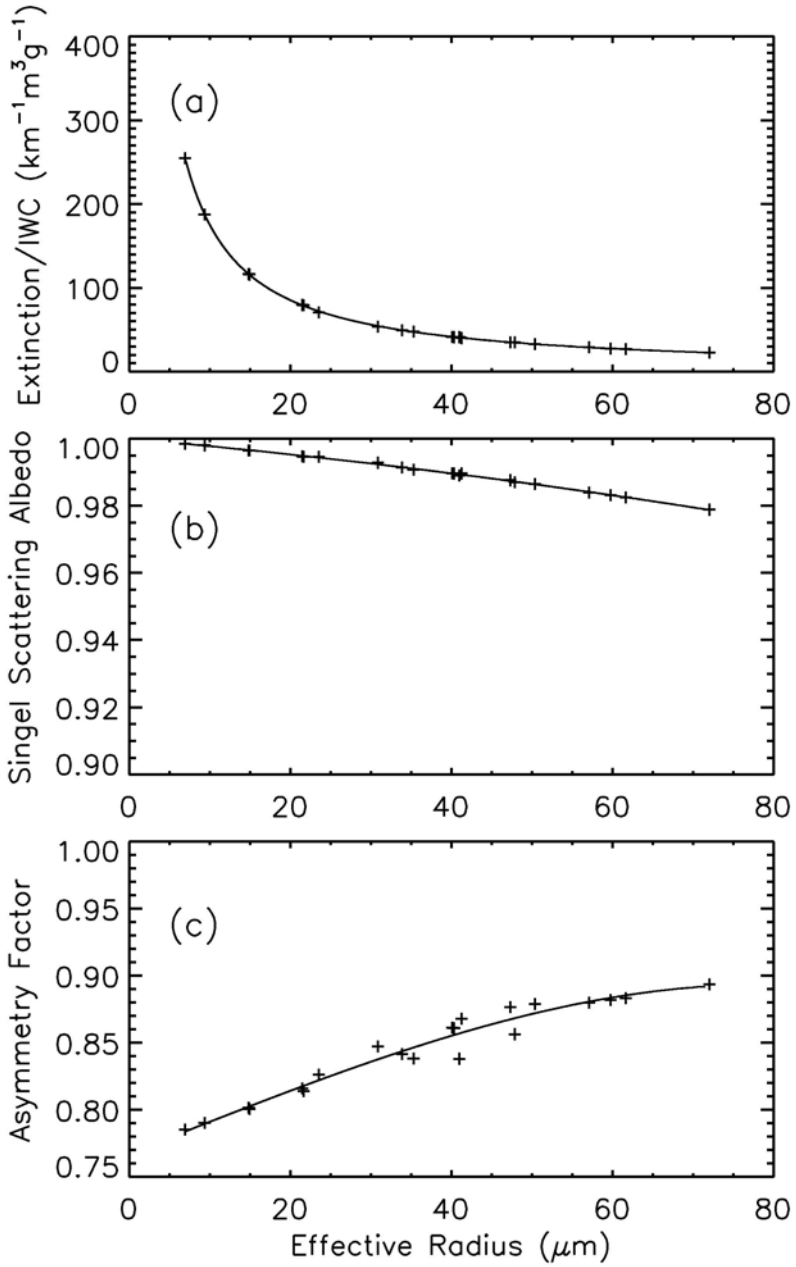

Figure 3.8 An example of parameterization of (a) the ratio of extinction coefficient to ice water content, (b) single scattering albedo, and (c) asymmetry factor as a function of effective radius.

optical properties at 1.40 μm. The parameterization accurately represents the single scattering properties with the effective radius.

The mean (bulk) phase function can be calculated in the same way as an asymmetry factor at each scattering angle, at each wavenumber, and for each ice particle habit. It is appropriate to use the exact phase function for the retrieval of ice clouds' microphysical and optical properties which need the information for scattering angles.

However, it takes time and becomes complicated when using an exact phase function in the flux calculation. Thus, an approximation of phase function is used to meet the balance between calculation time and accuracy. One of the most common approximations of scattering phase function is the Henyey-Greenstein function [Henyey and Greenstein, 1941], P_{HG}, defined as

$$P_{HG}(\theta; g) = \frac{1 - g^2}{(1 + g^2 - 2g\cos\theta)^{3/2}} \tag{3.23}$$

where g is an asymmetry parameter and θ is a scattering angle. Henyey-Greenstein function is a good approximation of scattering phase function for the forward scattering but it is not good for a backward scattering. Double Henyey-Greenstein function, P_{DHG} is proposed to improve the representation of backward scattering such as

$$P_{DHG} = fP_{HG}(\theta; g_1) + (1 - f)P_{HG}(\theta; g_2) \tag{3.24}$$

where g_1 is the same value of g in Henyey-Greenstein function, f represents a fraction of the forward scattering, and g_2 represents the backward scattering. f and g_2 is determined by making the squared differences between real phase function and double Henyey-Greenstein function minimize as following

$$MIN\left[\sum_{\theta_i}\left(\ln P(\theta_i) - \ln P_{DHG}(\theta_i)\right)^2\right]. \quad (3.25)$$

The minimum can be obtained by varying f from 0 to 1 and g_2 from -1 to 0.

Figure 3.9 shows the phase function of 5 different effective sizes at 1.40 μm. The phase function does not increase or decrease consistently with the effective size and has quite different features with respect to the effective size. In Figure 3.10, the double Henyey-Greenstein function is plotted with various values of f fixing g=0.80 and g_2=-0.50 at 1.40 μm. The backward scattering decreases with increasing f as f represents the fraction of forward scattering. Figure 3.11 is same as Figure 3.10 except for various values of g_2 fixing g=0.80 and f=0.95. The backward scattering increases with the increase of absolute value of g_2 which represents the backward scattering. Figure 3.12 shows the comparisons between real phase function, Henyey-Greenstein function, and double Henyey-Greenstein function with the effective size of 61.7 μm, f=0.90, g_1=0.84, and g_2=-0.33 at the wavelength of 1.40 μm. The approximated phase functions do not capture the detailed characteristics of real phase function but they fit real phase function relatively well. The double Henyey-Greenstein function depicts better the backward scattering.

3.4.3 The radiative forcing of thin cirrus clouds

Cloud radiative forcing effect is investigated in many ways using satellite data or surface measurement within the atmosphere, at the top of atmosphere, and at the bottom of atmosphere [e.g., Ramanathan et al., 1989; Rossow and Zhang, 1995; Sohn, 1999;

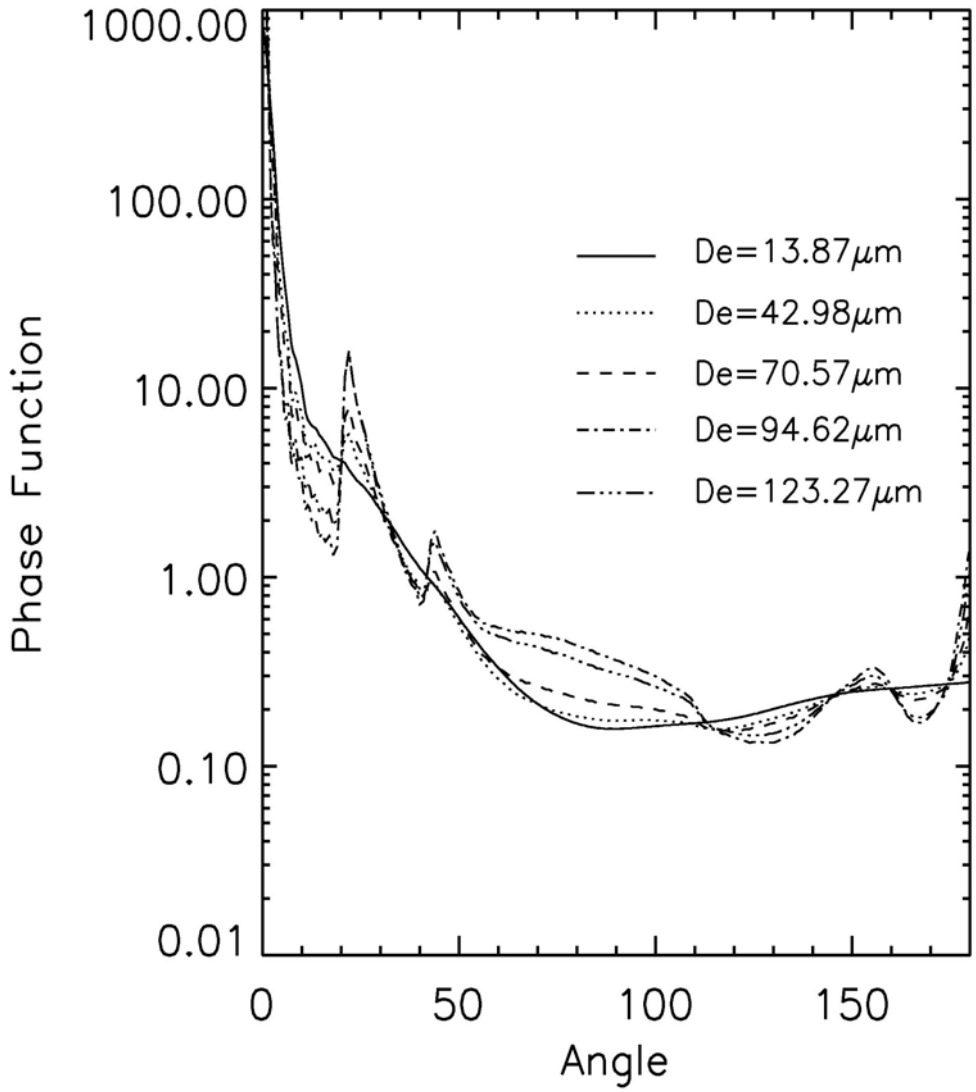

Figure 3.9 Variations of phase function with a different effective size.

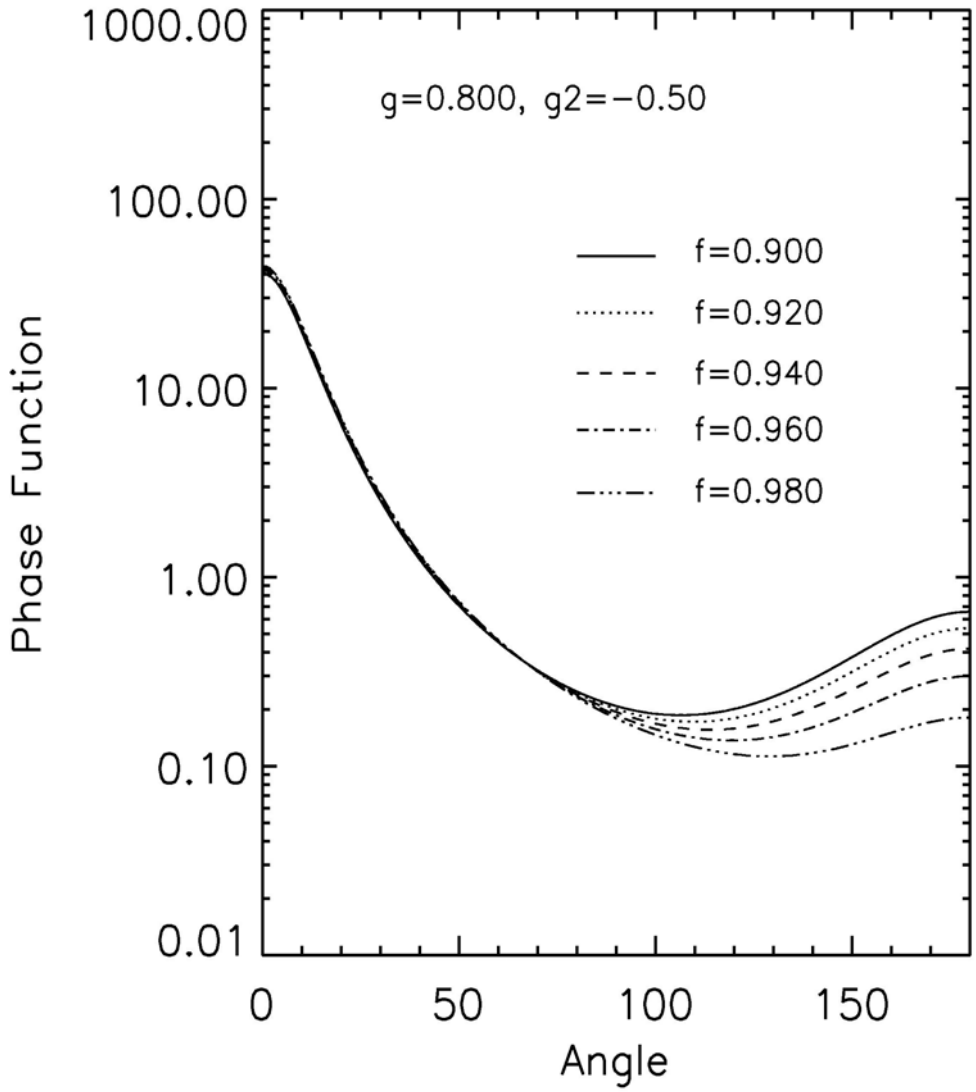

Figure 3.10 Variations of phase function with a different forward scattering factor, *f*.

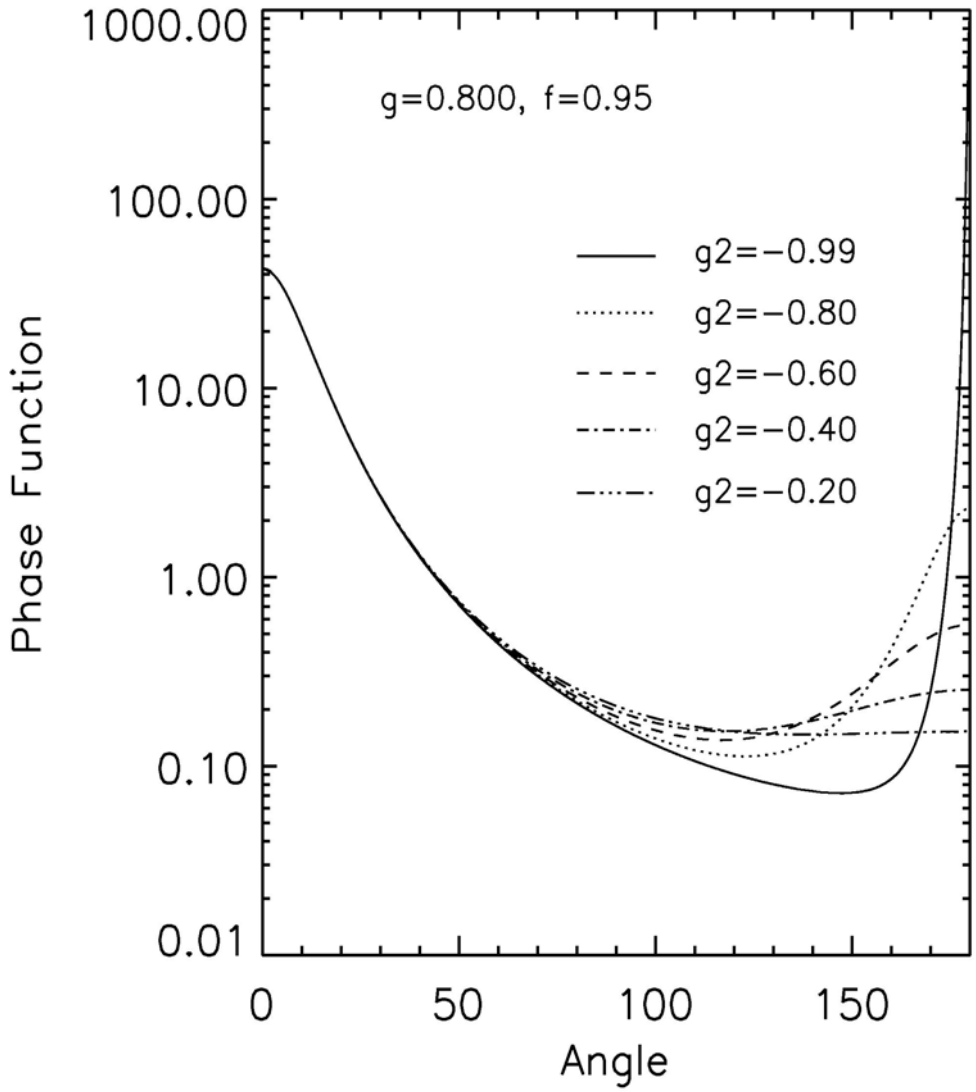

Figure 3.11 Variations of phase function with a different backward scattering factor, g_2.

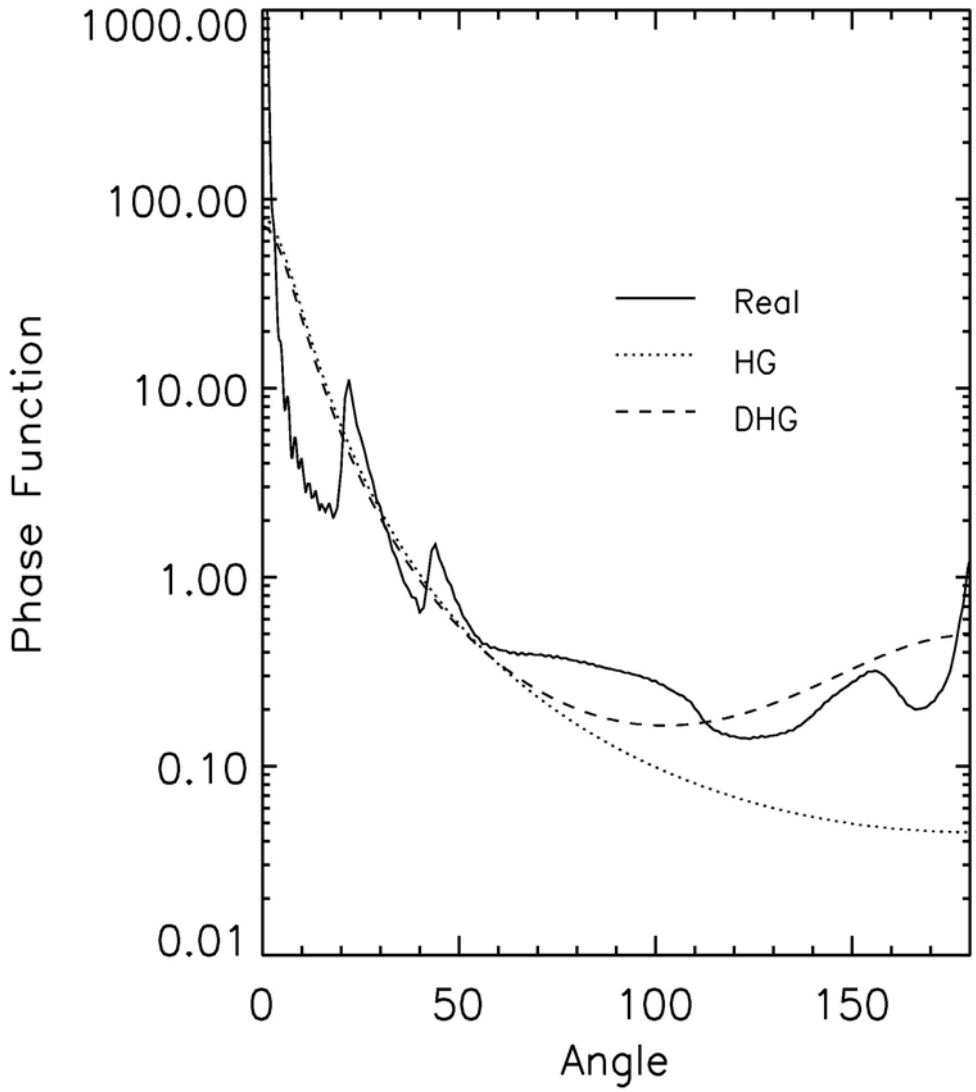

Figure 3.12 Comparisons among real phase function, Henyey-Greenstein function, and double Henyey-Greenstein function.

Choi and Ho, 2006; Mace et al, 2006]. Clouds have warming effect on the surface or atmosphere by longwave emission and cooling effect by reflecting the incident shortwave radiation. The net cloud radiative forcing is determined by the sum of longwave warming effect and shortwave cooling effect. The cloud radiative forcing (CRF) is defined as the net flux difference between cloudy conditions and clear-sky conditions. Thus, the shortwave (CRF_{SW}) and longwave (CRF_{LW}), and net cloud radiative forcing (CRF_{NET}) can be expressed as

$$CRF_{SW} = (F_{SW}{}^{\downarrow} - F_{SW}{}^{\uparrow})_{cld} - (F_{SW}{}^{\downarrow} - F_{SW}{}^{\uparrow})_{clr} \tag{3.26}$$

$$CRF_{LW} = (F_{LW}{}^{\downarrow} - F_{LW}{}^{\uparrow})_{cld} - (F_{LW}{}^{\downarrow} - F_{LW}{}^{\uparrow})_{clr} \tag{3.27}$$

$$CRF_{NET} = CRF_{SW} + CRF_{LW}\,, \tag{3.28}$$

respectively. $F^{\downarrow}$ and $F^{\uparrow}$ represent downward flux and upward flux, respectively.

This study evaluates the cloud radiative forcing at the top and bottom of atmosphere using retrieved optical depth, atmospheric profile from AIRS, and the parameterized single scattering properties of ice clouds. LibRadtran is the radiative transfer model used in this simulation. The cloud layer is assumed to exist between 10 and 12 km. The solar zenith angle from each granule is averaged over 1° × 1° latitude and longitude boxes for every month or for every season.

Figure 3.13 shows the atmospheric longwave heating rate for each shape. A tropical atmospheric profile is used for the simulation and cloud is located between 10 and 12 km. Ice water content of 0.0048 gm^{-3} and effective size of 41.5 μm is used. Cloud induced heating occurs at the lower part of clouds because the longwave emission from

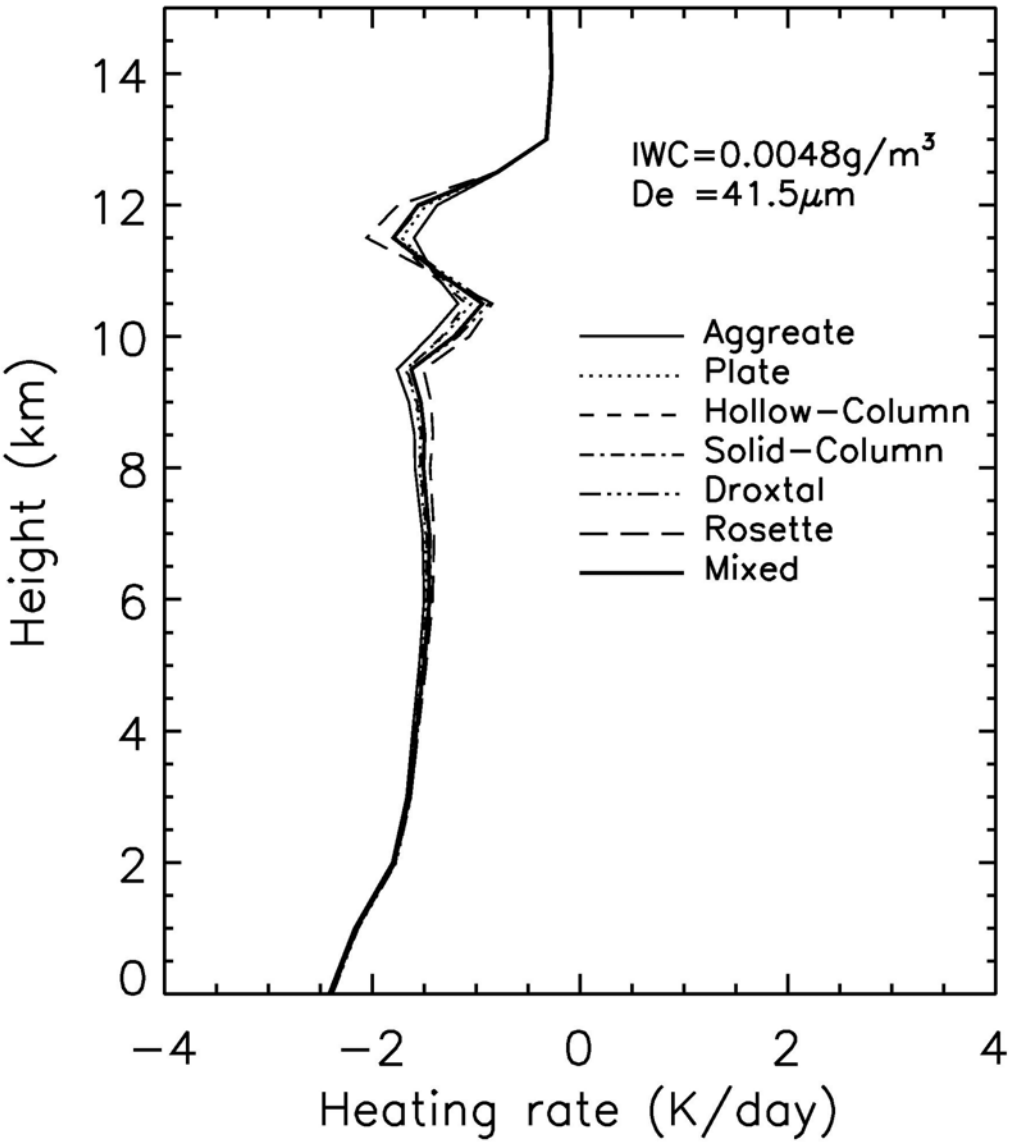

Figure 3.13 Variations of atmospheric heating rate with height for different ice particle habit.

the clouds increases downward flux. In the upper part of clouds, upward longwave flux decreases due to the absorption of longwave flux from the surface by clouds resulting in cloud induced cooling. The difference in heating rate for various ice particle shapes is not large but the heating rate is larger for smaller effective size of ice particle due to a greater surface area per volume leading to the stronger absorption.

Figure 3.14 shows the atmospheric heating rate with respect to ice water content for mixed habit. The heating or cooling rate increases with the larger ice water content because the absorption increases with increasing effective size.

Figure 3.15 shows the cloud radiative forcing at the top and bottom of atmosphere with respect to ice water content by the model simulation. At the top of atmosphere there is a positive longwave forcing and a negative shortwave forcing. The decreased upward longwave flux by the absorption of clouds at the top of atmosphere leads to the positive longwave cloud forcing. On the contrary, the increased upward shortwave flux by the reflection from the clouds results in the negative shortwave cloud forcing. The net forcing is small warming because the positive longwave forcing is larger than the negative shorwave forcing in magnitude. Net warming increases up to ice water content 0.006 gm^{-3} and decreases after that. At the bottom of atmosphere, the longwave radiative effect has a very small positive effect while the shortwave effect shows large negative forcing leading to a net negative forcing. The longwave warming by upper layer thin cirrus clouds has little effect on the surface.

Figure 3.16 (a) shows the $1° \times 1°$ spatial distribution of cloud radiative forcing at the top of atmosphere calculated using retrieved optical depth, AIRS profile, and

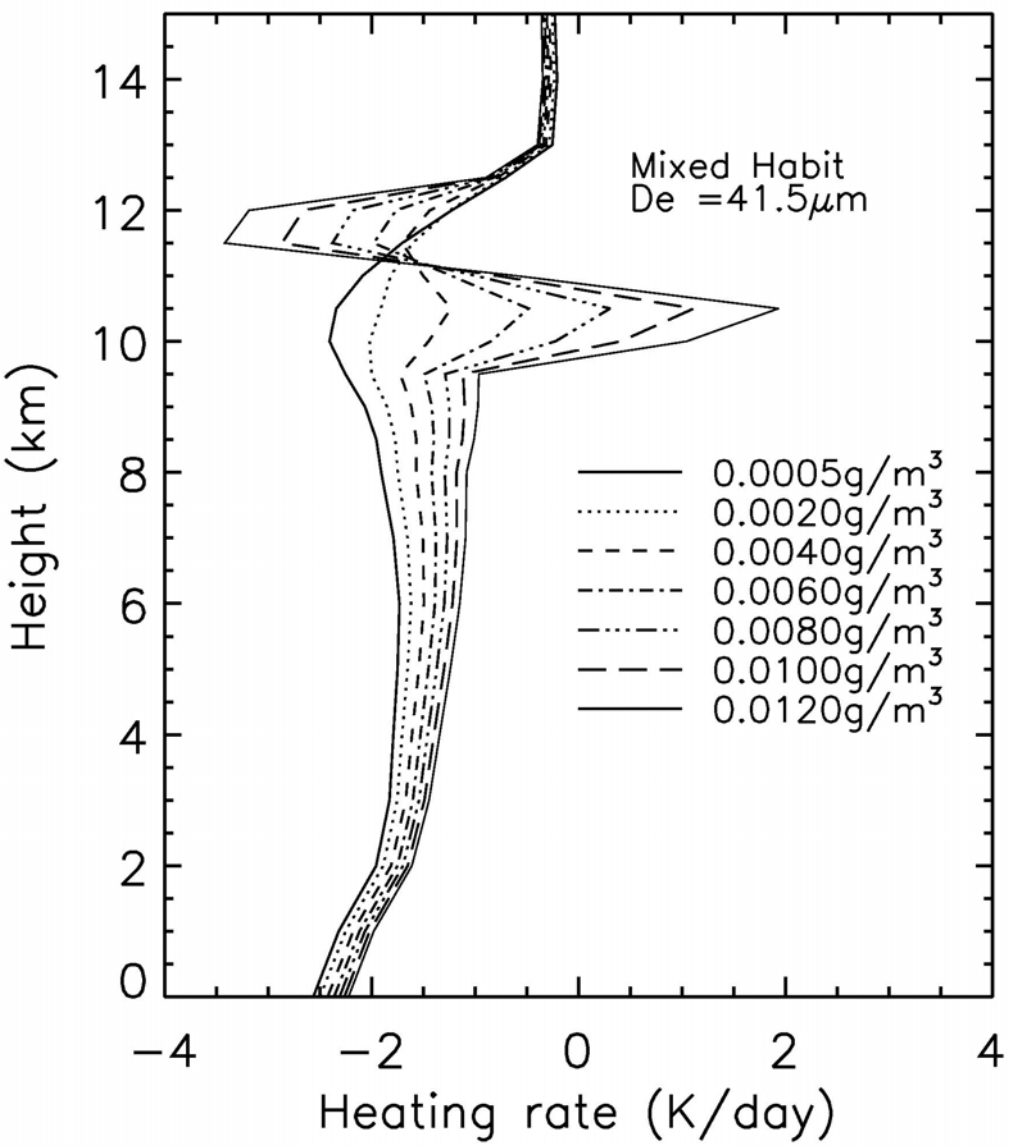

Figure 3.14 Variations of atmospheric heating rate with height for different ice water content.

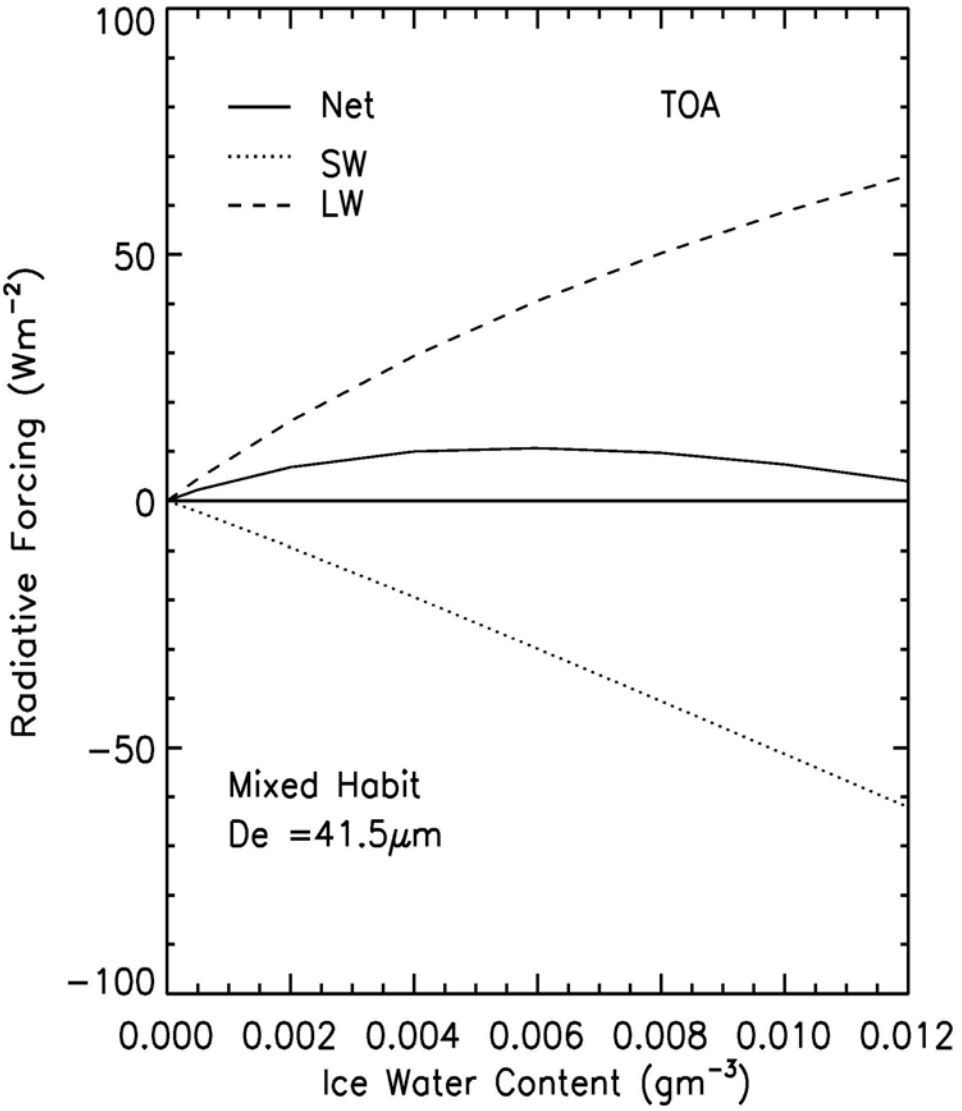

(a)

Figure 3.15 Cloud radiative forcing with ice water content. (a) At the top of atmosphere.

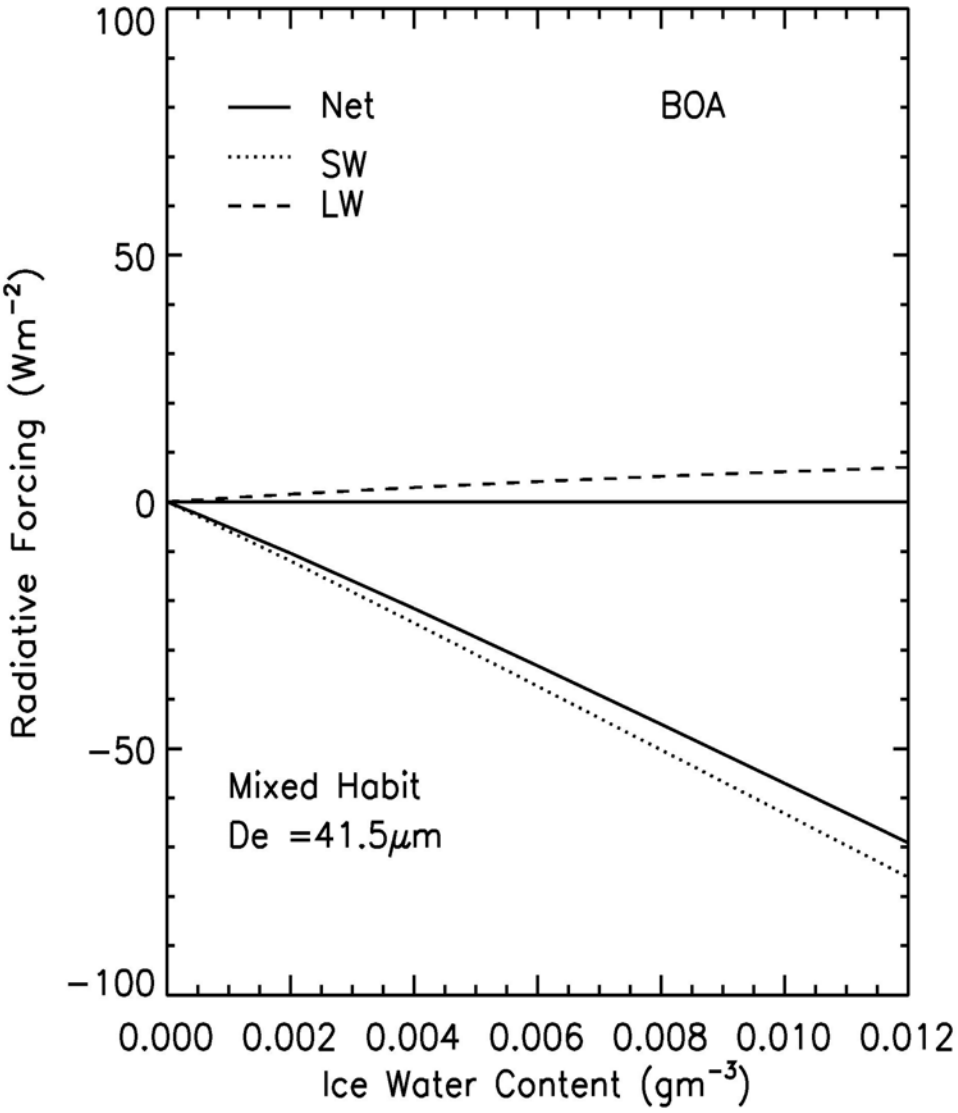

(b)

Figure 3.15 Continued (b) At the bottom of atmosphere.

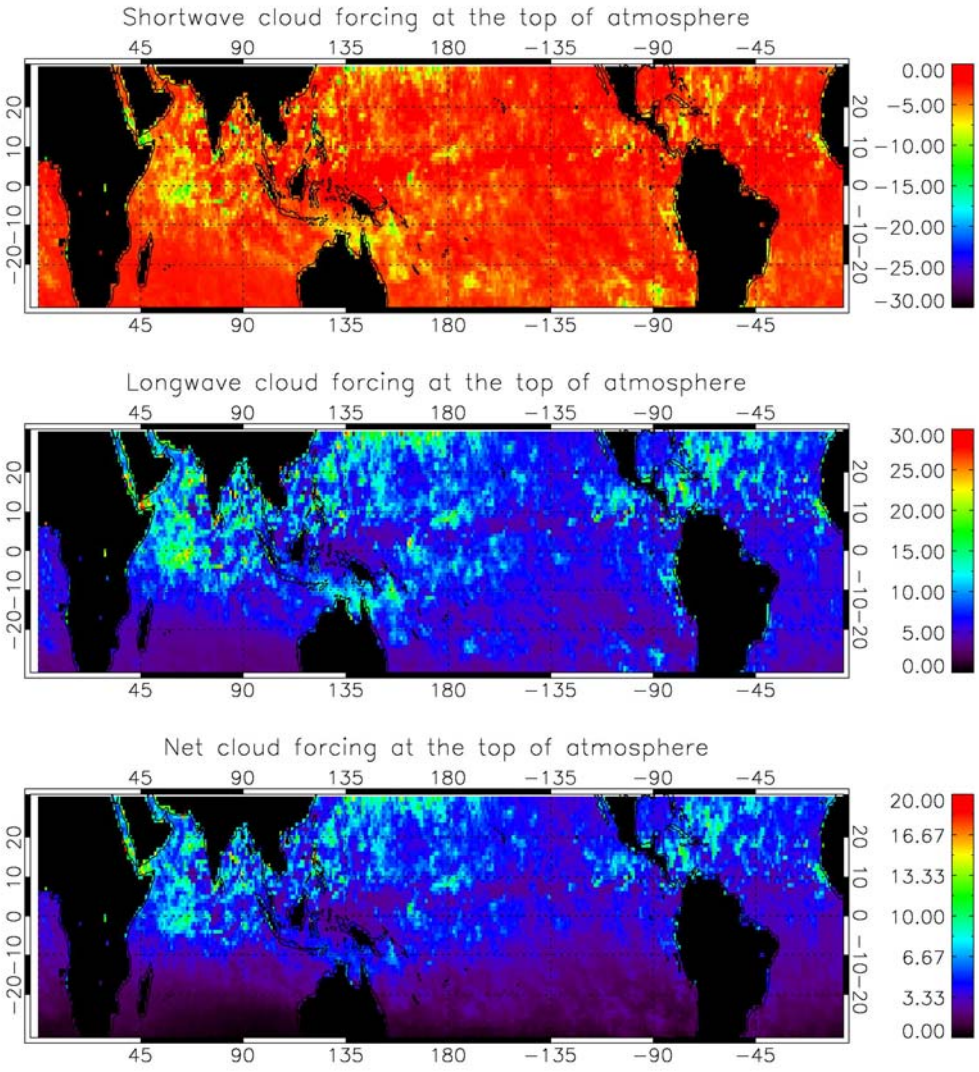

(a)

Figure 3.16 Spatial distribution of cloud radiative forcing (shortwave, longwave, and net forcing from top to bottom panel). (a) At the top of atmosphere for June 2005.

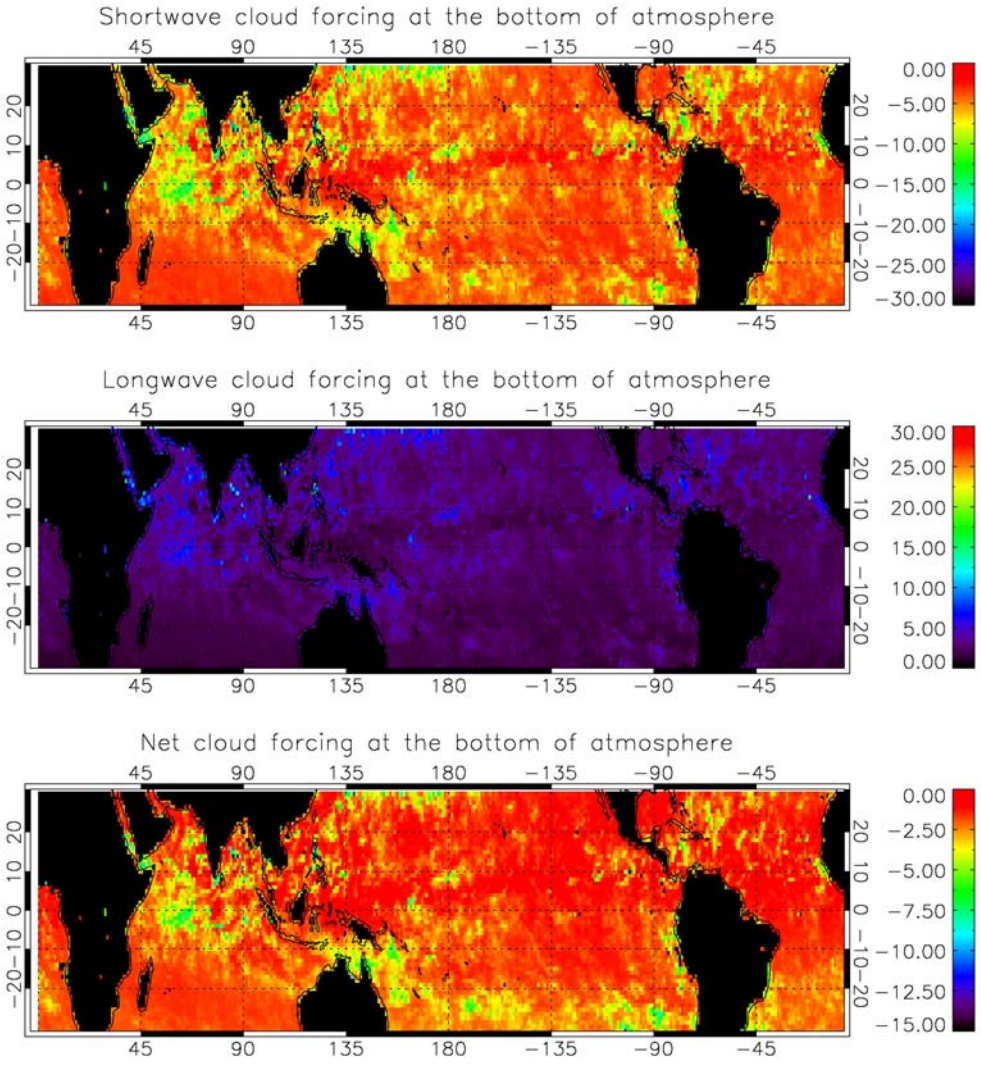

(b)

Figure 3.16 Continued (b) At the bottom of atmosphere for June 2005.

averaged solar zenith angle for June 2006. The large cloud radiative forcing appears around the western Pacific where the optical depth is large. It shows a negative cloud radiative forcing for shortwave, positive forcing for longwave and net positive cloud radiative forcing. The spatial distribution of cloud radiative forcing at the bottom of atmosphere for June is plotted in Figure 3.16 (b). Thin cirrus clouds produce large negative shortwave forcing in the Indian Ocean and the western Pacific Ocean but very small positive longwave forcing at the bottom of atmosphere. Thus, the net cloud forcing shows a negative effect.

Figure 3.17 (a) is the same as Figure 3.16 (a) except for December 2006. In December, the region where large forcing occurs moves southward and locates around Indonesia and north Australia. The net cloud forcing shows a positive effect due to larger positive longwave forcing than shortwave negative forcing. The cloud radiative forcing at the bottom of atmosphere for December is shown in Figure 3.17(b). The region of large cloud forcing is located around Indonesia and the southern Pacific and is the same as at the top of atmosphere. The net cloud forcing shows a negative effect due to a large negative shortwave forcing.

Figure 3.18 shows the relationship between optical depth and cloud radiative forcing obtained from $1° \times 1°$ calculations at the top and bottom of atmosphere. At the top of atmosphere, both shortwave negative forcing and longwave positive forcing becomes larger with the increasing optical depth in magnitude. The net cloud radiative forcing is positive because of the larger positive longwave forcing. The difference in surface temperature and atmospheric profile causes the variance. At the bottom of

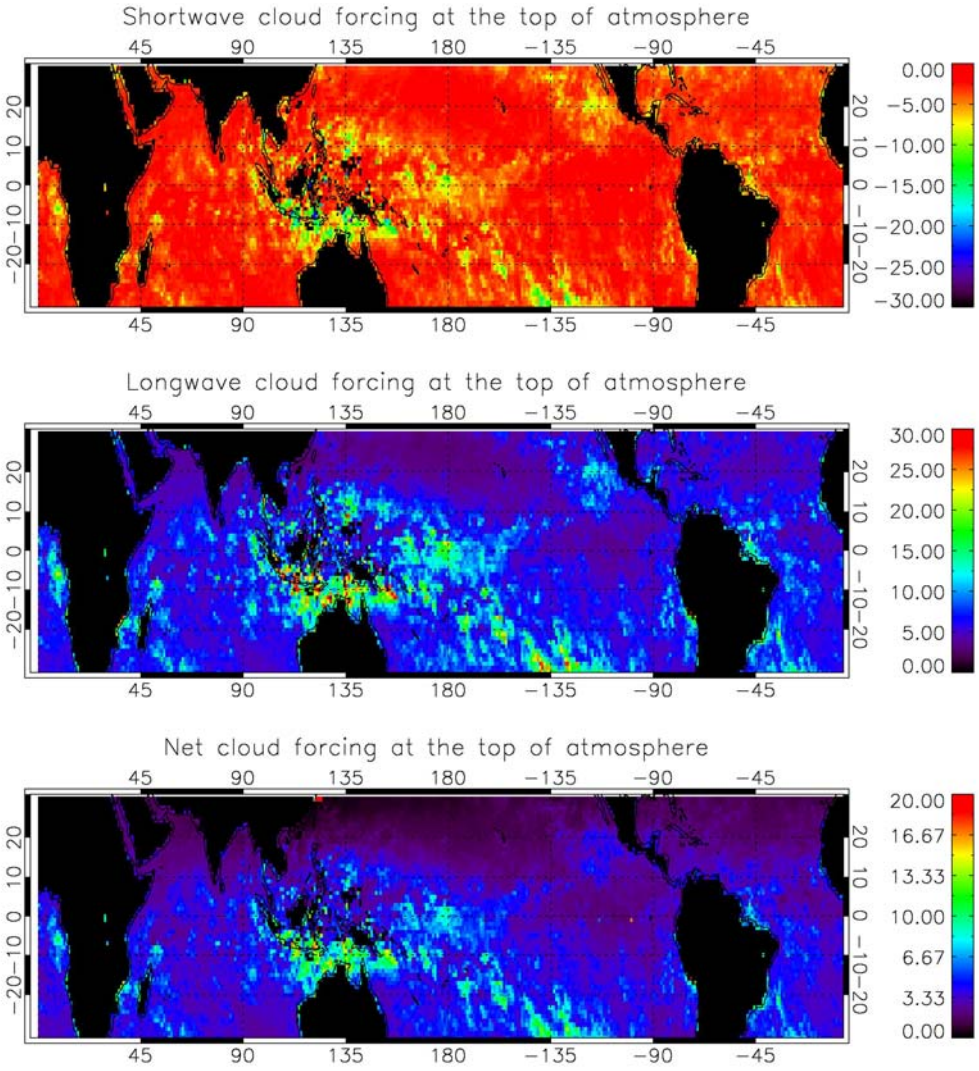

(a)

Figure 3.17 Spatial distribution of cloud radiative forcing (shortwave, longwave, and net forcing from top to bottom panel). (a) At the top of atmosphere for December 2005.

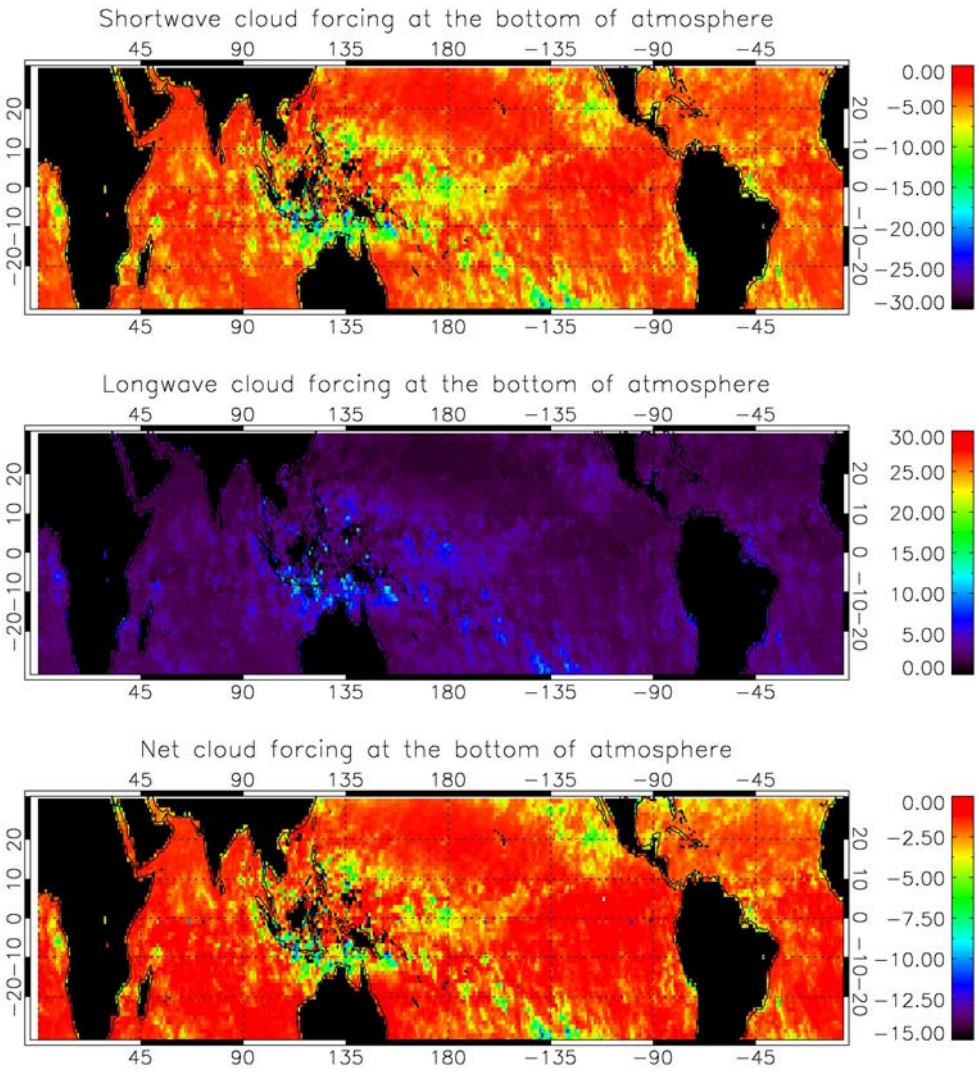

(b)

Figure 3.17 Continued (b) At the bottom of atmosphere for December 2005.

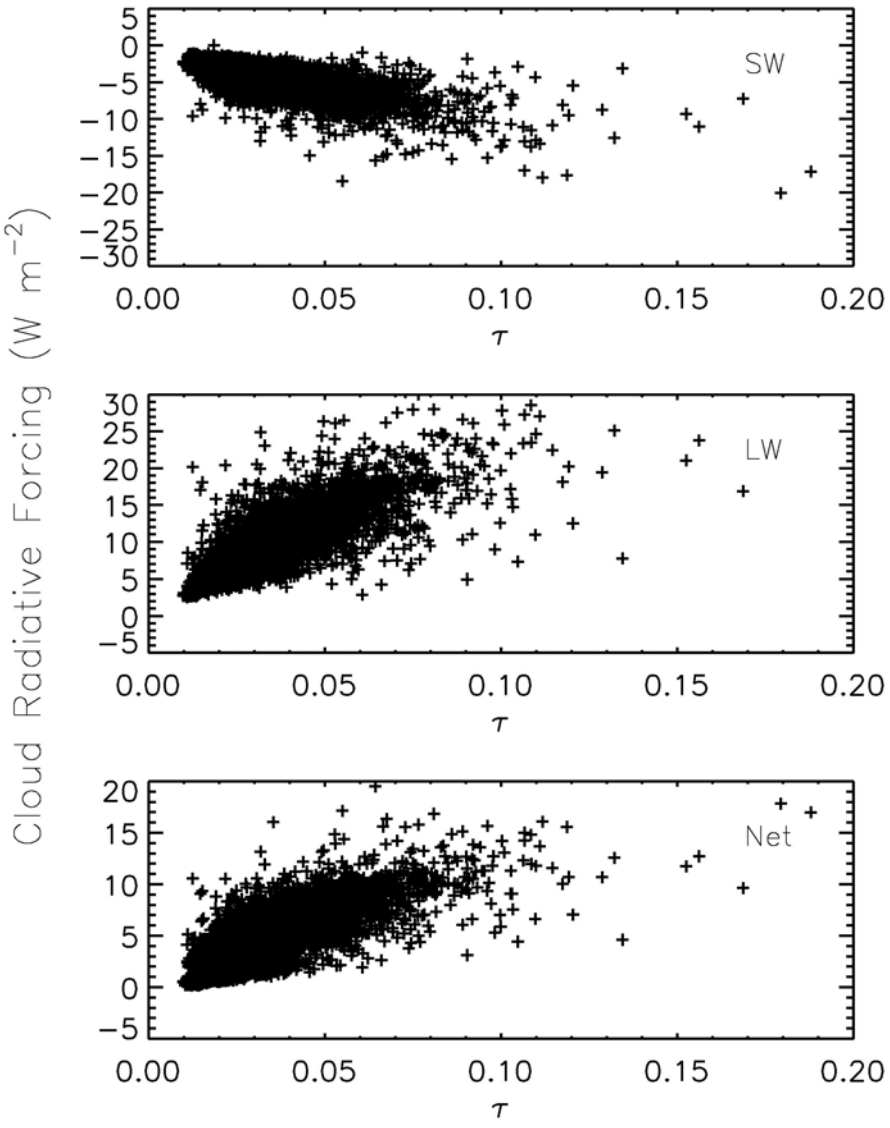

(a)

Figure 3.18 Relationship between optical depth and cloud radiative forcing (shortwave, longwave, and net cloud radiative forcing from top to bottom panel). (a) At the top of atmosphere.

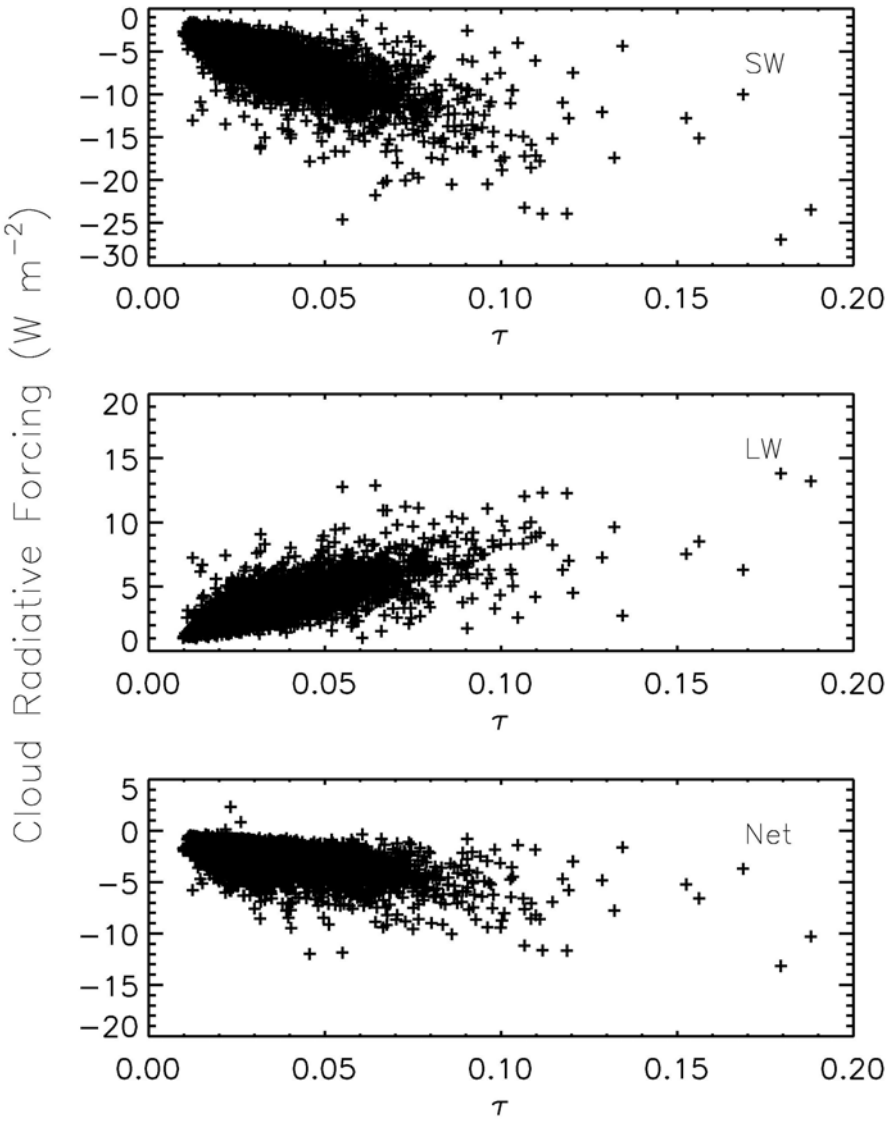

(b)

Figure 3.18 Continued (b) At the bottom of atmosphere.

atmosphere, there is a negative forcing for shortwave, positive for longwave and negative for net. Shortwave negative effect dominates at the bottom of atmosphere.

Figure 3.19 shows the relationship between optical depth and radiative forcing with respect to the solar zenith angle at the top and bottom of atmosphere. For shortwave, the negative forcing increases in magnitude with the increasing solar zenith angle if the optical depth is the same. For longwave, the forcing does not depend on the solar zenith angle by nature. As a result, the net positive forcing decreases with an increasing solar zenith angle at the top of atmosphere and the net negative forcing increases at the bottom of atmosphere.

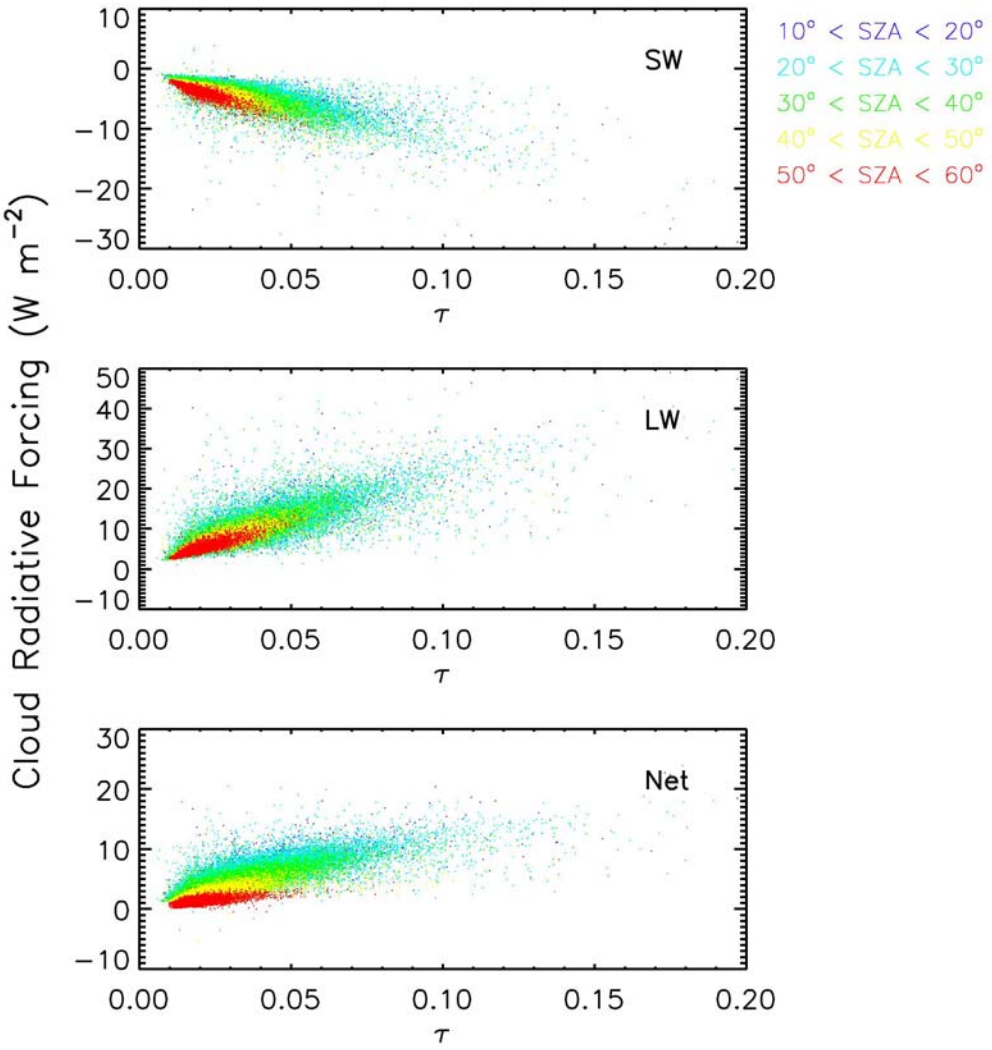

(a)

Figure 3.19 Cloud radiative forcing as a function of optical depth and solar zenith angle (shortwave, longwave, and net cloud radiative forcing from top to bottom panel). (a) At the top of atmosphere.

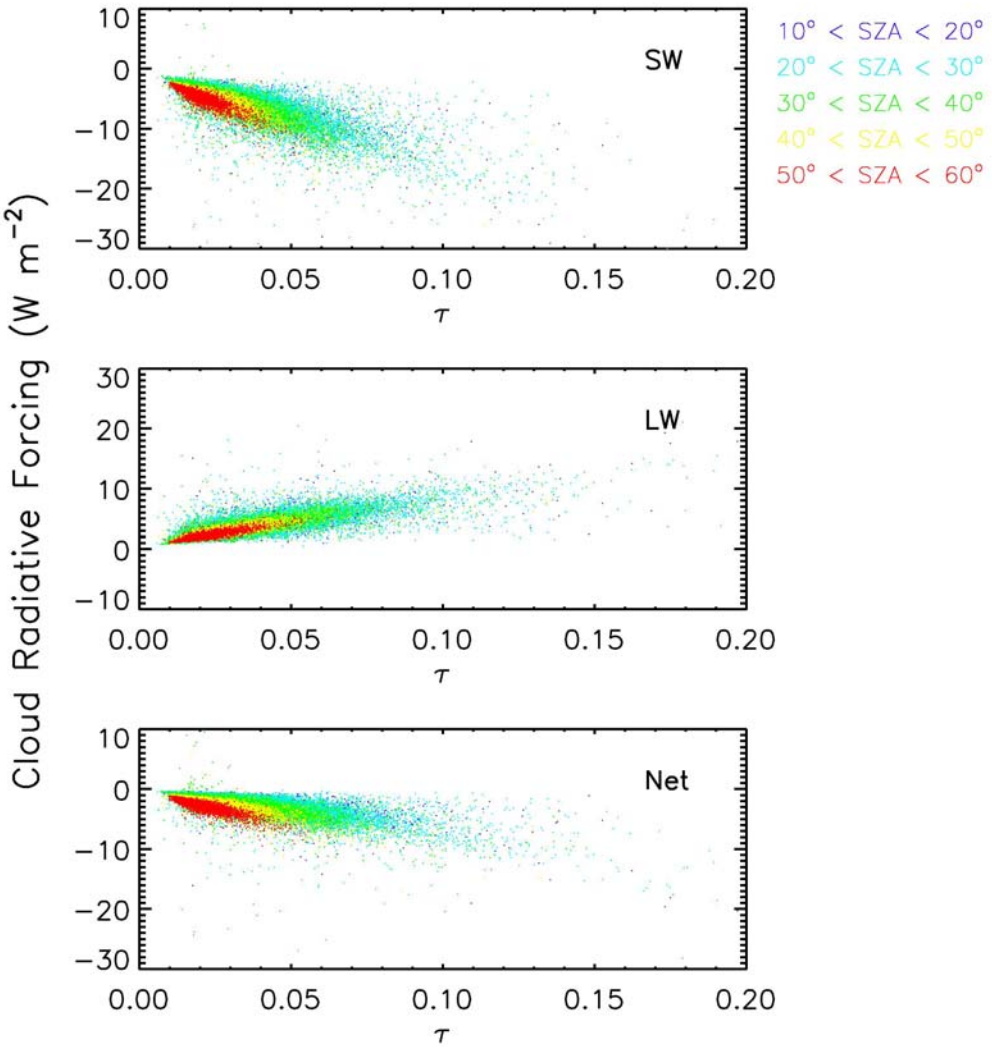

(b)

Figure 3.19 Continued (b) At the bottom of atmosphere.

CHAPTER IV

COMPARISON OF CERES CLEAR-SKY OLR AND MODEL-CALCULATED OLR FROM AIRS ATMOSPHERIC PROFILES OVER THE TROPICS AND DEPENDENCE OF OLR AND GREEENHOUSE EFFECT ON SURFACE TEMPERATURE AND WATER VAPOR

4.1 Background

The outgoing longwave radiation (OLR) is one of important components in the Earth's radiation budget. It has been measured and watched systemically for decades by Earth Radiation Budget (ERB) missions. These satellite measurements provide useful climatological radiation data which help to monitor and understand the physics and variability of Earth's radiation budget.

There have been many studies on the clear-sky OLR using satellite and atmospheric profile data. One approach is to investigate the difference between satellite measurement and simulated clear-sky OLR and to explain the cause of the difference. If a systematic large error exists between them, it would lead to misunderstanding Earth's radiation budget, climate physics, and the radiative effect of clouds. But those studies which compare measured OLR with a simulated one produced somewhat different results. Inamdar and Ramanathan [1994] showed that no significant difference (0.5 Wm^{-2}) exists between ERBE clear-sky OLR and calculated OLR using ship radiosonde data as an input for the radiative transfer model while their RMS of 9 Wm^{-2} is relatively large. Wong et al. [2000] compared CERES ERBE-like clear-sky OLR with a model as a

postlaunch validation of TRMM CERES using NOAA sea surface temperature and NCEP three-dimensional atmospheric dataset. The model is a good simulation of the spatial features of clear-sky OLR with a -4 Wm^{-2} difference. Whereas Ho et al. [1998] showed a positive model bias of 1.9 – 2.3 Wm^{-2} when compared with ERBE averaged over time (1985 - 1989) and space (60°S - 60°N). One reason for opposite signs in difference between measurement and simulation is that each study uses a different radiative transfer model and the treatment of absorption gases (H_2O, CO_2, O_3, CH_4, and CFCs, etc.) is different in each model [Ho et al., 1998]. Also, each different data set of atmospheric profiles used in the model simulation might contribute to the various results causing one study to differ from another.

Another approach is to examine the physical relationship between OLR, surface temperature, and water vapor including the greenhouse effect. Inamdar and Ramanathan [1994] studied the interactions between deep convection, vertical distributions of water vapor, and the greenhouse effect over tropical oceans. They showed that the greenhouse effect is stronger in convective regions due to the absorption of longwave radiation by excessive water vapor and a super greenhouse effect is caused by the rapid increase of lower level water vapor with increasing sea surface temperature (SST). Raval et al. [1994] compared four years of ERBE data and model simulation using atmospheric profile data obtained from rawindsonde and ship data to examine the dependence of OLR on surface temperature and water vapor. It is shown that OLR is mainly dependent on surface temperature (T_s) in low temperature (T_s < 10 °C) and on both surface temperature and relative humidity in tropical (T_s > 25 °C). Allan et al. [1998] showed

similar results when they compared long-term clear-sky ERBE OLR with a simulation using global ECMWF reanalyses data. It is noted that surface temperature is a more dominant factor on OLR in high latitudes and relative humidity has a larger effect on OLR in low latitudes. Also, it is shown that clear-sky OLR variation is most dependent on mid-troposphere (400 to 700 hPa) humidity changes.

This study simulates the clear-sky outgoing longwave radiation and compares it with CERES measurement to investigate the differences between them. One of the most unique features of this study is to use atmospheric profiles from AIRS which is onboard the same satellite, Aqua, with CERES. Thus, the OLR and atmospheric profiles are observed at nearly the same time and space. Also, this study will examine the effect of water vapor and temperature on clear-sky OLR including the super greenhouse effect which decouples surface temperature and OLR by reducing OLR with increasing surface temperatures at high sea surface temperatures. CERES OLR and atmospheric profile data from Aqua used in this study will be reviewed in section 4.2 and Chou's radiative transfer model will be explained in section 4.3. In section 4.4, the difference between CERES OLR and simulated OLR will be examined. The effect of surface temperature and water vapor on OLR and the super greenhouse effect are also presented in section 4.

4.2 Data

CERES provides the global cloud, aerosol and radiation data for EOS to examine the role of cloud/radiation feedback in the Earth's climate system [Loeb et al., 2005]. It is a broadband scanning radiometer in three channels: a shortwave channel (0.3-5.0μm)

to measure reflected solar radiation, an infrared window channel (8-12μm) to measure Earth's thermal emission and a total channel (0.3-200μm). The broadband longwave radiation is calculated as the total minus shortwave. CERES provides surface, atmosphere and top-of-atmosphere (TOA) radiative flux estimates globally at a 20-km spatial resolution at nadir [Wielicki et al., 1996]. CERES onboard Aqua has two scanning modes, one scanning in a fixed azimuth plane for time-space averaging and the other scanning in a rotating azimuth plane for improved angular sampling [Loeb et al., 2005].

The OLR data analyzed in this study are obtained from CERES single scanner footprint (SSF) TOA fluxes. CERES data is compared with MODIS cloud products and those data which are defined as confident clear are only selected. Then, the AIRS profiles which are closest within 20 km of center of CERES pixels are selected for each CERES fluxes. Only nighttime data around 1:30 am local time are used for March and September 2005.

4.3 Model

Chou's radiative transfer model [2001] is used for the calculation of clear-sky outgoing longwave radiation. In this model, the infra spectrum is divided into 9 bands and one subband from 0 to 3000 cm-1. The parameterization includes the absorption due to major gases (water vapor, CO2, and O3) and most of the minor trace gases (N2O, CH4, and CFC's) as well as clouds and aerosols. The gaseous transmission function is computed using either the k-distribution method or the table look-up method. The

accuracy of the model is within 1% of the high spectral-resolution line-by-line calculation. In this calculation, band 9 (1900~3000 cm-1) is excluded to match the CERES TOA flux band (50~2000 cm-1). The AIRS atmospheric profile, which is collocated with CERES measurement, includes temperature profile, water vapor profile, ozone profile, and surface temperature. 27-layer temperature profile, 10-layer water vapor profile, and 9-layer ozone profile are interpolated into a 100-layer atmospheric profile. The standard tropical atmosphere profiles are used above the maximum level of AIRS measurement. The advantage of using both CERES and AIRS data is that both system are onboard the same satellite, Aqua, and provide the same time and same area coverage measurement throughout the operations.

4.4 Results

4.4.1 The comparison of OLR between CERES and model simulation

The comparison between calculated OLR and CERES OLR for September 2005 is shown in Figure 4.1. The total number of points considered is 137,425. The mean value of CERES OLR is 290.0 Wm^{-2} and that of the calculated OLR is 294.2 Wm^{-2}. The calculated OLR is larger than CERES OLR at almost all points. The mean difference is 4.2 Wm^{-2} and the standard deviation in difference is 2.1 Wm^{-2}. Although there are discrepancies between CERES and simulated OLR it shows consistently a good relationship between them with small constant variations. The solid line is the line of slope 1 and the broken line is a linearly fitted line. The differences increase with increasing OLR - the two values match well in the humid region and the differences are

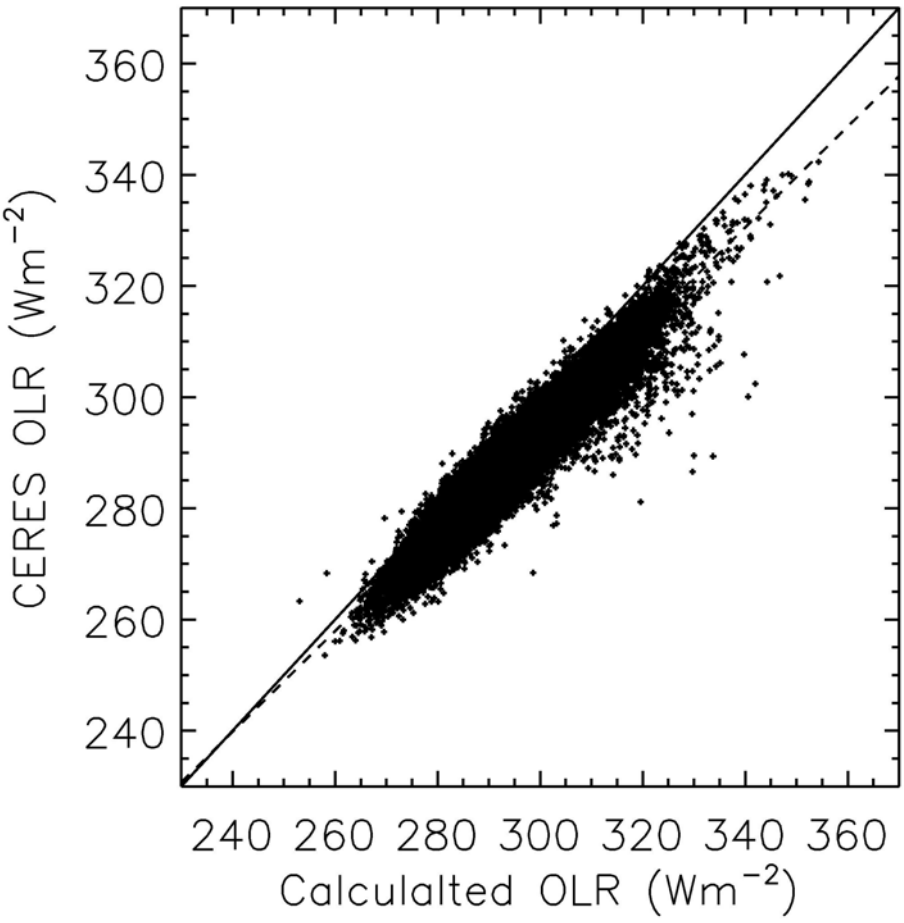

Figure 4.1 The comparison between CERES OLR and calculated OLR for September 2005.

larger in the less moist region. Observed correlations between OLR, surface temperature and water vapor are presented in detail in the following analyses.

To examine the spatial features of OLR and difference, a spatial distribution of CERES OLR, calculated OLR, and the difference between them were plotted over tropical oceans within latitudes 30°N and 30°S for September 2005 in Figure 4.2. The maximum OLR existed over the southeastern Pacific and the minimum over western Pacific Ocean. The model calculated accurately the spatial distribution of CERES OLR. The calculated OLR minimum appears over the western Pacific and the maximum over the southeastern Pacific as CERES OLR does. Differences are small in the northern hemisphere where OLR is low, whereas differences are large in southern Indian Ocean, southwestern Pacific, and southeast Pacific where OLR is high.

Figure 4.3 is the same as Figure 4.2 except for March 2005. Except for the fact that the maximum or minimum migrates southward in response to the migration of ITCZ and the sun, the general features are similar to those of September 2005. OLR minimum exists in the southwestern Pacific around Indonesia and the maximum exists along the zonal band between 10°N and 20°N and the southeastern Pacific. Calculated OLR produces spatial distributions similar to those of CERES OLR with larger values. Again, the difference between CERES and the calculated OLR is largest in the Northern hemisphere where OLR is large.

Figure 4.4 shows the zonal average of CERES OLR, model OLR and the difference between them. Each OLR and difference is averaged in every 1° latitude from 30°S to 30°N. It can be seen again that the simulation of OLR describes accurately the

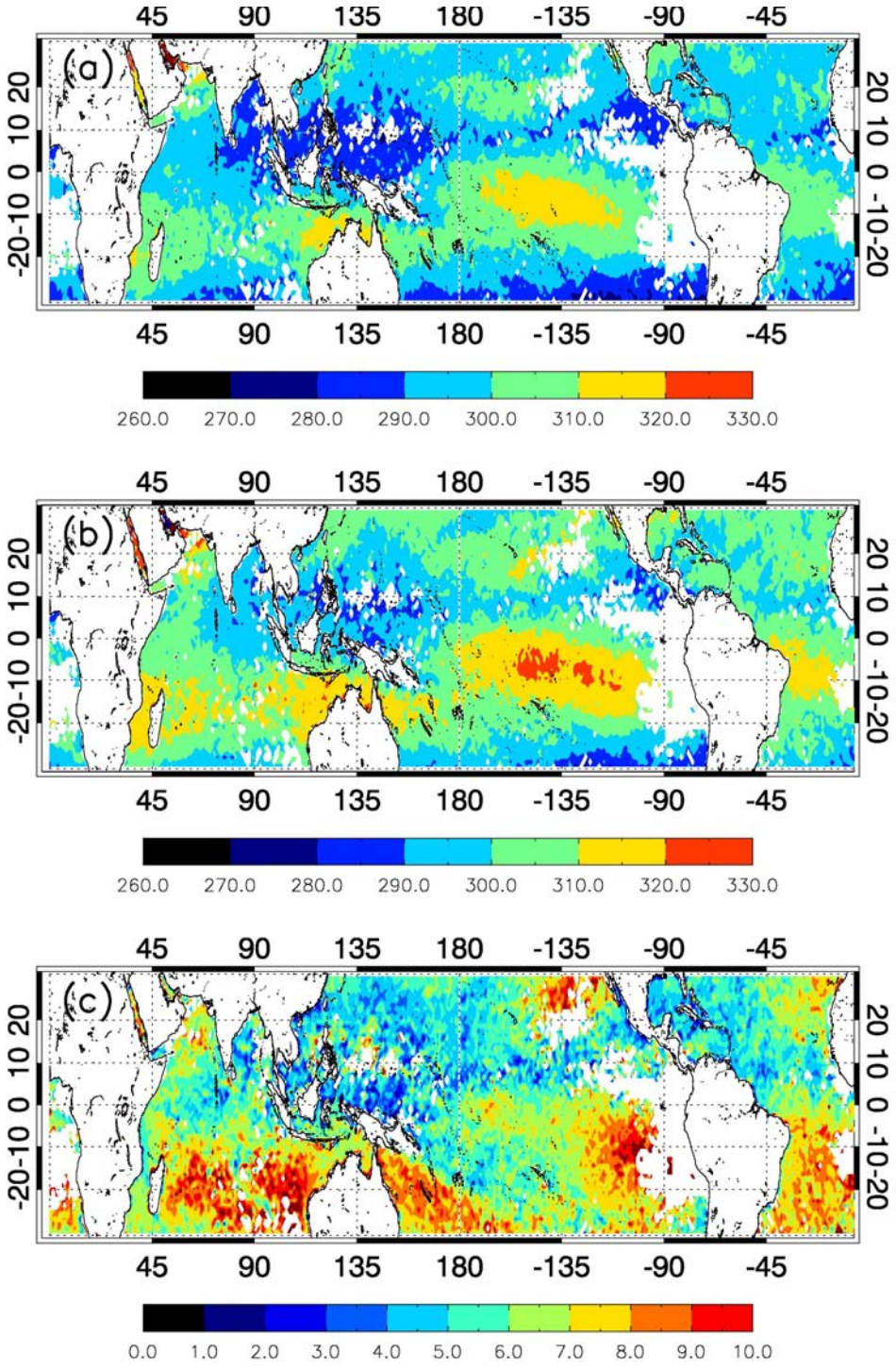

Figure 4.2 The spatial distribution of (a) CERES OLR, (b) calculated OLR, and (c) the difference between them for September 2005. All units are Wm^{-2}.

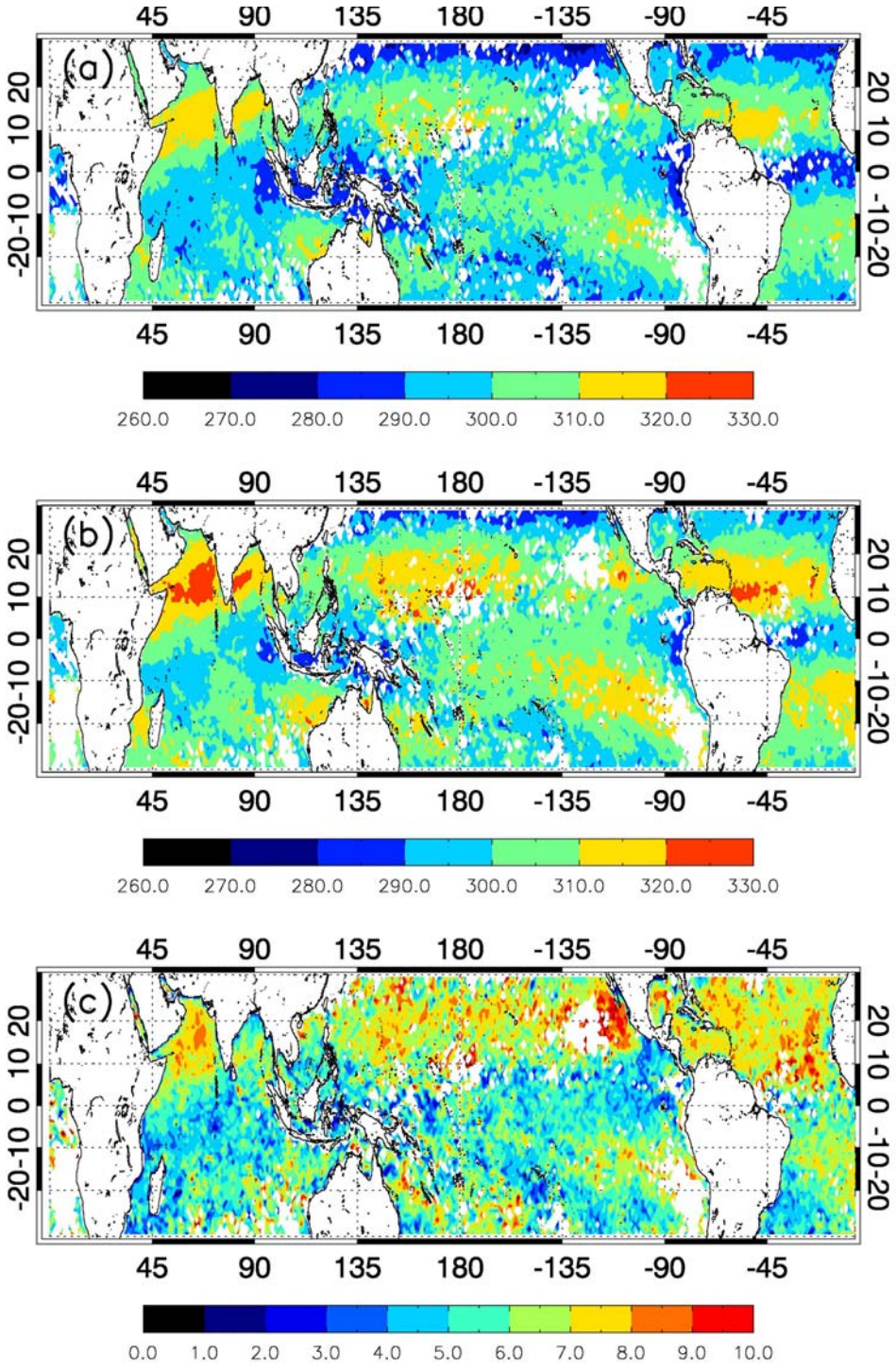

Figure 4.3 The spatial distribution of (a) CERES OLR, (b) calculated OLR, and (c) the difference between them for March 2005. All units are Wm^{-2}.

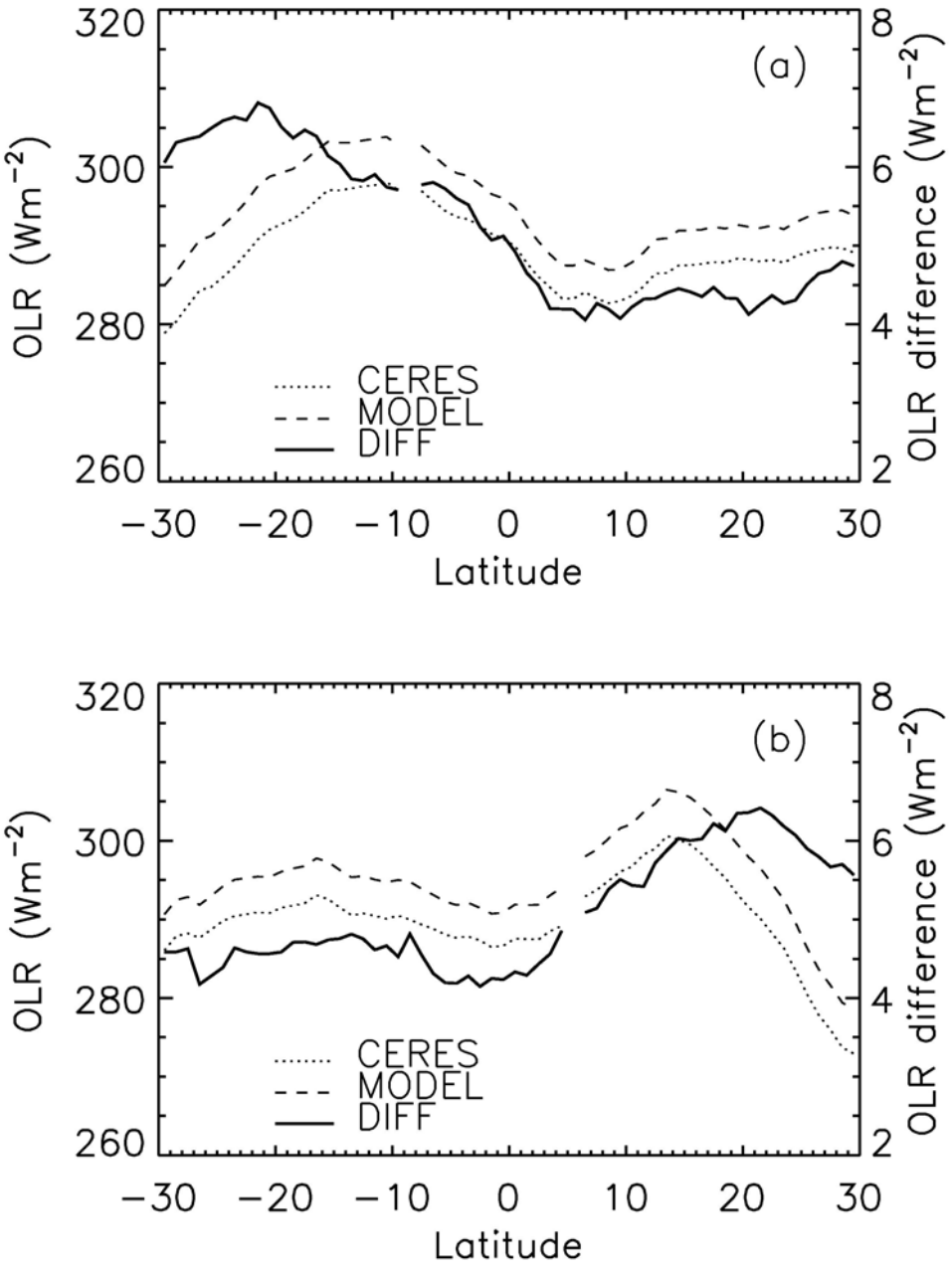

Figure 4.4 The latitudinal variation of CERES OLR, calculated OLR, and difference between them for (a) September 2005 and (b) March 2005.

variations of OLR with latitude. In September 2005, OLR peaks at 10°S, decreases up to 5°N, and shows relatively constant values between 5°N and 30°N. The variations of OLR difference with latitude between CERES and calculation resembles remarkably that of OLR. The variations are almost the same from 30°N to 10°S but difference continues to increase up to 20°S. In March 2005, OLR is relatively constant from 30°S to 5°N, then increases up to 15°N, and decreases at higher latitudes. The latitudinal variations of difference are similar to those of OLR from 30°S to 15°N but increase continuously and peak at 25°N.

Figure 4.5 shows the variations of OLR differences between CERES and model calculation with surface temperature and water vapor. The OLR difference is averaged over every 0.5 K of surface temperature and 1 g/kg of water vapor. OLR difference has a constant value of 6.5 Wm^{-2} up to the surface temperature of 297 K and decreases with increasing temperature between 297 K and 303 K of surface temperature. The difference increases with increasing surface temperature where surface temperature is larger than 303 K. The OLR difference shows a minimum at 303 K of surface temperature. It will be shown in Figure 4.9 that water vapor reaches maximum and OLR has local minimum at 303 K. OLR difference decreases constantly with increasing water vapor.

4.4.2 The relationship between OLR, surface temperature, and water vapor

Figure 4.6 shows the spatial distributions of CERES OLR, sea surface temperature (SST), and the column integrated water vapor for September 2005. SST

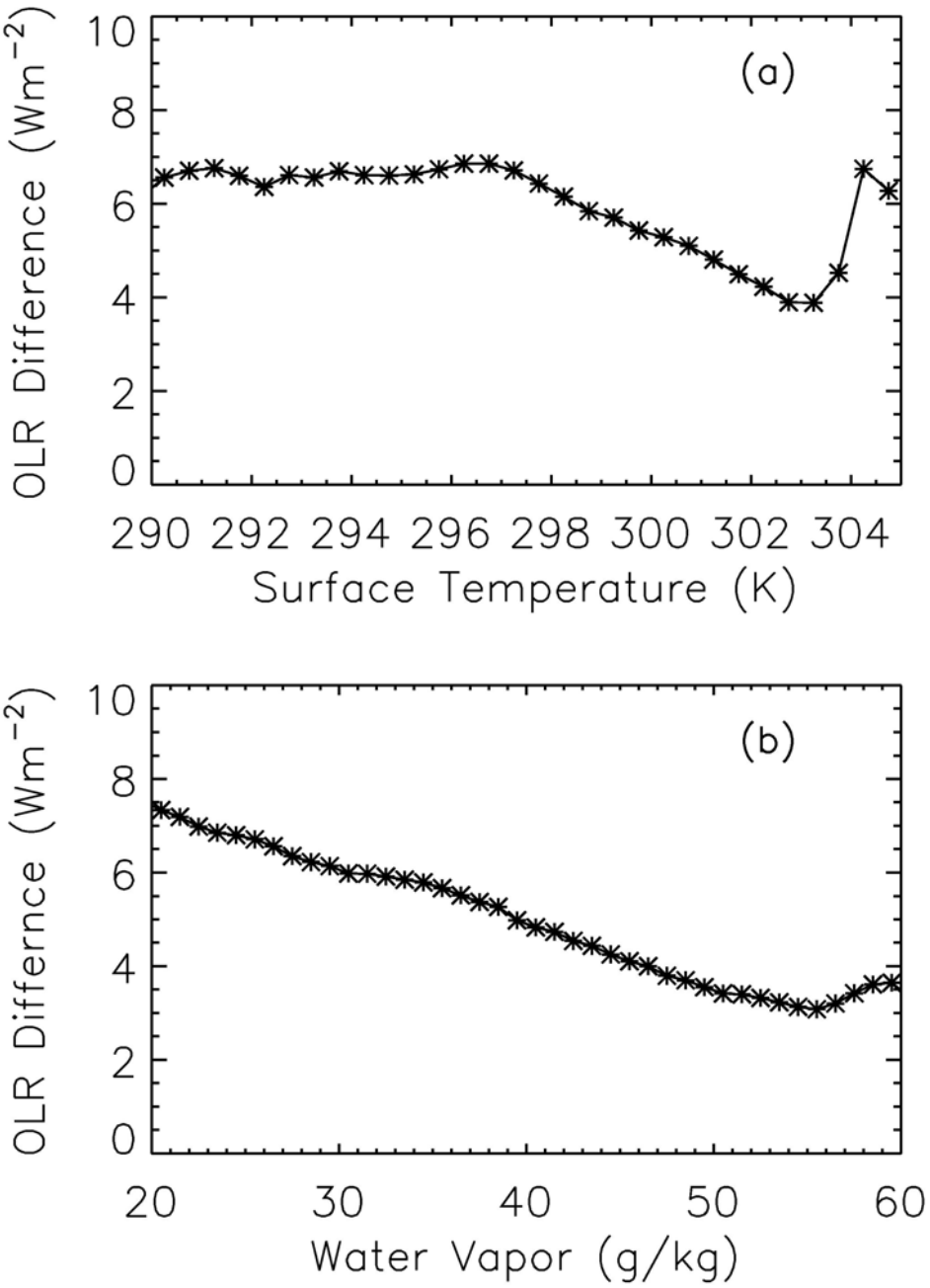

Figure 4.5 The OLR difference between calculated OLR and CERES OLR with a function of (a) surface temperature and (b) column integrated water vapor mixing ratio.

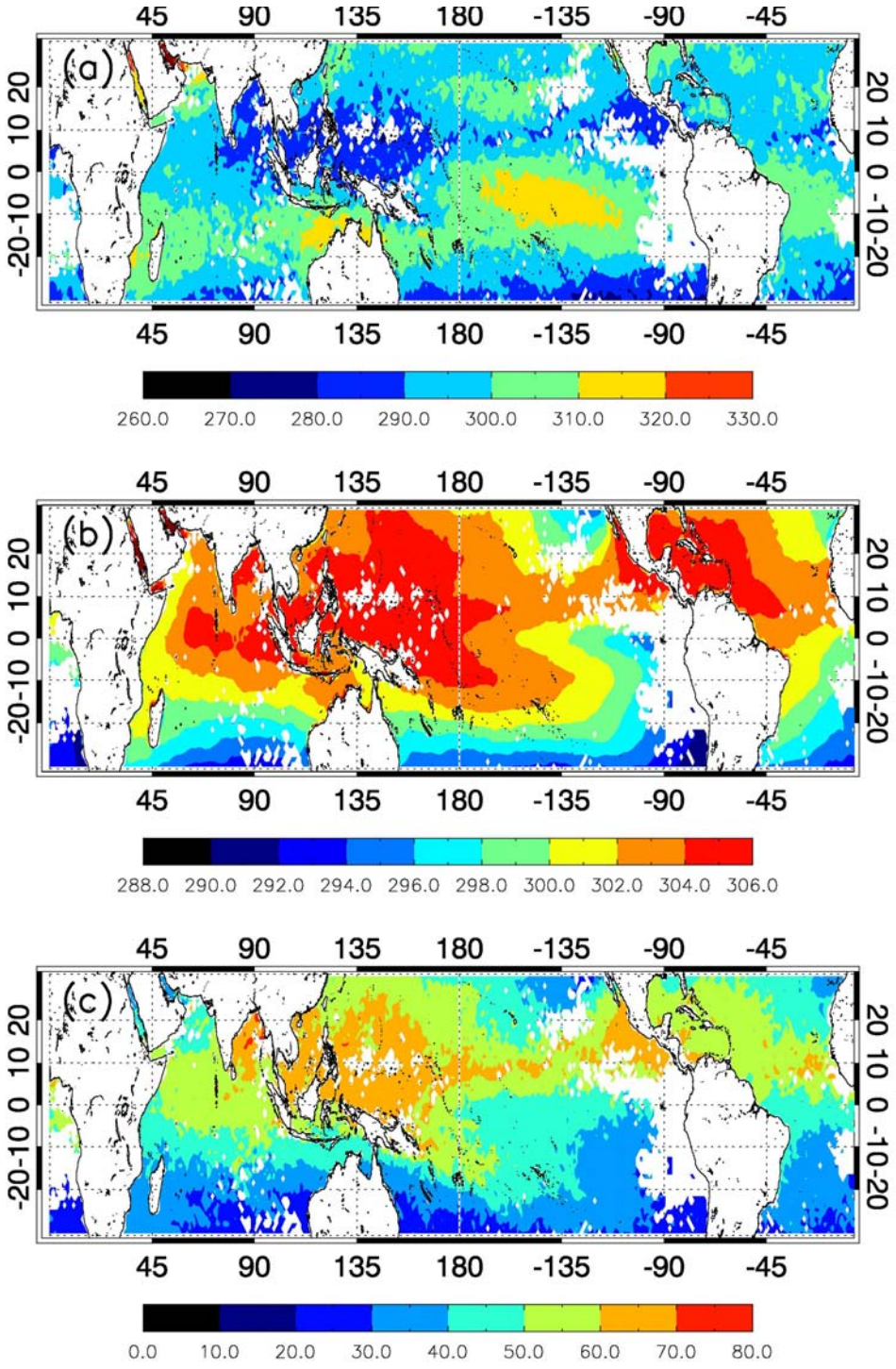

Figure 4.6 The spatial distribution of (a) CERES OLR (Wm^{-2}), (b) surface temperature (K), and (c) column integrated water vapor mixing ratio (g/kg) for September 2005.

maximum locates over the western Pacific warm pool and the Gulf of Mexico and SST decreases toward high latitudes. Water vapor distributions show patterns similar to that of SST distributions. Water vapor maximum locates over the western Pacific and Central America and water vapor decreases toward high latitudes. OLR increases with increasing SST and water vapor at high latitudes while decreases with increasing SST and water vapor at low latitudes. These features will be discussed in detail in a later section.

Figure 4.7 has the same spatial distribution as Figure 4.6 except for March 2005. The high SST is centered at the southwestern Pacific and the southern Indian Ocean and SST decreases gradually from this center toward high latitudes. Column integrated water vapor shows a spatial distribution similar to that of SST. The high water vapor locates at the southwestern Pacific around Indonesia, the southern Indian Ocean, and the Atlantic Ocean between South America and Africa and decreases gradually toward high latitudes. Again, at high latitudes, the OLR increases with increasing SST and water vapor while at low latitudes, the OLR decreases with increasing SST and water vapor.

Figure 4.8 shows the variation of CERES OLR and model OLR with surface temperature and total column water vapor for September 2005. OLR is averaged over every 1 K of surface temperature and 1 g/kg of water vapor. OLR increases with increasing surface temperature up to 299 K, decreases with increasing surface temperature between 299 K and 303 K, and increases again where the surface temperature is larger than 303 K. OLR increases with increasing water vapor up to 30 g/kg and decreases continuously with increasing water vapor. If surface temperature is

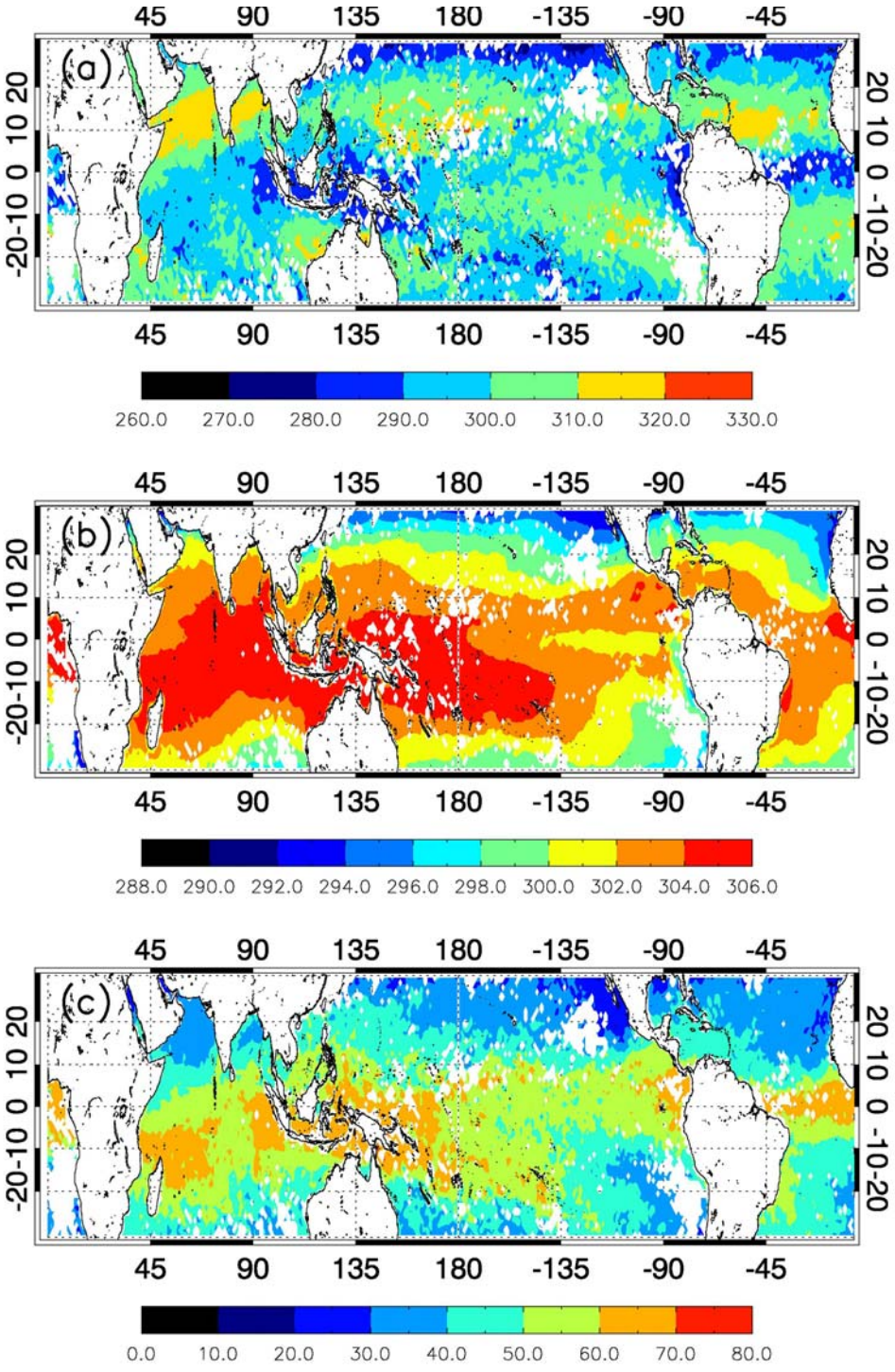

Figure 4.7 The spatial distribution of (a) CERES OLR (Wm^{-2}), (b) surface temperature (K), and (c) column integrated water vapor mixing ratio (g/kg) for March 2005.

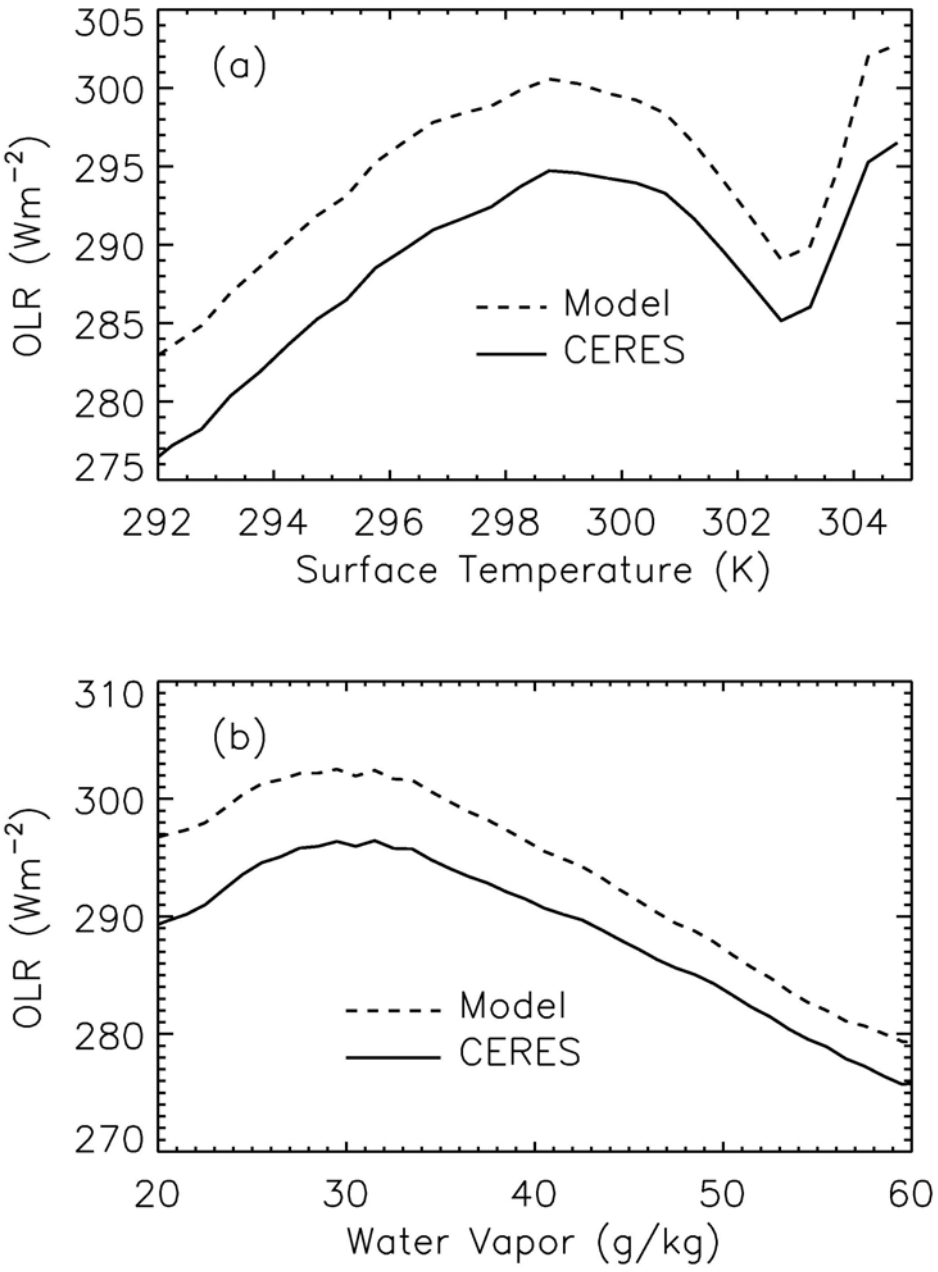

Figure 4.8 The variation of OLR with a function of (a) surface temperature and (b) column integrated water vapor mixing ratio for September 2005.

lower than 300 K, the dominant factor contributing to OLR is the surface temperature. The decrease of OLR with increasing surface temperature between 300 K and 303 K is due to the strong absorption of surface emitted longwave radiation by increased water vapor. In other words, the increase of longwave radiation absorption by water vapor exceeds the increase of longwave radiation emission from the surface with increasing surface temperature. This is referred to as the super greenhouse effect by Ramanathan and Collins [1991].

To examine the relationship between OLR, surface temperature, and water vapor, the variations of column integrated water vapor and OLR with surface temperature are plotted together for (a) September 2005 and (b) for March 2005 in Figure 4.9. Both OLR and water vapor increase with increasing surface temperature up to 299 K (301K) for September (March) 2005. But OLR decreases if the surface temperature is larger than 299 K while water vapor increases continuously up to 303 K of surface temperature. If surface temperature is larger than 303 K, OLR increases again while water vapor decreases. It is shown again that surface temperature is the dominant factor in OLR at low surface temperatures while water vapor dominates at high surface temperatures.

4.4.3 The effect of surface temperature, lapse rate, and water vapor on OLR and the greenhouse effect

Figure 4.10 shows the number distribution of points with surface temperature. The distribution peaks at high surface temperatures and more than 50% of data have surface temperatures larger than the convective threshold of 298 K.

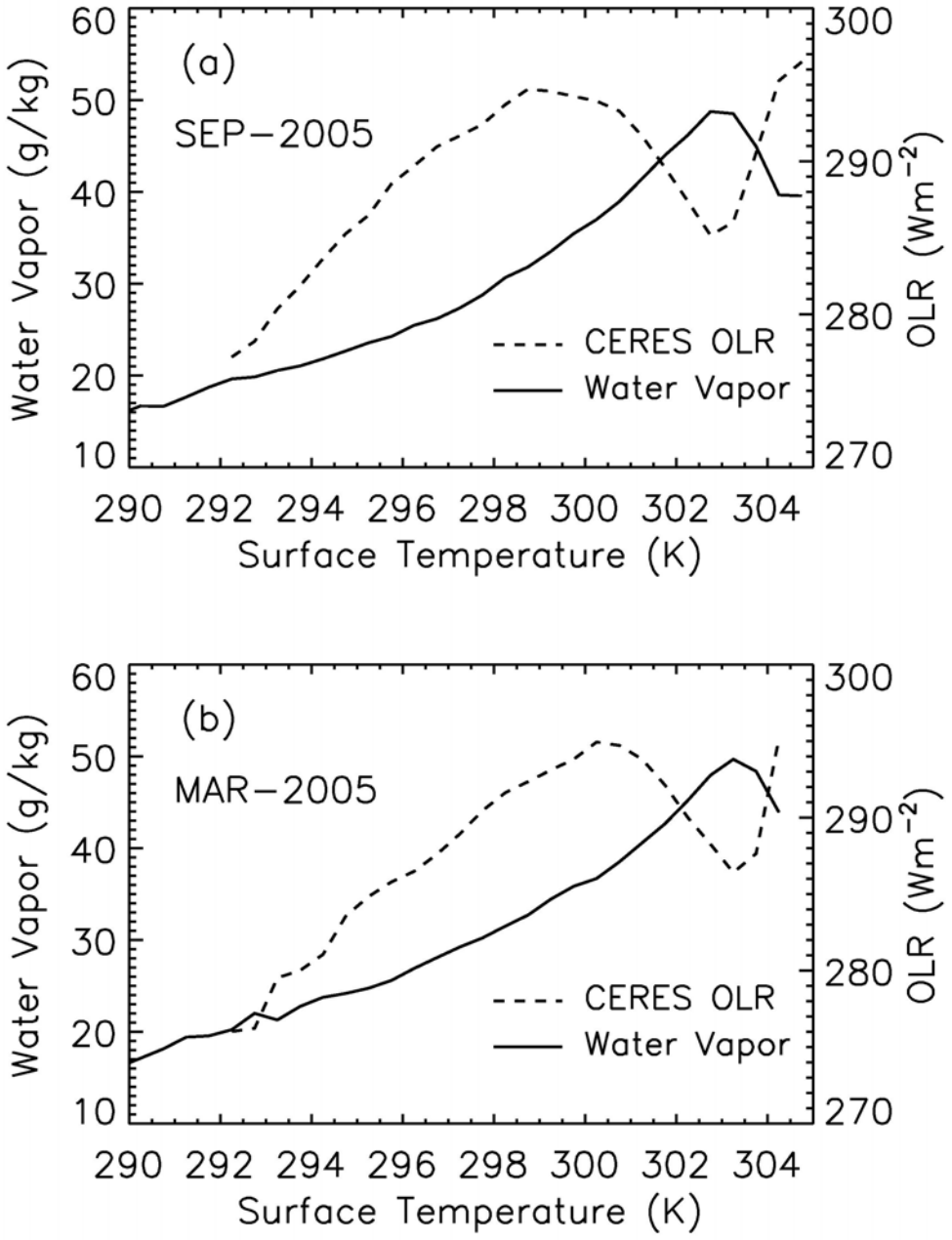

Figure 4.9 The variation of column integrated water vapor mixing ratio and CERES OLR with a function of surface temperature for (a) September 2005 and (b) March 2005.

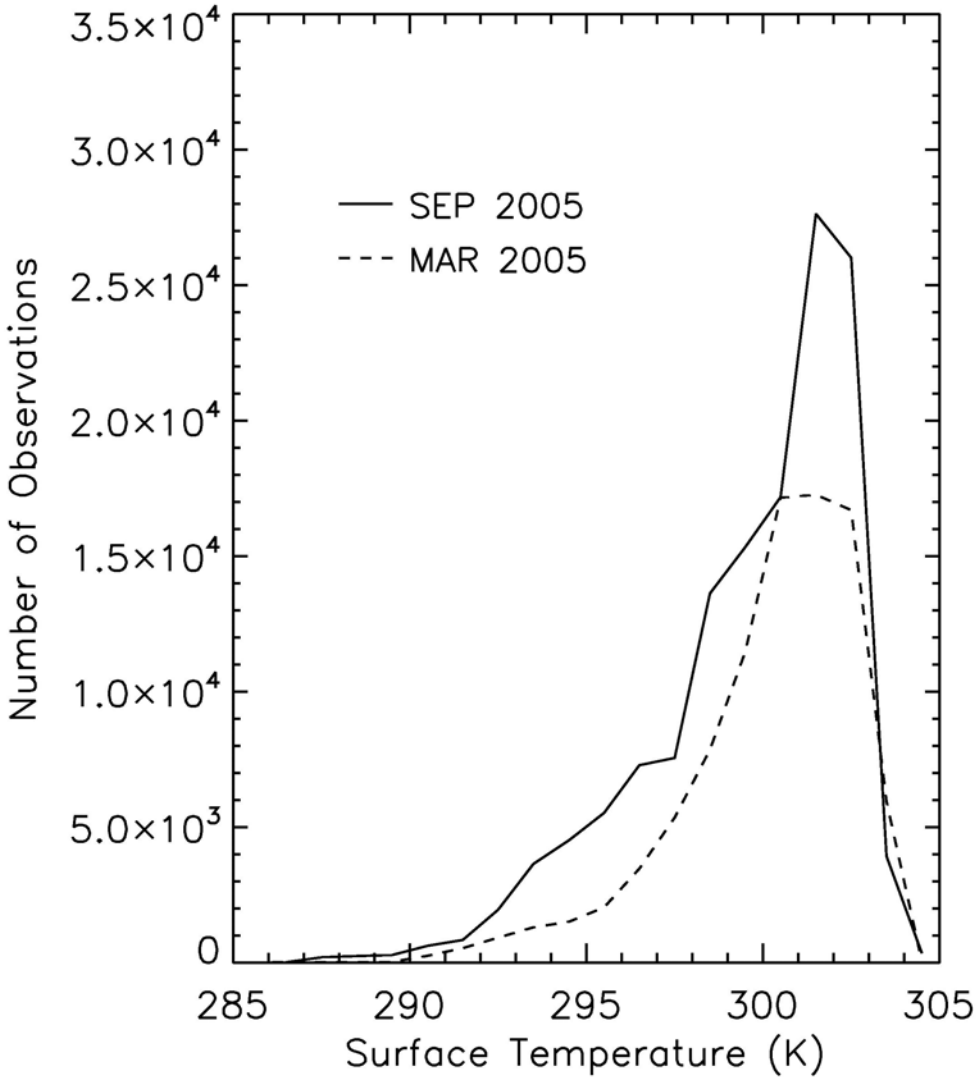

Figure 4.10 The number of observations with a surface temperature.

The variations of atmospheric temperature with surface temperatures at 850, 600, 400, and 200 hPa are shown in Figure 4.11. The atmospheric temperature increases with increasing surface temperatures up to 298 K in the low to mid troposphere (850 hPa ~ 400 hPa). In the lower troposphere (850hPa), the atmospheric temperature increases continuously with the increasing surface temperature where surface temperature is larger than 298K. However, the atmospheric temperature does not change with increasing surface temperature in the middle troposphere (600 hPa and 400 hPa) if the surface temperature is larger than 298 K. The upper troposphere (200 hPa) atmospheric temperature does not vary at all with the increasing surface temperature. This means that the temperature increase in the atmosphere corresponding to the increase of surface temperature is confined to the lower troposphere and does not disturb the upper troposphere. This feature is the same as that of Inamdar and Ramanathan [1994].

The variation of water vapor with surface temperature is shown in Figure 4.12. The water vapor increases gradually with increasing surface temperatures up to 298 K, increases sharply up to 303 K, and decreases beyond 303 K of surface temperature throughout the troposphere, which produces a water vapor maximum at around 303 K of surface temperature.

To examine the interaction between flux, the greenhouse effect, atmospheric cooling, and surface temperature, each variable is plotted in Figure 4.13 with a function of temperature. All the results in this figure are obtained from the model simulation. First, in Figure 4.13(a), the upward flux at the surface ($F_s^{\uparrow}$) increases with the increasing

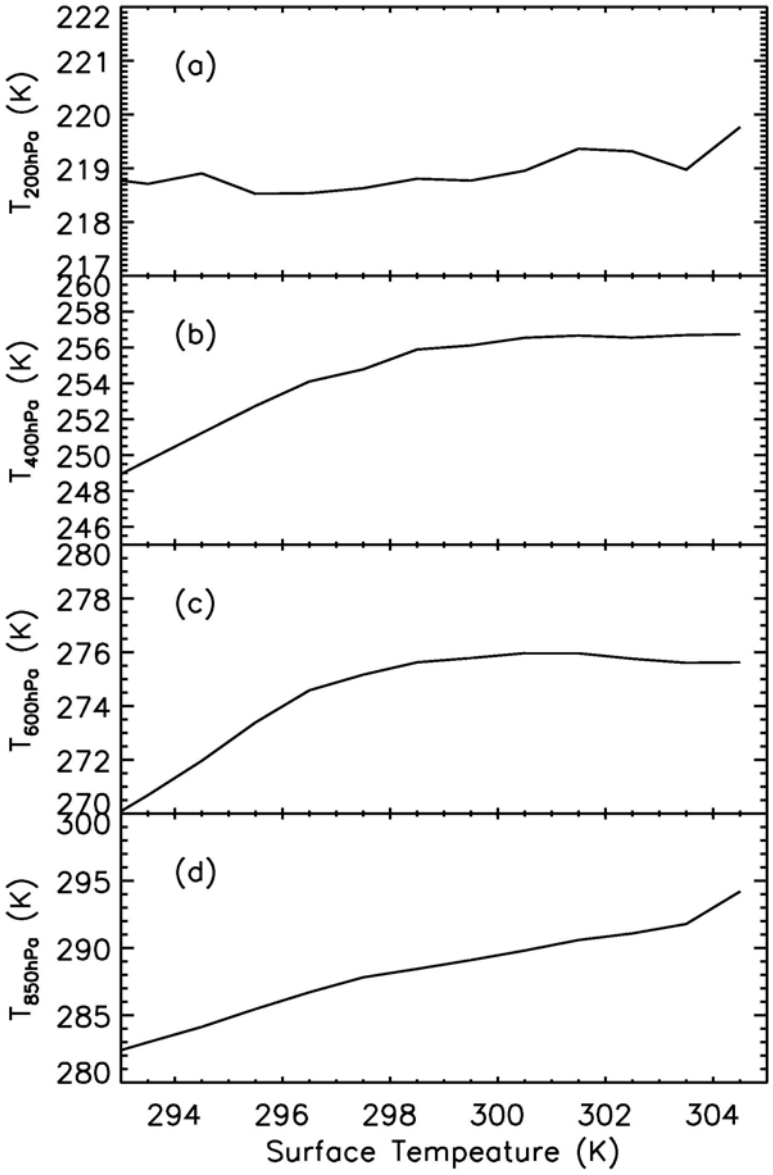

Figure 4.11 The variation of atmospheric temperature at (a) 200 hPa, (b) 400 hPa, (c) 600 hPa, and (d) 850 hPa with a function of surface temperature for September 2005.

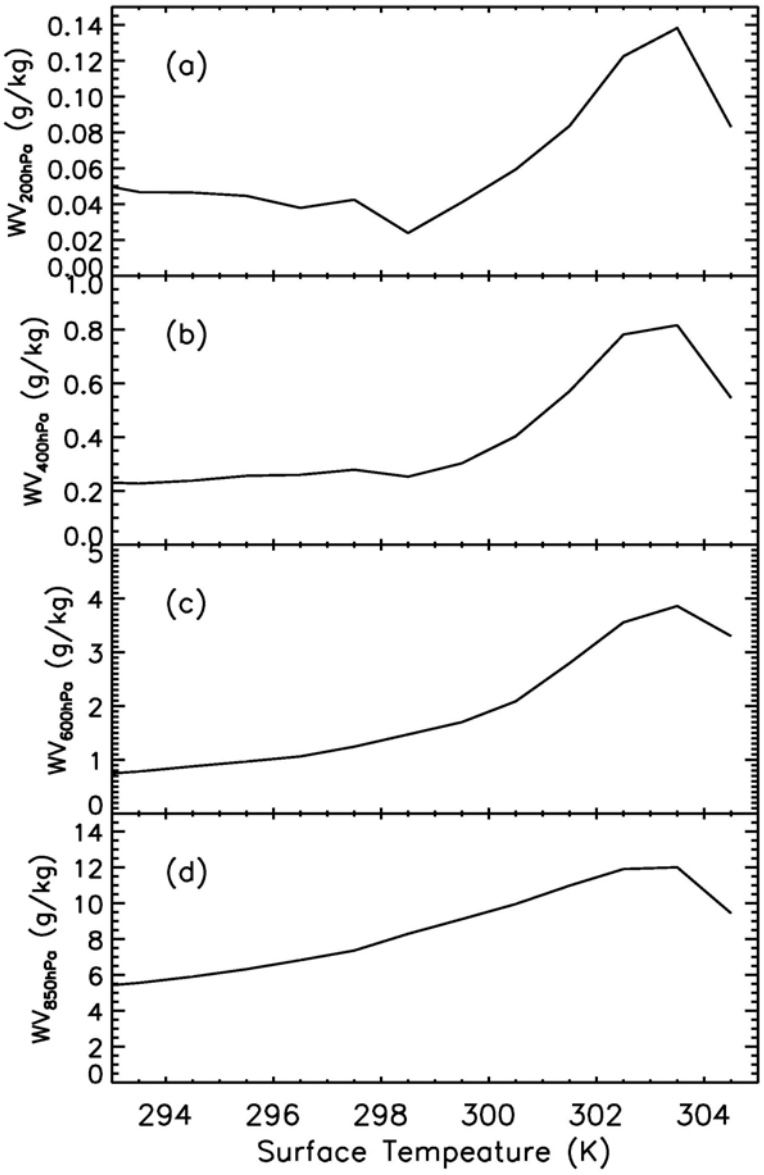

Figure 4.12 The variation of column integrated water vapor mixing ratio at (a) 200 hPa, (b) 400 hPa, (c) 600 hPa, and (d) 850 hPa with a function of surface temperature for September 2005.

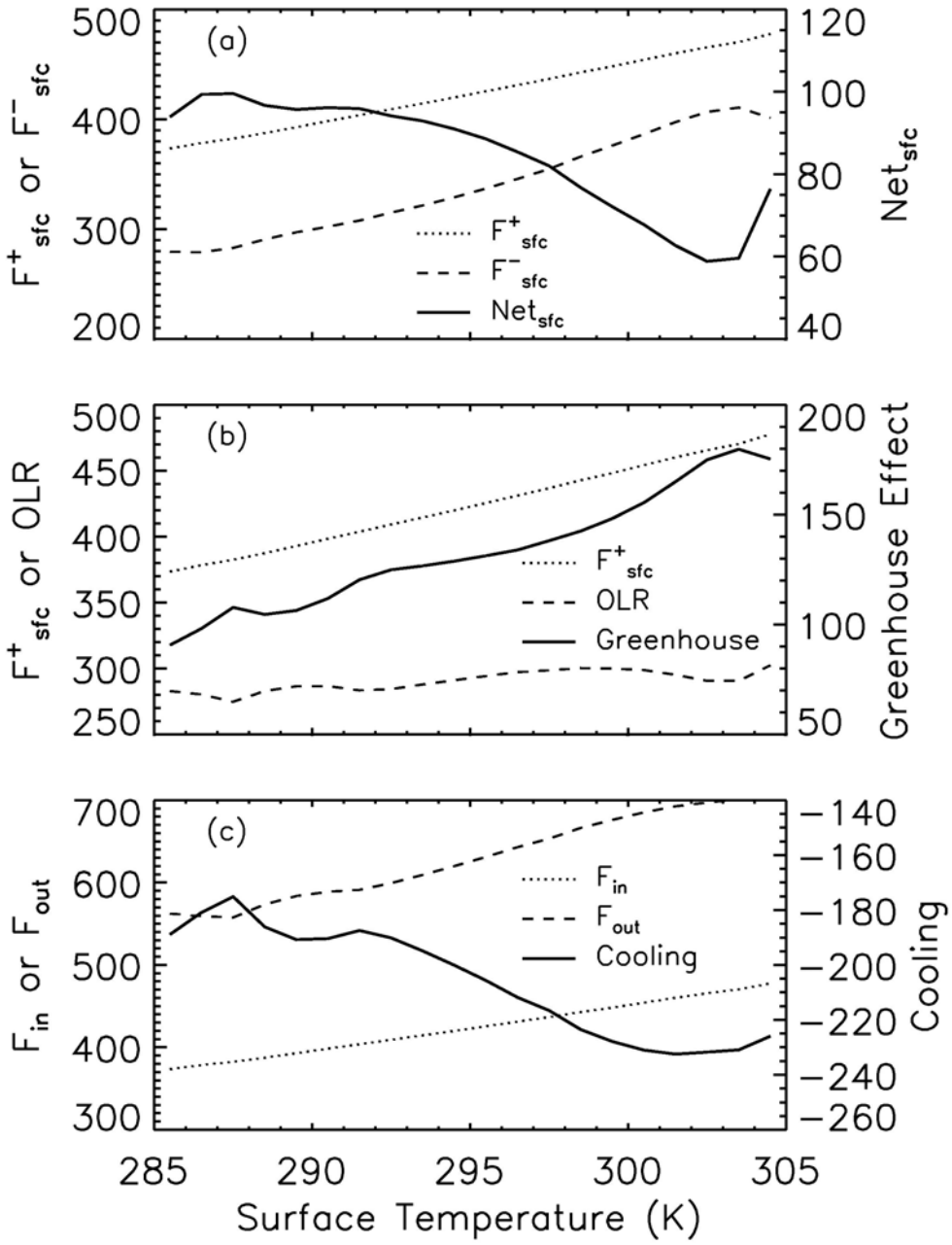

Figure 4.13 The variations of (a) upward flux at the surface, downward flux at the surface, and net flux at the surface, (b) upward flux at the surface, OLR, and greenhouse effect, and (c) flux into the atmosphere, flux out of atmosphere, and atmospheric cooling with a function of surface temperature for September 2005. All units are Wm^{-2}.

surface temperature due to the increased longwave emission from the surface. The downward flux at the surface ($F_s^{\downarrow}$) also increases with increasing surface temperature due to increased water vapor by absorbing longwave radiation from the surface and emitting back to the surface. The net flux at the surface, defined as $F_s^{net} = F_s^{\uparrow} - F_s^{\downarrow}$, decreases with increasing surface temperature because the increase of the downward flux is larger than that of the upward flux. In Figure 4.13(b), the clear-sky greenhouse effect, defined as $G_a = F_s^{\uparrow} - OLR$, increases with increasing surface temperature because the increase of the upward flux at the surface exceeds that of OLR. In Figure 4.13(c), the atmospheric cooling, defined as $C = F_{in} - F_{out} = F_s^{\uparrow} - (F_s^{\downarrow} + OLR)$, decreases with increasing surface temperature. It reaches a minimum of 230 Wm^{-2} at the surface temperature of 302 K.

The atmospheric temperature profile and water vapor profile at three different surface temperatures of 294 K, 300 K, and 303 K are compared in Figure 4.14 for September 2005. All the profiles between surface temperatures of 293 K and 294 K are averaged for 294 K, between 299 K and 300 K for 300 K, and between 302 K and 303 K for 303 K. 294 K, 300 K, and 303 K of surface temperature can represent non-convective, transition, and convective regions, respectively. There is almost no difference in the temperature profile between 300 K and 303 K except in the lowest few kilometers. This confirms the fact that the upper atmospheric temperature is not affected by surface temperature if the surface temperature is larger than 298 K as in Figure 4.11. Those profiles have lower tropopause temperatures than the temperature profile of 294 K.

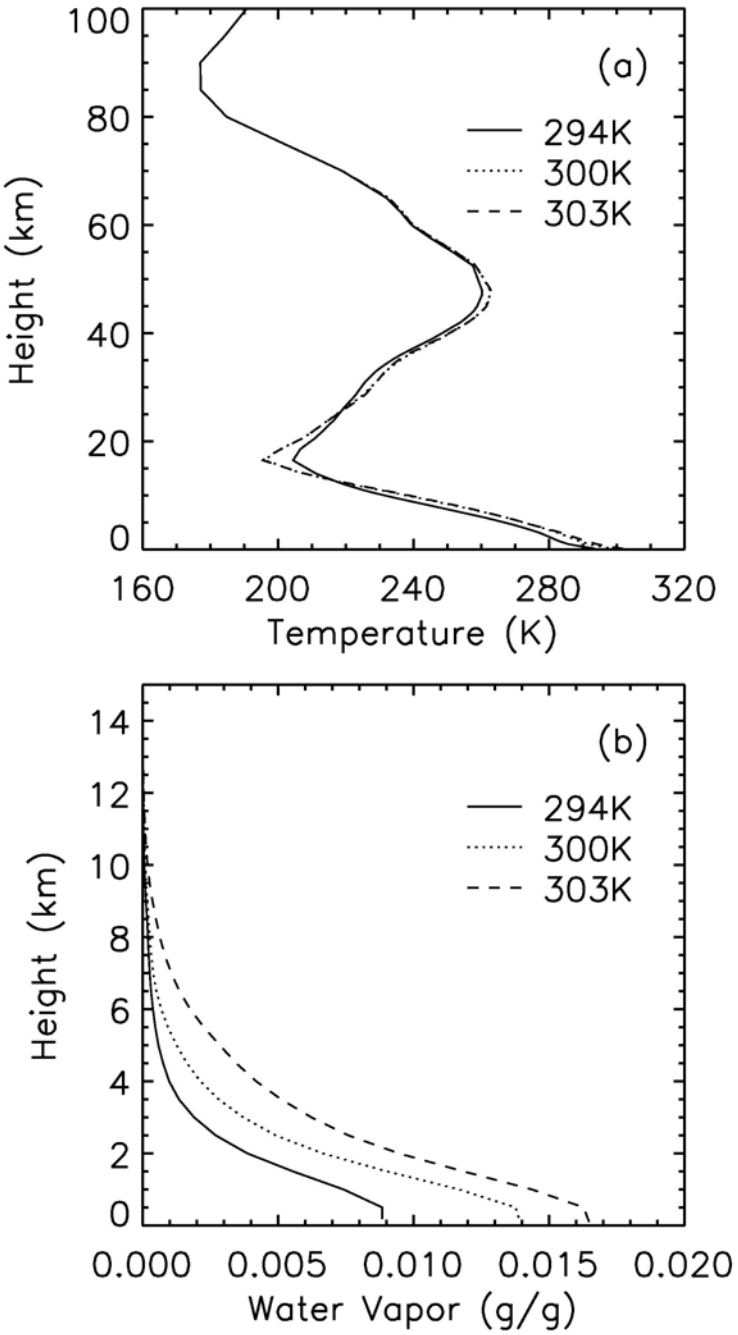

Figure 4.14 Comparison of atmospheric (a) temperature profiles and (b) water vapor profiles at the surface temperature of 294 K, 300 K, and 303 K for September 2005.

The atmospheric temperature of 294 K is lower than that of 300 K or 303 K throughout the troposphere except near the tropopause. Atmospheric temperatures of 300 K and 303 K become larger again than that of 294 K in the stratosphere. The water vapor profiles at three different temperatures show clear differences between them in Figure 4.14(b). Water vapor profile at 294K has the smallest amount of water vapor and water vapor profile at 303K is largest throughout the troposphere. The difference between 300 K and 303 K is smaller than the difference between 300 K and 294 K in the lower troposphere but larger in the upper troposphere.

To investigate the relative effect of surface temperature, lapse rate, and water vapor on OLR, each variable is exchanged between 294 K, 300 K, and 303 K and OLR is recalculated using the exchanged quantities. Table 4.1 shows the results at 294 K of surface temperature when exchanged with properties of 300 K or 303 K. The exchanged properties are surface temperature, lower tropospheric temperature, upper tropospheric temperature, total atmospheric temperature, both surface and total tropospheric temperature, lower tropospheric water vapor, upper tropospheric water vapor, and total atmospheric water vapor. The troposphere is divided into two regions: the lower troposphere from the surface to 500 hPa and the upper troposphere from 500 hPa to 100 hPa. The OLR at 294 K, 300 K, and 303 K from its own atmospheric profile is 285.3 Wm^{-2}, 297.7 Wm^{-2}, and 289.3 Wm^{-2}, respectively. ΔOLR is the difference between OLR from the exchanged property and OLR from the original atmospheric profiles. Percentage change is calculated by

Table 4.1 The change in OLR at 294 K of surface temperature when profiles of 294 K is exchanged with those of 300 K or 303 K for September 2005. All ΔOLR is the change from the original OLR of 285.3 Wm^{-2}.

294 K 285.3 Wm^{-2}	300 K 297.7 Wm^{-2} (ΔOLR=12.4 Wm^{-2})		303 K 289.3 Wm^{-2} (ΔOLR=4.0 Wm^{-2})	
exchanged property (300 K or 303 K)	OLR	ΔOLR	OLR	ΔOLR
surf temp	293.5	8.2 (2.9 %)	297.8	12.5 (4.4 %)
lower temp	295.0	9.7 (3.4 %)	297.3	12.0 (4.2 %)
upper temp	290.1	4.8 (1.7 %)	290.5	5.2 (1.8 %)
total temp	299.5	14.2 (5.0 %)	302.3	17.0 (6.0 %)
surf and total temp	307.7	22.4 (7.8 %)	314.7	29.4 (10.3 %)
lower water vapor	277.7	-7.6 (-2.6 %)	269.8	-15.5 (-5.4 %)
upper water vapor	282.1	-3.2 (-1.1 %)	274.7	-10.6 (-3.7 %)
total water vapor	274.8	-10.5 (-3.7 %)	261.1	-24.2 (-8.5 %)

$$\left(\frac{\left(OLR_{swapped} - OLR_{original} \right)}{OLR_{original}} \times 100(\%) \right) . \quad (4.1)$$

When the properties of 294 K are exchanged by 300 K, OLR increases 22.4 Wm^{-2} by the temperature effect and decreases 10.5 Wm^{-2} by the water vapor effect. The surface temperature effect (8.2 Wm^{-2}) contributes 37 % of the temperature effect (22.4 Wm^{-2}) and the atmospheric lapse rate contributes the remaining 63 %. The lapse rate effect in the lower troposphere (9.7 Wm^{-2}) is twice as large as that in the upper troposphere (4.8 Wm^{-2}). The lower troposphere water vapor effect (-7.6 Wm^{-2}) is much larger than the upper troposphere water vapor effect (-3.2 Wm^{-2}). When the properties of 294 K are exchanged with 303 K, all OLR changes are larger in magnitude compared to the changes created by the 300 K properties. However, the ratio of contribution to each change remains relatively constant. For example, the effect of surface temperature change (12.5 Wm^{-2}) occupies 43 % of the temperature effect (29.4 Wm^{-2}). The decrease of OLR by water vapor (-24.2 Wm^{-2}) of the 303 K profile is much larger than that of 300 K (-10.5 Wm^{-2}) while the increase of OLR by temperature (29.4 Wm^{-2}) of 303 K is only 7 Wm^{-2} larger than that of 300 K (22.4 Wm^{-2}). Thus, the total OLR difference between 294 K and 303 K (4.0 Wm^{-2}) is smaller than that between 294 K and 300 K (12.4 Wm^{-2}). In summary, when the atmospheric profile of 294 K is exchanged with that of 300 K or 303 K, the effect of temperature increases OLR in response to the increase of temperature and the effect of water vapor decreases OLR in response to the increased absorption by water vapor.

In Table 4.2, the OLR changes at 300 K of surface temperature when exchanged atmospheric profiles of 294 K or 303 K are presented. The net OLR change between 300 K and 294 K is an OLR decrease of 12.4 Wm^{-2} and the change between 300 K and 303 K is an OLR decrease of 8.4 Wm^{-2}. However, the mechanism of the OLR decrease is different for each case. When atmospheric profiles of 300 K are exchanged with those of 294 K, the effect of temperature decreases OLR (-22.1 Wm^{-2}) while the effect of water vapor increases OLR (10.9 Wm^{-2}) resulting in a net decrease of OLR because the decrease by temperature effect is larger than the increase by water vapor effect. When atmospheric profiles of 300 K are exchanged with those of 303 K, the effect of temperature increases OLR (6.3 Wm^{-2}) while the effect of water vapor decreases OLR (-14.1 Wm^{-2}) leading to a net decrease of OLR because the decrease by water vapor effect is larger than the increase by temperature effect. It is noted that the effect of the lower troposphere lapse rate (-11.6 Wm^{-2}) is more than half of the temperature effect (-22.1 Wm^{-2}) when profiles of 300 K are exchanged with those of 294 K. Also, the effect of the upper troposphere water vapor (-7.0 Wm^{-2}) is almost comparable to that of the lower troposphere water vapor (-7.8 Wm^{-2}). Except for this, the effect of lower troposphere is larger than that of the upper troposphere in every case, including both the effect of temperature and water vapor.

Table 4.3 shows the result of OLR change at 303 K of surface temperature by exchanged properties of 294 K or 303 K. The net change in OLR decreases when properties of 303 K are exchanged with those of 294 K and increases when exchanged with those of 300 K. The effect of temperature decreases OLR (-27.2 Wm^{-2}) and the

Table 4.2 The change in OLR at 300 K of surface temperature when profiles of 300 K is exchanged with those of 294 K or 303 K for September 2005. All ΔOLR is the change from the original OLR of 297.7 Wm^{-2}.

300 K 297.7 Wm^{-2}	294 K 285.3 Wm^{-2} (ΔOLR=-12.4 Wm^{-2})		303 K 289.3 Wm^{-2} (ΔOLR=-8.4 Wm^{-2})	
exchanged property (294 K or 303 K)	OLR	ΔOLR	OLR	ΔOLR
surf temp	292.1	-5.6 (-1.9 %)	300.7	3.0 (1.0 %)
lower temp	286.1	-11.6 (-3.9 %)	300.5	2.8 (0.97 %)
upper temp	292.6	-5.1 (-1.7 %)	298.2	0.50 (0.17 %)
total temp	281.2	-16.5 (-5.5 %)	301.1	3.4 (1.1 %)
surf and total temp	275.6	-22.1 (-7.4 %)	304.0	6.3 (2.1 %)
lower water vapor	305.0	7.3 (2.5 %)	289.9	-7.8 (-2.6 %)
upper water vapor	300.9	3.2 (1.1 %)	290.7	-7.0 (-2.4 %)
total water vapor	308.6	10.9 (3.7 %)	283.6	-14.1 (-4.7 %)

Table 4.3 The change in OLR at 303 K of surface temperature when profiles of 303 K is exchanged with those of 294 K or 300 K for September 2005. All ΔOLR is the change from the original OLR of 289.3 Wm^{-2}.

303K 289.3 Wm^{-2}	294 K 285.3 Wm^{-2} (ΔOLR=-4.0 Wm^{-2})		300 K 297.7 Wm^{-2} (ΔOLR=8.4 Wm^{-2})	
exchanged property (294 K or 300 K)	OLR	ΔOLR	OLR	ΔOLR
surf temp	283.2	-6.1 (-2.1 %)	287.2	-2.1 (-0.71 %)
lower temp	274.5	-14.8 (-5.1 %)	286.5	-2.8 (-0.95 %)
upper temp	282.5	-6.8 (-2.4 %)	288.7	-0.60 (-0.21 %)
total temp	267.8	-21.5 (-7.4 %)	285.9	-3.4 (-1.2 %)
surf and total temp	262.1	-27.2 (-9.4 %)	283.8	-5.5 (-1.9 %)
lower water vapor	304.6	15.3 (5.3 %)	297.2	7.9 (2.7 %)
upper water vapor	298.6	9.3 (3.2 %)	295.6	6.3 (2.2 %)
total water vapor	316.0	26.7 (9.2 %)	304.2	14.9 (5.2 %)

effect of water vapor increases OLR (26.7 Wm^{-2}) when profiles of 303 K are exchanged with those of 294 K. However, the similar magnitude of the two effects results in a small decrease in net OLR change. The effect of temperature decreases OLR (-5.5 Wm^{-2}) and the effect of water vapor increases OLR (14.9 Wm^{-2}) when properties of 303 K are exchanged with those of 300 K. The net OLR change is positive due to the larger positive effect by water vapor.

Similarly, to examine the relative effect of surface temperature, lapse rate, and water vapor on the greenhouse effect, the properties of 294 K, 300 K, and 303 K are exchanged and the greenhouse effect is recalculated using the exchanged properties. Table 4.4 shows the change in the greenhouse effect at 294 K of surface temperature when properties of 294 K are exchanged with those of 300 K or 303 K. The original greenhouse effect at 294 K, 300 K, and 303 K is 129.2 Wm^{-2}, 150.6 Wm^{-2}, and 176.3 Wm^{-2}, respectively. If the surface temperature increases from 294 K to 300 K, the greenhouse effect increases by 25.5 Wm^{-2} because of the increased surface emission. The increase in the lapse rate produces the decrease in the greenhouse effect because the OLR increases by increased atmospheric temperature. The effect of the lower tropospheric lapse rate (-9.7 Wm^{-2}) is larger than that of the upper tropospheric lapse rate (-4.8 Wm^{-2}). The net effect of temperature on the greenhouse is an increase of 11.3 Wm^{-2} because the increase by the effect of surface temperature (25.5 Wm^{-2}) exceeds the decrease by the effect of lapse rate (-14.2 Wm^{-2}). The effect of increased water vapor produces the increase in the greenhouse effect because increased water vapor absorbs more longwave radiation from the surface or lower atmosphere and eventually reduces

Table 4.4 The change in greenhouse effect at 294 K of surface temperature when profiles of 294 K is exchanged with those of 300 K or 303 K for September 2005. All ΔG_a is the change from the original greenhouse effect of 129.2 Wm^{-2}.

294 K 129.2 Wm^{-2}	300 K 150.6 Wm^{-2} (ΔG_a=21.4 Wm^{-2})		303 K 176.3 Wm^{-2} (ΔG_a=47.1 Wm^{-2})	
exchanged property (300 K or 303 K)	G_a	ΔG_a	G_a	ΔG_a
surf temp	154.7	25.5 (19.7 %)	167.8	38.5 (29.8 %)
lower temp	119.5	-9.7 (-7.5 %)	117.2	-12.0 (-9.3 %)
upper temp	124.4	-4.8 (-3.7 %)	124.0	-5.2 (-4.0 %)
total temp	115.0	-14.2 (-11.0 %)	112.3	-17.0 (-13.1 %)
surf and total temp	140.5	11.3 (8.8 %)	150.8	21.6 (16.7 %)
lower water vapor	136.8	7.6 (5.8 %)	144.7	15.5 (12.0 %)
upper water vapor	132.4	3.2 (2.5 %)	139.8	10.6 (8.2 %)
total water vapor	139.7	10.5 (8.1 %)	153.4	24.2 (18.7 %)

OLR. Positive effects from both temperature and water vapor result in the net increase in the greenhouse effect when properties of 294 K are exchanged with 300 K. The results are similar with larger magnitudes when properties of 294 K are exchanged with 303 K. It is noted that the temperature effect and water vapor effect on the change in the greenhouse effect are similar in magnitude for both 300 K and 303 K.

The changes in the greenhouse effect at the surface temperature of 300 K when the atmospheric profiles of 300 K are exchanged with those of 294 K or 303 K are presented in Table 4.5. If the surface temperature is exchanged with 294 K, the greenhouse effect decreases by 21. 4 Wm^{-2} due to the decreased emission from the surface. However, the exchanged atmospheric lapse rate has a positive effect (16.4 Wm^{-2}) on the greenhouse effect because of the decreased OLR at the lower temperature. The net temperature effect on the greenhouse effect is negative (-11.7 Wm^{-2}) because the surface temperature effect (-28.1 Wm^{-2}) is much larger than the atmospheric lapse rate effect (16.4 Wm^{-2}). The effect of water vapor decreases the greenhouse effect (-10.9 Wm^{-2}) due to the decrease of water vapor, which can not decrease OLR effectively. Both the negative effects of temperature and water vapor when 300 K profiles are exchanged with 294 K lead to a net decrease in the greenhouse effect. When the profiles of 300 K are exchanged with those of 303 K, the net change in the greenhouse effect is an increase of 25.7 Wm^{-2}. The temperature has a positive effect of 11.0 Wm^{-2} and the water vapor also has a positive effect of 14.1 Wm^{-2}. Similar to the change in OLR, the effect of the upper tropspheric water vapor (7.0 Wm^{-2}) is comparable to the effect of the lower

Table 4.5 The change in greenhouse effect at 300 K of surface temperature when profiles of 300 K is exchanged with those of 294 K or 303 K for September 2005. All ΔG_a is the change from the original greenhouse effect of 150.6 Wm^{-2}.

300 K 150.6 Wm^{-2}	294 K 129.2 Wm^{-2} (ΔG_a=-21.4 Wm^{-2})		303 K 176.3 Wm^{-2} (ΔG_a=25.7 Wm^{-2})	
exchanged property (294 K or 303 K)	G_a	ΔG_a	G_a	ΔG_a
surf temp	122.5	-28.1 (-18.7 %)	164.9	14.3 (9.5 %)
lower temp	162.1	11.5 (7.7 %)	147.7	-2.9 (-1.9 %)
upper temp	155.6	5.0 (3.3 %)	150.1	-0.50 (-0.33 %)
total temp	167.0	16.4 (10.9 %)	147.2	-3.4 (-2.3 %)
surf and total temp	138.9	-11.7 (-7.7 %)	161.6	11.0 (7.3 %)
lower water vapor	143.2	-7.4 (-4.9 %)	158.3	7.7 (5.2 %)
upper water vapor	147.3	-3.3 (-2.2 %)	157.6	7.0 (4.7 %)
total water vapor	139.7	-10.9 (-7.2 %)	164.7	14.1 (9.4 %)

tropospheric water vapor (7.7 Wm^{-2}) only when the profiles of 300 K are exchanged with those of 303 K.

In Table 4.6, the changes in the greenhouse effect are presented when properties of 303 K are exchanged with those of 294 K or 300 K. There is a large decrease in the greenhouse effect (-45.0 Wm^{-2}) by the decrease of surface temperature from 303 K to 294 K. Thus, the net temperature effect is still negative (-23.9 Wm^{-2}) despite the positive effect due to the change of lapse rate (21.5 Wm^{-2}). The effect of water vapor on the greenhouse effect is also negative (-26.7 Wm^{-2}). The negative effects of both temperature and water vapor lead to the large negative effect on the greenhouse effect (-47.1 Wm^{-2}) when the profiles of 303 K are exchanged with those of 294 K. When the profiles of 303 K are exchanged with those of 300K, the tendencies of change in the greenhouse effect are similar to those when exchanged with 294 K. The effect of temperature is negative (-11.8 Wm^{-2}) and the effect of water vapor is also negative (-15.0 Wm^{-2}) resulting in a net decrease in the greenhouse effect (-25.7 Wm^{-2}).

Table 4.6 The change in greenhouse effect at 303 K of surface temperature when profiles of 303 K is exchanged with those of 294 K or 300 K for September 2005. All ΔG_a is the change from the original greenhouse effect of 176.3 Wm^{-2}.

303 K 176.3 Wm^{-2}	294 K 129.2 Wm^{-2} (ΔG_a=-47.1 Wm^{-2})		300 K 150.6 Wm^{-2} (ΔG_a=-25.7 Wm^{-2})	
exchanged property (294 K or 300 K)	G_a	ΔG_a	G_a	ΔG_a
surf temp	131.3	-45.0 (-25.5 %)	161.0	-15.3 (-8.7 %)
lower temp	191.1	14.8 (8.4 %)	179.1	2.8 (1.6 %)
upper temp	183.1	6.8 (3.9 %)	176.9	0.60 (0.34 %)
total temp	197.8	21.5 (12.2 %)	179.7	3.4 (1.9 %)
surf and total temp	152.4	-23.9 (-13.5 %)	164.5	-11.8 (-6.7 %)
lower water vapor	161.0	-15.3 (-8.7 %)	168.4	-7.9 (-4.5 %)
upper water vapor	167.0	-9.3 (-5.3 %)	170.0	-6.3 (-3.6 %)
total water vapor	149.6	-26.7 (-15.1 %)	161.3	-15.0 (-8.5 %)

CHAPTER V

CONCLUSIONS

5.1 The influence of thermodynamic phase on the retrieval of mixed-phase cloud microphysical and optical properties in the visible and near infrared region

Mixed-phase clouds are a frequent phenomenon in the atmosphere and are important for several reasons. This study investigated the accuracy of the retrieval of two properties, effective particle size and optical thickness, for a single layered cloud containing both ice and water particles using the bidirectional reflectance at two wavelengths. The mixed-phase cloud was modeled as an external mixture of ice and water particles rather than as two distinct layers, each of which has hydrometeors of a single phase. Bidirectional reflectances were computed using a discrete ordinates radiative transfer model over an ocean surface having an albedo of 0.3. Based on these simulated reflectances for both single-phase and mixed-phase clouds, the effective particle diameter and optical thickness were inferred. The sensitivity of these inferred values to the ice fraction was investigated. It was shown that the assumption of a single thermodynamic phase can induce errors in the retrieved parameters when the cloud is composed of both ice and water, since the bidirectional reflectances are influenced by the ice fraction. Specifically, the effective particle size retrieved for a mixed-phase cloud from the visible and near-infrared bands can be underestimated (or overestimated) if pure water (or ice) phase is assumed, whereas the corresponding optical thickness of the mixed-phase cloud can be overestimated (or underestimated). While results were

presented for only one solar-satellite-viewing geometry, sensitivity to ice fraction is expected to hold for viewing conditions that are unaffected by sunglint. Finally, it was noted that the identification of mixed-phase clouds as well as their discrimination from well-separated multiphase cloud layers (such as thin cirrus overlying a lower-level water cloud) remains a very challenging task for passive satellite sensors.

5.2 The distribution of tropical thin cirrus clouds and their radiative impact: analyses based on MODIS and AIRS measurements

The fraction of observations and optical depth of tropical thin cirrus clouds were retrieved to study the characteristics of temporal and spatial distributions. The optical depths of thin cirrus clouds were retrieved using MODIS 1.38 μm reflectance over oceans and clear-sky pixels determined by MODIS cloud mask. It was found that these thin cirrus clouds were more frequently observed near deep convective region in the western Pacific. Detectible thin cirrus clouds were retrieved in more than 40 % of pixels flagged as clear-sky. The regions of high fraction and large optical depth were located in the northern hemisphere during spring and summer and moved southward during autumn and winter. The radiative effects of tropical thin cirrus clouds were calculated using retrieved optical depth, atmospheric profiles from AIRS, and parameterized optical properties of ice clouds. The thin cirrus clouds produced a heating in the lower part of clouds and cooling in the upper part of clouds within cloud layer. Atmospheric heating was larger for the smaller particle with constant ice water content and increased with increasing effective size of ice particle due to larger absorption. To investigate how the

clouds change the radiation field in the atmosphere, the net flux changes at the top and bottom of atmosphere were calculated. The thin cirrus clouds showed a net positive forcing at the top of atmosphere due to a larger positive longwave forcing and a net negative forcing at the bottom of atmosphere due to a larger negative shortwave forcing.

5.3 Comparison of CERES clear-sky OLR and model-calculated OLR from AIRS atmospheric profiles over the tropics and dependence of OLR and the greenhouse effect on surface temperature and water vapor

CERES clear-sky OLR and model-calculated OLR were compared to investigate the effects of temperature and water vapor on OLR. The AIRS profiles were co-located with CERES pixels, interpolated into 100 levels, and used as input data for atmospheric profiles in a radiative transfer model. The mean difference between them was 4.2 Wm^{-2} for September 2005 with a standard deviation of 2.1 Wm^{-2}. The difference was largest in the high OLR regions where low water vapor exists and smallest over the humid regions. The OLR increased with increasing surface temperature but decreased if surface temperature was greater than 300 K. The water vapor also increased with increasing surface temperature but increased water vapor absorbs more longwave radiation emitted from the surface or lower atmosphere and radiates it back to the surface resulting in reduced OLR at the top of atmosphere.

REFERENCES

Allan, R. P., K. P. Shine, A. Slingo, and J. A. Pamment, 1998: The dependence of clear-sky outgoing longwave radiation on surface temperature and relative humidity. *Q. J. R. Meteorol. Soc.*, 124, 1-22.

Baum, B. A., D. P. Kratz, P. Yang, S. C. Ou, Y. Hu, P. F. Soulen, and S-C. Tsay, 2000: Remote sensing of cloud properties using MODIS airborne simulator imagery during SUCCESS: 1. Data and models, *J. Geophys. Res.*, 105, 11767-11780.

Baum, B. A., A. J. Heymsfield, P. Yang, and S. T. Bedka, 2005a: Bulk scattering properties for the remote sensing of ice clouds. Part I: Microphysical data and models. *J. Appl. Meteor.*, 44, 1885-1895.

Baum, B. A., P. Yang, A. J. Heymsfield, S. Platnick, M. D. King, Y.-X. Hu, and S. T. Bedka, 2005b: Bulk scattering properties for the remote sensing of ice clouds. Part II: Narrowband models. *J. Appl. Meteor.*, 44, 1896-1911.

Bergman, J. W. and H. H. Hendon, 1998: Calculating monthly radiative fluxes and heating rates from monthly cloud observations, *J. Atmos. Sci.*, 55, 2471-3491.

Berk, A., L. S. Bernstein, and D. C. Robertson, 1989: MODTRAN: A moderate solution model for LOWTRAN-7, *Report GL-TR-89-0122*, Geoph. Lab. Air Force System Command, Hanscom AFB, USA.

Choi, Y. S. and C.-H. Ho, 2006: Radiative effect of cirrus with different optical properties over the tropics in MODIS and CERES observations. *Geophys. Res. Lett.*, 33, L21811, doi:10.1029/2006GL027403.

Chou, M.-D., M. J. Suarez, X.-Z. Liang, and M. M.-H. Yan, 2001: A Thermal Infrared Radiation Parameterization for Atmospheric Studies. *NASA Tech. Memo. 104606*, vol. 19, 1-55.

Comstock, J. M., and K. Sassen, 2001: Retrieval of cirrus cloud radiative and backscattering properties using combined lidar and infrared radiometer (LIRAD) measurements. *J. Atmos. Oceanic Technol.*, 18, 1658-1673.

Comstock, J. M., T. P. Ackerman, and G. G. Mace, 2002: Ground-based lidar and radar remote sensing of tropical cirrus clouds at Nauru Island: Cloud statistics and radiative impacts. *J. Geophys. Res.*, 107, doi:10.1029/2002JD002203.

Dessler, A. E., P. Yang, 2003: The distribution of tropical thin cirrus clouds inferred from Terra MODIS data. *J. Climate*, 16, 1241-1247.

Fleishauer, R. P., V. E. Larson, and T. H. Vonder Haar, 2002: Observed microphysical structure of midlevel, mixed phase clouds, *J. Atmos. Sci.*, 59, 1779-1804.

Fu, Q., and K.-N. Liou, 1992: On the correlated k-distribution method for radiative transfer in nonhomogeneous atmosphere. *J. Atmos. Sci.*, 49, 2139-2156.

Fu., Q., and K.-N. Liou, 1993: Parameterization of the radiative properties of cirrus clouds. *J. Atmos. Sci.*, 60, 2008-2025.

Fu, Q., 1996: An accurate parameterization of the solar radiative properties of cirrus clouds for climate models, *J. Climate*, 9, 2058-2082.

Gao, B.-C and Y. J. Kaufman, 1995: Selection of 1.375μm MODIS channel for remote sensing of cirrus clouds and stratospheric aerosols from space. *J. Atmos. Sci.*, 52, 4231-4237.

Gao, B.-C., Y. J. Kaufman, W. Han, and W. J. Wiscombe, 1998: Correction of thin cirrus path radiance in the 0.4-1.0μm spectral region using the sensitive 1.375μm cirrus detecting channel. *J. Geophys. Res.*, 103, 32169-32176.

Gao, B.-C., P. Yang, W. Han, R.-R. Li, and W. J. Wiscombe, 2002: An algorithm using visible and 1.38μm channels to retrieve cirrus clouds reflectances from aircraft and satellite data. *IEEE Trans. Geosci. Remote. Sensing*, 40, 1659-1668.

Henyey, L. G. and J. L. Greenstein, 1941: Diffuse radiation in the galaxy, *ApJ*, 93, 70-83.

Ho, C-H., M-D. Chou, M. Suarez, K-M. Lau, and M. M-H. Yan, 1998: Comparison of model-calcaulated and ERBE-retrieved clear-sky outgoing longwave radiation, *J. Geophys. Res.*, 103(D10), 11529-11536.

Inamdar, A. K. and V. Ramanathan, 1994: Physics of greenhouse effect and convection in warm oceans, *J. Climate.*, 7, 715-731.

Jacobson, M. Z., 2003: Development of mixed-phase clouds from multiple aerosol size distributions and the effect of the clouds on aerosol removal, *J. Geophys. Res.*, 108(D8), 4245, 10.1029/2002JD002961.

Jensen, E. J., O. B. Toon, H. B. Selkirk, J. D. Spinhirne, and M. R. Schoeberl, 1996: On the formation and persistence of subvisible cirrus clouds near the tropical tropopause. *J. Geophys. Res.*, 101, 21361-21375.

Key, J. R., P. Yang, B. A. Baum, and S. L. Nasiri, 2002: Parameterization of shortwave ice cloud optical properties for various particle habits, *J. Geophys. Res.*, 107(D13), 4181, 10.1029/2001JD000742.

King, M. D., 1987: Determination of the scaled optical thickness of clouds from reflected solar radiation measurements, *J. Atmos. Sci.*, 44, 1734-1751.

King, M. D., W. P. Menzel, Y. J. Kaufmann, D. Tanre, B.-C. Gao, S. Platnick, S. A. Ackerman, L. A. Remer, R. Pincus, and P. A. Hubanks, 2003: Cloud and aerosol properties, precipitable water, and profiles of temperature and water vapor from MODIS. *IEEE Trans. Geosci. Remote. Sensing*, 41, 442-458.

King, M. D., S. Platnick, P. Yang, G. T. Arnold, M. A. Gray, J. C. Riedi, S. A. Ackerman, and K. N. Liou, 2004: Remote sensing of liquid water and ice cloud optical thickness and effective radius in the arctic: Application of airborne multispectral MAS data, *J. Atmos. Oceanic Technol.*, 21, 857-875.

Korolev, A. V., and G. A. Isaac, 2003: Phase transformation of mixed-phase clouds, *Q. J . R. Meteorol. Soc.*, 129, 19-38.

Korolev, A. V., G. A. Isaac, S. G. Cober, J. W. Strapp, and J. Hallett, 2003: Microphysical characterization of mixed-phase clouds, *Q. J . R. Meteorol. Soc.*, 129, 39-65.

Liou, K.-N., 2002: An introduction to atmospheric radiation, 2nd ed., Academic Press, UK.

Loeb, N. G., S. Kato, K. Loukachine, and N. Manalo-Smith, 2005: Angular distribution models for top-of atmosphere radiative flux estimation from the Clouds and the Earth's Radiant Energy System instrument on the Terra satellite. Part I: Methodology. *J. Atmos. Sci*., 22, 338-351.

Lubin, D., 2004: Thermodynamic phase of maritime Antarctic clouds from FTIR and supplementary radiometric data. *J. Geophys. Res.*, 109(D04204), 10.1029/2003JD003979.

Mace, G. G., S. Benson, and S. Kato, 2006: Cloud radiative forcing at the Atmospheric Radiation Measurement Program Climate Research Facility: 2. Vertical redistribution of radiant energy by clouds. *J. Geophy. Res.*, 111, D11S91, doi:10.1029/2005JD005922.

Mayer, B. and A. Kylling, 2005: The libRadtran software package for radiative transfer calculations-description and examples of use, *Atmos. Chem. Phys.*, 5, 1855-1877.

Massie, S., A. Gettleman, W. Randel, and D. Baumgardner, 2002: The distribution of tropical cirrus in relation to convection. *J. Geophys. Res.*, 107(D21), 10.1029/2001JD001293.

Mather, J. H., T. P. Ackerman, M. P. Jensen, and W. E. Clements, 1998: Characteristics of the atmospheric state and the surface radiation budget at the tropical western Pacific ARM site, *Geophys. Res. Lett.*, 25, 4513-4516.

McFarquar, G. M., A. J. Heymsfield, J. Spinhirne, and B. Hart, 2000: Thin and subvisible tropopause tropical cirrus: Observation and radiative impacts. *J. Atmos. Sci.*, 57, 1841-1853.

Mitchell, D. L., A. Macke, and Y. Liu, 1996: Modeling cirrus clouds. Part II: Treatment of radiative properties, *J. Atmos. Sci.*, 53, 2967-2988.

Moore, K. D., K. J. Voss, and H. R. Gordon, 1998: Spectral reflectance of Whitecaps: Instrumentation, calibration, and performance in coastal waters, *J. Atmos. Oceanic Technol.*, 15, 496-509.

Nakajima, T., and M. D. King, 1990: Determination of the optical thickness and effective particle radius of cloud from reflected solar radiation measurements, Part I: Theory, *J. Atmos. Sci.*, 47, 1878-1893.

Pfister, L., H. B. Selkirk, E. J. Jensen, M. R. Schoeberl, O. B. Toon, E. V. Browell, W B. Grant, B. Gary, M. J. Mahoney, T. V. Bui, and E. Hinsta, 2001: Aircraft observation of thin cirrus clouds near the tropical tropopause. *J. Geophys. Res.*, 106, 9765-9786.

Platnick, S., J. Y. Li, M. D. King, H. Gerber, and P. V. Hobbs, 2001: A solar reflectance method for retrieving the optical thickness and droplet size of liquid water clouds over snow and ice surfaces, *J. Geophys. Res.*, 106, 15185-15199.

Platnick, S., M. D. King, S. A. Ackerman, W. P. Menzel, B. A. Baum, J. C. Riedi, and R. A. Frey, 2003: The MODIS cloud products: Algorithms and Examples from Terra. *IEEE Trans. Geosci. Remote. Sensing*, 41, 459-473.

Platt, C. M., R. S. Young, P. J. Mensen, G. R. Patterson, S. C. Marsden, R. T. Austin, and J. H. Churnside, 1998: The optical properties of equatorial cirrus from observations in the ARM Pilot Radiation Observation Experiment, *J. Atmos. Sci.*, 55, 1977-1996.

Potter, B. and J. R. Holton, 1995: The role of monsoon convection in the dehydration of the lower tropical stratosphere, *J. Atmos. Sci.*, 52, 1034-1050.

Prabhakara, C., D. P. Kratz, J.-M, Yoo, G. Dalu, and A. Vernekar, 1993: Optically thin cirrus clouds: Radiative impact on the warm pool. *J. Quant. Spectrosc. Radiat. Transfer*, 49, 467-483.

Ramanathan, V., R. D. Cess, J. E. F. Harrison, P. Minnis, B. R. Barkstrom, E. Ahmed, and D. Hartmann, 1989: Cloud-radiative forcing and climate: Results from the Earth Radiation Budget Experiment, *Science*, 243, 57-63.

Ramanathan, V. and W. Collins, 1991: Thermodynamic regulation of ocean warming by cirrus clouds deduced from observations of the 1987 El Nino. *Nature*, 351, 27-32.

Raval, A. and A. H. Oort, 1994: Observed dependence of outgoing longwave radiation on sea surface temperature and moisture, *J. Climate*, 7, 807-821.

Rawlins, F., and J. S. Foot, 1990: Remotely sensed measurements of stratocumulus properties during FIRE using the C130 aircraft multi-channel radiometer, *J. Atmos. Sci.*, 47, 2488-2503.

Riley, J. T., 1998: Mixed-phase icing conditions: a review, *Technical Report of Federal Aviation Administration*, DOT/FAA/AR-98/76, Washington DC, http://www.tc.faa.gov/its/act141/reportpage.html.

Rossow, W. B. and T.-C. Zhang, 1995: Calculation of surface and top of atmosphere radiative fluxes from physical quantities based on ISCCP data sets: 2. Validation and first results, *J. Geophys. Res.*, 99 (D10), 20829-20845.

Sohn, B. J., 1999: Cloud-induced infrared radiative heating and its implications for large-scale tropical circulations. *J. Atmos. Sci.*, 56, 2657-2672.

Stamnes, K., S. C. Tsay, W. Wiscombe, and K. Jayaweera, 1988: A numerically stable algorithm for discrete-ordinate-method radiative transfer in multiple scattering and emitting layered media, *Appl. Opt.*, 27, 2502-2509.

Stephens, G. L. 2005: Cloud feedbacks in the climate system: A critical review, *J. Atmos. Sci.*, 18, 237-273.

Sun, Z., and K. P. Shine, 1994: Studies of the radiative properties of ice and mixed phase clouds, *Q. J. R. Meteorol. Soc.*, 120, 111-137.

Twomey, S., and T. Cocks, 1989: Remote sensing of cloud parameters from spectral reflectance measurements in the near-infrared, *Beitr Phys. Atmos.*, 62, 172-179.

Wang, P. H., P. Minnis, M. P. McCormick, G. S. Kent, and K. M. Skeens, 1996: A 6-year climatology of cloud occurrence frequency from Stratospheric Aerosol and Gas Experiment II observations (1985-1990). *J. Geophys. Res.*, 101, 29407-29429.

Webster, P. J., 1994: The role of hydrological processes in ocean-atmosphere interactions, *Rev. Geophys.*, 32 (4), 427-476.

Wong, T. and D. F. Young, 2000: Validation of the CERES/TRMM ERBE-Like monthly mean clear-sky longwave dataset and the effects of the 1998 ENSO event, *J. Climate*, 13, 4256-4267.

Wielicki, B. A., B. R. Barkstrom, E. F. Harrison, R. B. Lee III, G. L. Smith, and J. E. Coopoer, 1996: Clouds and the earth's radiant energy system (CERES): An earth observing system experiment, *Bull. Am. Meteorol. Soc.*, 77, 853-868.

Winker, D. M., and C. R. Trepte, 1998: Laminar cirrus observed near the tropical tropopause by LITE. *Geophys. Res. Lett.*, 25, 3351-3354.

Yang, P., K. N. Liou, K. Wyser, and D. Mitchell, 2000: Parameterization of the scattering and absorption properties of individual ice crystals, *J. Geophys. Res.*, 105, 4699-4718.

Yang, P., B.-C. Gao, B. A. Baum, W. Wiscombe, Y. Hu, S. L. Nasiri, A. Heymsfield, G. McFarquhar, and L. Miloshevich, 2001: Sensitivity of cirrus bidirectional reflectance in MODIS bands to vertical inhomogeneity of ice crystal habits and size distributions. *J. Geophys. Res.*, 106, 17267-17291.

Yang, P., H. L. Wei, B. A. Baum, H-L. Huang, A. J. Heymsfield, Y. X. Hu, B-C. Gao, D. D. Turner, 2003: The spectral signature of mixed-phase clouds composed of non-spherical ice crystals and spherical liquid droplets in the terrestrial window region, *J. Quant. Spectrosc. Radiat. Transfer*, 79, 1171-1188.

Zuidema, P., B. Barker, Y. Han, J. Intrieri, J. Key, P. Lawson, S. Matrosov, M. Shupe, R. Stone, and T. Uttal, 2005: An arctic springtime mixed-phase cloudy boundary layer observed during SHEBA, *J. Atmos. Sci.*, 62, 160-176.

VITA

Joonsuk Lee received a bachelor's degree in Atmospheric Sciences from Yonsei University, Seoul, Korea in February 1998. He continued to study in Yonsei University until February 2000 when he received a master's degree in Atmospheric Sciences.

Mr. Lee entered the Ph.D. program in the Department of Atmospheric Sciences at Texas A&M University in August 2003, and received a Ph.D. degree in August 2007.

Mr. Lee can be reached by email at jlee@ariel.met.tamu.edu, or by contacting Dr. Ping Yang at pyang@ariel.met.tamu.edu in the Department of Atmospheric Sciences, Texas A&M University. Mr. Lee also can be reached by mailing at the Department of Atmospheric Sciences, Texas A&M University, 3150 TAMU, College Station, TX 77843-3150.